Title
3-Helix Micelles as Nanocarriers – Understanding Hierarchical Structures, Kinetic Pathway, and Controlling Multivalency

Author
Ang, JooChuan

Publication Date
2016

Peer reviewed|Thesis/dissertation

3-Helix Micelles as Nanocarriers – Understanding Hierarchical Structures, Kinetic Pathway, and Controlling Multivalency

By

JooChuan Ang

A dissertation submitted in partial satisfaction of the

requirements for the degree of

Doctor of Philosophy

in

Engineering – Materials Science and Engineering

in the

Graduate Division

of the

University of California, Berkeley

Committee in charge:

Professor Ting Xu, Chair

Professor Philip Messersmith

Professor Niren Murthy

Fall 2016

3-Helix Micelles as Nanocarriers – Understanding Hierarchical Structures, Kinetic Pathway, and Controlling Multivalency

by

JooChuan Ang

Abstract

3-Helix Micelles as Nanocarriers – Understanding Hierarchical Structures, Kinetic Pathway, and Controlling Multivalency

By

JooChuan Ang

Doctor of Philosophy in Materials Science and Engineering

University of California, Berkeley

Professor Ting Xu, Chair

This dissertation focuses on fundamental understanding of the hierarchical nanostructure and kinetic pathway of self-assembled sub-20 nm 3-helix micelles. 3-helix micelles are formed by self-assembly of a new family of amphiphilic peptide-PEG-lipid hybrid conjugates. Structural deconvolution of this complex, hierarchically assembled multi-component system is non-trivial and delineating the structural components is crucial to reveal structural insights into the organization of building block constituents. Furthermore, decoupling the effect of each component on the self-assembly kinetic pathway is imperative to appreciate their contribution towards the overall energy landscape of the system for future design of nanocarriers. The knowledge gained from these studies provides insight to identify design parameters that will facilitate the development of nanocarriers based on 3-helix micelles.

3-helix micelles demonstrate immense potential as a nanocarrier for drug delivery to the brain due to its ability to bypass the blood-brain barrier and accumulate within glioblastoma tumors in rat models. To bridge the gap in knowledge between biological performance of 3-helix micelles and fundamental structure-function correlation, the hierarchical structure and assembly kinetic pathway are studied in detail.

Unraveling the internal structure of 3-helix micelle using contrast variation small-angle neutron scattering revealed a slightly deformed side-conjugated PEG and ~85 v/v% of 3-helix micelle is comprised of water. The entropic deformation of PEG likely contributes to the high kinetic stability of 3-helix micelles whereas the high water content has significant repercussions on the mechanical properties of 3-helix micelles as a nanocarrier and could shed light on the extravasation properties of 3-helix micelles through biological barriers.

The self-assembly pathway of peptide-PEG-lipid conjugates at the air-water interface to form trimeric coiled-coils was shown to be dependent on the applied lateral pressure. PEGylated amphiphiles based on 3-helix bundle-forming peptides form a mixture of dimers and trimers at intermediate pressure and converts to trimers completely upon high surface pressure. PEG acts to mediate the interaction between bundles and preserves the coiled-coil structural integrity upon high compression.

The energy landscape of 3-helix micelle formation was also delineated to understand the role of each component within the building block contributes toward the overall self-assembly process. The key factor in determining the kinetic stability is the formation of trimeric coiled-coil bundles in the corona of 3-helix micelles, providing greater energetic barriers for subunits to overcome to dissociate from the micelle. Hydrophobic packing of alkyl chains contributes to a lesser degree to the overall kinetic stability, but plays a key role in the internal structural reorganization during the formation of trimeric coiled-coils.

The fundamental knowledge gained from structural and kinetic aspects of 3-helix micelle self-assembly process was applied to a mixture of two coiled-coil-based amphiphiles to generate a mixed micelle nanocarrier platform that provides control over the local multivalent state of ligands on the micelle surface. Tracking the distribution of the two amphiphiles within the mixed micelle indicated that they phase separate into regions enriched in one amphiphile. The ability to control multivalent ligand presentation as well as generation of ‘patchy’ mixed micelles suggests this nanocarrier platform based on 3-helix micelles has potential for ligand-targeted drug delivery applications.

Lastly, the conjugation architecture of di-alkyl chains attached to the peptide headgroup was studied to probe how alkyl packing can influence micelle stability. The results showed that highly splayed di-alkyl chains can pack more efficiently, leading to enhanced alkyl melting transition temperatures and increased stability without significantly disrupting the peptide secondary and tertiary structure. This demonstrates that conjugation architecture of alkyl chains can be a useful design parameter to manipulate the stability of 3-helix micelles.

3-Helix Micelles as Nanocarriers – Understanding Hierarchical Structures, Kinetic Pathway, and Controlling Multivalency

Table of Contents

Acknowledgments

The work described in this dissertation was made possible by the patience and guidance of my supervisor, Professor Ting Xu. I am deeply grateful to her for giving me the opportunity to work on this fascinating project. The endless curiosity and enthusiasm Ting exudes has been very inspiring. Her mission to conduct high-quality work has left a deep impression on me. I truly appreciate the time and effort Ting has invested in preparing me to be a competent researcher.

I would like to acknowledge all past and present members of the Xu group. Special thanks to Dr. Jessica Shu, Dr. Nikhil Dube, Dr. He Dong, and Dr. Reidar Lund for their help when I first started out in the group. Dr. Dong would always have useful advice whenever I ran into trouble with synthesis and my discussions with Dr. Lund about scattering and data modeling have always been fruitful and very enjoyable.

I thank all my collaborators whose expertise in subjects beyond my knowledge have added significant value to the work. The valuable input and help of Prof. Katherine Ferrara, Prof. John Forsayeth, Prof. Sinan Keten, Dr. Jai Woong Seo, Lisa Mahakian, Elizabeth Ingham, and Dan Ma are gratefully acknowledged.

Special thanks to my friends: Jose, Isaac, Tim, Will, Shawn, Brian, Benson, and Chris for putting up with my idiosyncrasies and being a good source of conversation and entertainment.

I am genuinely blessed to have met Tiffany, my fiancée, at Berkeley. She has been a steady source of love and encouragement in my life, thank you! LiWen, I could not have asked for a better sister and friend. Finally, I owe my deepest gratitude to my parents for their unwavering love.

Chapter 1

Engineered Nanoparticles for Drug Delivery

§ 1.1 Nanoparticle therapeutics

The advent of nanotechnology is widely considered to be the greatest innovation in engineering since the Industrial Revolution. At the heart of this 'nano-Industrial revolution' are nanoparticles, particles with sizes generally less than 100 nm. The size of nanoparticles is similar to that of most biological molecules and the use of nanomaterials to interface with biological systems have led to developments in medical devices, molecular diagnostic devices, and drug delivery systems.

The use of nanocarriers for drug delivery offers the possibility to encapsulate lipophilic drugs thereby enhancing their aqueous solubility, protect therapeutic agents from premature enzymatic degradation, enhance blood pharmacokinetics, improve tissue biodistribution, and decreasing dosage and frequency of administration. Currently, there are over 20 different nanoparticle formulations approved by the FDA for clinical use, with many more nanoparticle platforms (such as polymer-drug conjugates, polymeric micelles, liposomes, dendrimers etc.) in preclinical or clinical trials[1]. Liposomes were the first nanoparticle platform to be approved as a therapeutic agent in 1995 with Doxil[2] (~100 nm liposomal doxorubicin). Encapsulation of doxorubicin within liposomes resulted in ~100-fold increase in circulation time, enhanced tumor accumulation, and reduced cardiotoxicity compared to the free drug. However, there are some undesired side-effects such as skin toxicity that was not observed with free doxorubicin. Genexol, a ~25 nm poly(ethylene glycol)-poly(lactic acid) block copolymer micelle containing paclitaxel, received approval in South Korea in 2007 and is the first polymeric micellar nanoparticle in Phase II-IV trials in the United States[3-5]. This polymeric micelle formulation of paclitaxel is free of toxic surfactant, Cremophor EL, previously used as a solvent for dissolving paclitaxel (the formulation is known as Taxol), therefore allowing for lower toxicity and higher dosing compliance for patients. Preclinical data with Genexol showed a 3-fold increase in the maximum-tolerated dose and a significantly higher anti-tumor efficacy compared to free paclitaxel[6]. A different formulation of paclitaxel, bound to albumin nanoparticles ~130 nm in size, known as Abraxane, has been approved by the FDA for breast cancer in 2005, non-small cell lung cancer in 2012, and metastatic pancreatic cancer in 2013.

Although improvements in patient safety and morbidity have led to the clinical approval of nanoparticle platforms for drug delivery, efficacy in patient responses remain modest with the nanoparticle platforms offering marginal progress over conventional formulations[7, 8]. Regardless of the enhancement in circulation lifetime of drugs and enhance accumulation at lesion sites, there are a series of biological barriers that hinder the delivery of therapeutic cargo to the diseased sites[9-12]. The major challenges include opsonization and subsequent discharge from circulation by the mononuclear phagocyte system (MPS), efficient penetration of tumor tissue, and cellular internalization. Critical parameters that govern the design of nanocarriers for efficient drug delivery to tumor tissue will be discussed in the following sections.

§ 1.2 Nanocarrier design based on tumor biology

Desirable attributes of a nanocarrier include: non-toxic, long circulation, deep tumor penetration, minimal cargo leakage in serum, eventual clearance from the body etc. It is currently thought that the ideal diameter of nanocarriers for cancer therapeutics should be in the range of 10–30 nm. The 10 nm lower bound is based on sieving coefficients for the glomerular capillary walls of flexible, deformable macromolecules[13]. Similar measurements of renal filtration pore size cutoff using urinary excretion of inorganic particles[14] and globular proteins[15] yielded a filtration-size threshold of ~6 nm. In addition to renal clearance, interactions between nanoparticles and the MPS in the liver and spleen have important roles to play in nanoparticle clearance. Clearance by the MPS is size-dependent, with particles larger than 200 nm accumulating in the liver and spleen and processed by MPS cells. Surface modifications can also significantly affect MPS clearance; as the surface charge of nanoparticles increase either positively or negatively, interaction with the MPS is enhanced thus leading to faster clearance. The 30 nm upper threshold of ideal nanocarriers is based on the penetration depth of polymeric nanoparticles into solid tumors[16]. Only micelles with diameters smaller than 30 nm have significant penetration into pancreatic tumors with poor permeability. In a separate study using quantum dots, 12 nm nanoparticles diffuse away from blood vessels into the solid tumor much further than larger 60 and 125 nm particles[17]. The unique characteristic of tumor environment that is different from normal tissues has been used to design various classes of nanocarriers that can selectively deliver to tumor sites and minimize off-target effects.

1.2.1 Enhanced permeation and retention (EPR) effect – a size-based phenomenon

Blood vessels in tumors are highly irregular in architecture compared to normal tissues. In lieu of a hierarchical branching structure from large to small vessels and eventually into evenly spaced capillary beds, the spatial distribution of tumor vessels are highly heterogeneous and chaotic[18], leading to fenestrations of several hundreds of nanometer[19, 20]. The vasculature of tumors is thus leaky to macromolecules. Coupled with a poor lymphatic drainage system, the accumulation of macromolecules in tumors leaking in from blood vessels is known as the "enhanced permeation and retention (EPR) effect"[21, 22]. The EPR effect has been well-exploited in nanocarrier technology whereby nanoparticles below the tumor fenestration threshold size, 400–600 nm, can significantly accumulate within tumor tissue while localization of the nanoparticles to normal tissue is attenuated. However, the heterogeneity of EPR between tumor xenograft types might limit its usefulness[23, 24]. Recent results from human patients administered 20–30 nm PEG-cyclodextrin nanoparticles carrying camptothecin, a DNA topoisomerase I inhibitor, showed that the nanoparticles localized in the solid tumor tissue and not in adjacent tissues[25]. Furthermore, sufficient concentrations of camptothecin was achieved in the tumor to downregulate the expression of topoisomerase I, suggesting that the EPR effect might be more robust for smaller nanocarriers in the size range of 10–30 nm.

The main mechanism of transport within tumors is diffusion. The tumor interstitial matrix consists of a dense network of fibrous proteins (collagen, laminin, etc.) and proteoglycans (hyaluronic acid, heparin sulfate, etc.)[26]. The transport of nanoparticles within

the dense tumor tissue is highly dependent on its size and flexibility. Particles with sizes larger than 30 nm are unable to effectively diffuse within solid tumors[16, 17, 27]. Although large particles extravasate from blood vessels, they are unable to effectively penetrate the interior of the tumor, and are concentrated around the periphery of the blood vessels[28-31]. Administration of an anti-fibrotic agent reduced collagen expression in tumor models and resulted in enhanced intratumoral distribution of ~100 nm nanoparticles as well as significantly improved efficacy of systemically administered Doxil[32]. A multistage delivery strategy developed recently utilizes a size-switchable nanoparticle aggregate triggered by the tumor environment with low pH[33] or protease-activated disassembly[34]. The design employs 80–100 nm nanoparticles that can preferentially extravasate into the leaky vasculature of the tumor. Following extravasation into tumor tissue, the nanoparticles are broken up into smaller nanoparticles ~10 nm that can increase their diffusion within the dense tumor interstitial matrix to achieve efficient tumor penetration and distribution.

Besides the size of nanocarriers, several vascular factors such as vascular endothelial growth factors (VEGF)[35, 36] and nitric oxide[36-38] are known to increase permeability of normal blood vessels as well as that of tumor vessels, thereby enhancing the EPR effect for nanoparticle delivery across the vasculature[39, 40]. Administration of VEGF led to enhanced transvascular delivery of nanoparticles in murine tumor models. Another strategy to artificially enhance the EPR effect is through slow infusion of angiotensin to increase systolic blood pressure[41]. Another school of thought is that due to the dysfunctional nature of vessels[42] and the high interstitial pressure in solid tumors[43], extravasation of nanoparticles from the blood stream into the tumor site is inefficient. Normalization of tumor vasculature can facilitate transport of nanoparticles into the tumor[44, 45]. However, normalization means smaller average pore sizes for extravasation of nanoparticles. This approach would require the use of smaller nanoparticles (<20 nm) for drug delivery[46].

1.2.2 Surface modification

Nanoparticles without surface modifications quickly absorb a layer of protein corona in biological milieu[47] to lower their surface energy. Biomolecules that bind strongly to the surface of nanoparticles is known to form a ‘hard’ corona whereas weakly associated biomolecules are referred to be part of the ‘soft corona[48, 49]. The identities of biomolecules adsorbed on the surface of nanomaterials varies depending on the size and surface properties of the nanoparticles[50]. In the presence of non-specifically adsorbed proteins, nanoparticles are more prone to uptake by phagocytic cells, a process known as opsonization, and cleared by the MPS. To capitalize on the EPR effect, nanoparticles with long half-lives in blood have been designed to increase their propensity for extravasation across the vasculature into the tumor site[51, 52].

Chemical conjugation of poly(ethylene glycol) (PEGylation) is a common method to prolong the circulation of drugs, therapeutic proteins, and vesicles[53, 54]. The ethylene glycol repeat units associate with water molecules, forming a hydration layer. The hydration layer hinders non-specific protein adsorption and subsequent recognition by the MPS. Although PEG has long been touted as a non-immunogenic and non-antigenic agent, studies have shown

that PEGylated agents can elicit antibody formation against PEG (anti-PEG) in animals and humans[55-57]. Repeated injection of PEGylated nanoparticles causes accelerated clearance of the nanocarriers from the circulation[58, 59]. Other potential materials with low immunogenicity such as poly(phosphoesters)[60, 61], zwitterionic polybetaines[57, 62-66], XTEN[67, 68] (a class of unstructured polypeptides), and various hydrophilic polymers[69, 70] are currently in development as alternatives to PEG as coatings for long circulating stealth nanoparticles.

1.2.3 Tumor targeting

Tumor cells express many surface receptors that distinguish them from normal cells[42]. Tumor cells proliferate rapidly with elevated metabolic rates, overexpressing cell receptors for nutrition such as transferrin receptor[71, 72] and folate receptor[73, 74]. Integrins can influence tumor growth and metastasis[75] and thus a target for ligand binding[76]. Epidermal growth factor receptor (EGFR) plays an important role in tumor growth and progression[77]. ~20–30% of invasive breast cancer upregulate EGFR and has been shown to correlate inversely with overall survival[78, 79]. Besides breast cancer, EGFR is overexpressed in a variety of solid tumors[80] and is a candidate for targeted therapies.

Active targeting does not increase accumulation of nanoparticles in tumor tissue but does increase intracellular uptake through ligand-receptor mediated interactions[81-83]. Specific ligand-receptor interactions are short range interactions on the order of ~0.5 nm. Successful receptor targeting of tumor using nanoparticles requires effective extravasation into the tumor tissue before specific ligand-receptor interactions mediate cellular internalization of the targeted nanoparticles. In preclinical studies, anti-VEGF immunoliposome displayed 6-fold increase in cellular uptake at tumor site compared to non-targeted liposomes 24 hr after intravenous administration[84]. A number of lipid- and polymer-based nanoparticles targeting transferrin receptor and EGFR are currently being evaluated in clinical trials[85, 86]. Monoclonal antibodies have also been used as targeting ligands due their high affinity and specificity for their targets. However, the bulky size and redundant constant regions of monoclonal antibodies can lead to increase in overall size and immunogenicity of the functionalized nanoparticle. The use of short peptides, aptamers, and antibody fragments[87-89] could potentially overcome this shortcoming. A potential caveat of ligand functionalization is the increase in opsonization due to the targeting moiety. Targeting specificity of transferrin was loss when nanoparticles placed in complex biological media adsorbs a biomolecule corona, leading to undesired shielding of targeting ligands[90]. In all, a delicate balance between stealth and degree of targeting ligand functionalization is required to maintain long circulation of nanoparticles for efficient extravasation into tumor tissue and subsequent targeting of ligands to specific receptors for enhanced intracellular transport.

1.2.4 Deformability

The development of nanoparticle stiffness to tune the pharmacokinetics and biodistribution of nanocarriers is a relatively new concept[91]. Nanogels of varying softness using zwitterionic monomers were produced by tuning the cross-linking density. Softer

nanogels pass through splenic filtration more easily than their more rigid counterparts, resulting in longer circulation and lower splenic accumulation[92]. Similar results were observed with hydrogel particles, where highly deformable micrometer-sized particles avoided filtration by the lungs and spleen to achieve long circulation lifetimes in excess of 30 hr[93, 94]. The flexibility and deformability of nanoparticles may also contribute to the transport of particles through small capillaries, such as those in the lung, as shown by microfluidic capillary models[95]. Moreover, semi-flexible macromolecules are more efficient at penetrating dense barriers than rigid spherical particles of comparable size[96, 97]. Altogether, studies indicate that deformable, soft nanoparticles demonstrate the ideal transport properties in blood circulation as well as within solid tumors for long half-lives and deep tumor penetration.

§ 1.3 Amphiphilic block co-polymeric micelles as nanocarriers

Polymeric micelles currently under clinical evaluation as nanocarriers[98, 99] are amphiphilic block copolymers with a hydrophilic block (usually PEG) and a hydrophobic block (such as polyesters and poly(amino acids)). Under aqueous conditions, the hydrophobic block will prefer to repel water and self-aggregate to form a water-excluded core whereas the hydrophilic block will form a shell to mediate interactions with the aqueous environment. Drugs can either be chemically conjugated to the hydrophobic block or physically encapsulated within the hydrophobic core.

Micelle thermodynamic stability is governed by the concentration at which micelles are formed, known as the critical micelle concentration (CMC). The CMC of amphiphilic polymeric micelles are on the order of 10^{-6} to 10^{-7} M which is much lower than that of low molecular weight surfactants, about 10^{-3} to 10^{-4} M. Above the CMC, micelles exist in equilibrium with a small population of unimeric chains whereas only unimeric chains are in solution below the CMC. Generally, more hydrophobic blocks and higher molecular weights lower the CMC[100]. As a result of the low CMC, polymeric micelles are much more resistant to dilution effects and can remain stable at low concentrations. However, intravenous administration of micelles experience a large dilution, making it challenging to maintain thermodynamic stability. Kinetically stable micelles can be generated for extended periods of time below the CMC, exploiting properties of the core-forming block such as the glass transition temperature and melting temperature[101]. The crystallinity of the hydrophobic core can also influence stability; micelles formed from amorphous cores (polydecalactone) exhibit much higher CMCs than those with semi-crystalline cores (polycaprolactone and polylactide)[102]. The higher CMC of amorphous cores led to faster drug release rates albeit with a higher drug loading capacity compared to semi-crystalline cores[103].

Polymeric micelles have advantages over other nanoparticle platforms such as size over liposomes and tunable kinetic stability by controlling the core properties. The use of polymeric micelles in animal studies has resulted in 10–50 times increase in accumulation of polymeric micelles compared to the free drug[104-107]. Increasing kinetic stability of micelles has been correlated with higher accumulation of micelles in tumor[108]. Micelle blood circulation and tumor accumulation generally increases with increasing size which is optimal between 100–

160 nm. However, large micelles have poor penetration of the tumor, resulting in poor drug delivery efficacy[109]. An optimal micelle size that balances circulation time and tumor accumulation but yet does not compromise tumor penetration is critical to improve polymeric micelles as an effective nanoparticle platform for drug delivery.

§ 1.4 Potential of 3-helix micelle

A new class of nanocarriers, 3-helix micelles that are 15–20 nm in diameter, based on a trimeric coiled-coil peptide-PEG-lipid hybrid conjugate amphiphile was developed recently. In rodents, 3-helix micelle exhibited long *in vivo* circulation with a half-life of ~29.5 hr along with favorable biodistribution showing low uptake in the major MPS organs such as the liver and spleen[110]. While PEGylated nanoparticles require additonal surface modifications[111] such as polysorbate 80 or ligands that target active BBB transporters, 3-helix micelle is the only PEGylated nanocarrier to be able to effectively penetration the blood-brain barrier without further surface modification for drug delivery[112]. Moreover, 3-helix micelle accumulates within rat glioblastoma xenograft tumors significantly greater than stealth liposomes[112]. In non-human primates studies, 3-helix micelle displayed extensive distribution in brain regions through cerebrospinal fluid delivery[113]. Local administration to rat stratium through convection-enhanced delivery of doxorubicin-loaded 3-helix micelle showed broader and more homogeneous distribution compared to free drug[114]. Time-dependent positron emission tomography of intraveneously administrated doxorubucin-loaded 3-helix micelle showed that it is highly mobile within tumors. Doxorubicin-loaded 3-helix micelle displayed 2-fold increase in tumor accumulation from 24 hr to 72 hr, significantly beyond its blood circulation half-life. Moreover, the 3-helix micelle formulation of doxorubicin exhibited lower skin toxicity than liposomal doxorubicin[114], demonstrating an effective and safe platform for drug delivery. Studies in canines with spontaneous tumors have shown that the EPR effect is dependent on the tumor type with most carcinomas exhibiting high uptake of liposomes while most soft tissue sarcomas do not[115], suggesting that tumor histology may have significant impact on the EPR effect. Rather surprisingly, 3-helix micelles exhibited high degree of penetration and extensive distribution for all six carcinoma and sarcoma solid tumors studied (unpublished data). The unprecedented biological performance of 3-helix micelles highlights the unique properties of 3-helix micelles due to self-assembled interactions at the molecular level, prompting us to conduct more in depth fundamental studies to bridge the gap in knowledge between the biological performance and the structure and assembly pathway of 3-helix micelles.

§ 1.5 Synopsis of subsequent chapters

Considerable challenges lie in the clinical development of nanocarriers, despite their enormous potential. Fundamental understanding of the effect of nanocarrier design on their physiochemical properties *in vivo* is imperative for the development of drug delivery vehicles with high fidelity in complex biological environments yet modular for various applications. The focus of this dissertation is to understand the hierarchically self-assembled structure and

the role of various components in the kinetic pathway of 3-helix micelle formation. Using that knowledge, we attempt to design a micellar nanocarrier platform that can dictate the local multivalency of ligands on a sub-20 nm nanoparticle. Chapter 2 discusses the utility of 3-helix micelle as a viable platform for drug delivery to the brain. 3-helix micelle can bypass the blood-brain barrier and effectively accumulation within brain tumors. Chapter 3 elucidates the internal structure of 3-helix micelles, decoupling the radial distribution of the individual components. Main results indicated the deformation of side-conjugated PEG and an exceptionally high water content in the micelle. Chapter 4 studies the assembly process of 3-helix peptide-PEG-lipid conjugates at a model 2-D air-water interface. The results from this study provides fundamental understanding of the coiled-coil headgroup assembly within 3-helix micelles and highlights the importance of lateral pressure in the formation of trimeric coiled-coils for PEGylated amphiphiles as well as the role of side-conjugated PEG in maintaining the coiled-coil structural integrity under high lateral compression. Chapter 5 studies the role that various components of 3-helix micelle play in the self-assembly kinetic pathway. The results indicate a distinct kinetic pathway governed mainly by inter- and intra-micellar molecular rearrangement. The study decouples the energy barriers for alkyl packing, coiled-coil assembly, and subunit desorption processes. Chapter 6 describes a nanocarrier platform, based on 3-helix micelle, to control the local ligand multivalency on a sub-20 nm micelle using a mixture of amphiphilic peptide-PEG-lipid conjugates with different coiled-coil oligomeric states. Results here indicate the highly orthogonal assembly of coiled-coils as a basis for controlling oligomeric states on surfaces. Highly stable mixed micelles were generated. Time-dependent studies show the formation of ‘patchy’ mixed micelles. Chapter 7 studies the influence of di-alkyl chain conjugation architecture on the stability of 3-helix micelles. Results indicate the possibility to engineer micellar nanocarriers with tunable stability by modulating alkyl chain packing within 3-helix micelles through alkyl conjugation architecture.

Chapter 2

Enhanced Accumulation of 3-Helix Micelles in Rat Glioblastoma

There is an urgent need to develop nanocarriers for the treatment of glioblastoma multiforme (GBM). Using co-registered positron emission tomography (PET) and magnetic resonance (MR) images, here we performed systematic studies to investigate how a nanocarrier's size affects the pharmacokinetics and biodistribution in rodents with a GBM xenograft. In particular, highly stable, long-circulating three-helix micelles, based on a coiled-coil protein tertiary structure, was evaluated as an alternative to a larger liposomal nanocarrier. While the circulation half-life of the 3HM was similar to 110 nm PEGylated liposomes ($t_{1/2}$ = 15.5 and 16.5 hr, respectively), the 20 nm micelles greatly enhanced accumulation within a U87MG xenograft in nu/nu rats after intravenous injection. After accounting for tumor blood volume, the extravasated nanoparticles were quantified from PET images, yielding ~ 0.77 %ID/cm^3 for the micelles and 0.45 %ID/cm^3 for the liposomes. For GBM lesions with a volume greater than 100 mm^3, 3-helix micelle accumulation was enhanced both within the detectable tumor and in the surrounding brain parenchyma. Furthermore, 3-helix micelle accumulation was shown to extend to the margins of the GBM xenograft. In summary, 3-helix micelles provide an attractive nanovehicle for carrying treatment to GBM.

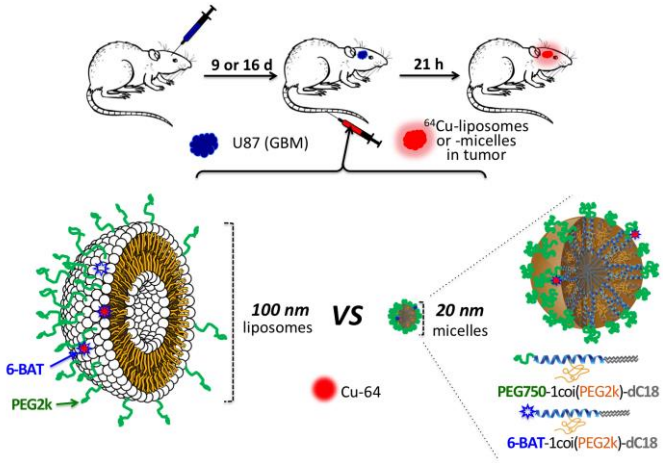

§ 2.1 Introduction

Glioblastoma multiforme (GBM) is the most common and aggressive malignant primary brain tumor, with a median patient survival of 12–15 months[1-3]. Combining radiotherapy and post-surgical chemotherapy using cisplatin[4, 5], irinotecan[6-8], thalidomide[9, 10], or bevacizumab[11, 12] has only led to a limited improvement in survival rate[13, 14]. The blood-brain barrier (BBB) typically limits the accumulation of therapeutics within the brain and such drugs can be deactivated by intra- and extra-cellular enzymes in the BBB. The BBB includes a range of passive and active transport mechanisms: 1) a paracellular pathway, regulated by tight junctions; 2) a lipophilic pathway, through the lipid membranes; 3) specific receptor-mediated transcytosis actuated by specific interactions with receptors on cerebral endothelial cells; and 4) non-specific adsorptive-mediated transcytosis, triggered by interactions between positively-charged species and negatively-charged lipid membranes on

endothelial cells[15]. The BBB is altered in the presence of diseases such as GBM and transport of nanotherapies is enhanced through junctions that are altered by the presence of disease. However, while essentially all GBM patients have significant BBB disruption, the disruption is variable across the tumor and GBM patients also have regions of tumor with limited BBB permeability[16]. Therefore, the development of strategies to enhance drug accumulation is important. Further, when drugs are delivered to the GBM tumor parenchyma, efflux transporters actively pump the drug out of the target cell[15, 17-19]. GBM therapeutics must be administered at a high dose that can lead to severe side effects and early termination of treatment, and thus, there is an urgent need to develop nanocarriers for the treatment of GBM.

It is well known that the surface chemistry of a nanocarrier determines its pharmacokinetics (PK), biodistribution, and clearance pathway[20], and PEGylation can be used to avoid recognition by the reticuloendothelial system (RES) and extend the circulation time. However, in the absence of additional surface modification, PEGylated nanocarriers typically do not cross the BBB[21, 22]. When the BBB is compromised by disease, passive delivery of nanotherapeutics is feasible. Passive delivery of long-circulating nanoparticles via the enhanced permeability retention (EPR) effect has been the major mechanism for nanoparticle uptake into tumors[23-27]. In general, smaller nanoparticles (15–50 nm) demonstrate a greater EPR effect and intratumoral distribution than larger nanoparticles (100–300 nm) and therefore show the potential to enhance accumulation within tumors[28, 29]. However, systematic studies of the effect of nanocarrier size and surface chemistry on the carrier's ability to accumulate within GBM tumor tissue have been lacking. Previous studies have shown that the vascular permeability increases in highly angiogenic glioblastoma due to the disrupted BBB providing a conduit for the delivery of nanotherapies[30-32]. However, the vascular permeability is reduced in brain tumors as compared with tumors within other organs and the size limit for nanoparticles observed to preferentially accumulate in glioblastoma (7–100 nm) is smaller than that in colorectal carcinoma, heptoma, and sarcoma (380–2000 nm)[33]. Once localized in the tumor, there is increasing evidence that nanocarriers need to be below a certain size to achieve significant tumor penetration[34-37].

Enhanced delivery to brain tumors with small nanoparticles has not yet been experimentally validated. Hobbs et al. demonstrated that particle permeability for orthotopic brain tumors was limited to particles with a diameter ranging from 7 to 100 nm[33]; however, differences within the size range were not described. Kim et al. reported that PEGylated silica nanoparticle uptake in a U87MG mouse xenograft was greater with 100–150 nm particles as compared with larger and smaller particles (40 and >300 nm)[38]. However, the tumor in this study was implanted in the mouse shoulder, which may differ in the pore cutoff size as compared with the orthotopic brain tumor.

This study compares the accumulation of two ^{64}Cu-labeled nanocarriers: a PEGylated 110 nm liposome with similar pharmacokinetics to other long-circulating liposomes[39] and recently developed sub-20 nm 3-helix micelles (3HM)[40]. This family of highly stable, long circulating 3HM is based on a coiled-coil protein tertiary structure that is routinely used to present ligand clusters on the cell surface. The headgroup of the amphiphile consists of a

peptide that self-associates to form a coiled-coil 3-helix bundle and a PEG chain (2000 Da) attached to the exterior of the 3-helix bundle at the middle position. A short PEG chain (750 Da) is also attached to one end of the peptide (C-terminus) and acts as a stealth layer on the surface of the micelle. The hydrophobic portion of the amphiphile is a double alkyl tail attached to the other end of the peptide (N-terminus). The amphiphile can be readily synthesized at high purity. Once dissolved in aqueous solution, the amphiphile self-assembles to form a 3HM that is <20 nm in size with very low polydispersity[40-44]. Systematic characterization confirmed very slow subunit exchange kinetics and excellent kinetic stability of the micelle under physiological condition[40, 42]. Micelles labelled with the FRET pair DiI and DiO demonstrated a trace level of cargo dissociation from the micelles over 24 hr in BSA[40].

Our previously developed methods to label liposomes and micelles with ^{64}Cu using the 6-BAT chelator have shown these labels to be stable in serum over 48 hr[39]. Less than 8% of the ^{64}Cu label disassociated from liposomes over 48 hr of serum incubation at 37°C and results with micelles were similar. In a mouse model, the circulation half-life for the ^{64}Cu-labeled micelles was 29.5 hr and ~15% of the injected dose/gram (%ID/g) remained in circulation after 48 hr, as compared with 7 %ID/g for PEGylated liposomes. *In vivo* studies further showed that the accumulation of 3HM in the liver and spleen is substantially reduced as compared with PEGylated liposomes[40].

Using co-registered positron emission tomography (PET) and magnetic resonance (MR) images, here we report on systematic studies to investigate how the nanocarrier's size affects the pharmacokinetics and biodistribution in rodents with GBM xenograft and evaluate the unique 3HM for the treatment of GBM. The resulting data suggest that imaging of nanoparticle distribution and tumor kinetics can be used to improve the design of nanoparticles for GBM treatment and confirmed that GBM delivery can be improved with small nanocarriers.

§ 2.2 Results and discussion

2.2.1 Physiochemical characterization of ^{64}Cu-micelles

To facilitate ^{64}Cu labeling, a custom 6-BAT chelator was incorporated into the self-assembled liposomes and micelles. Liposomes with 0.5 mol% 6-BAT lipid and micelles with 2 mol% of dC18-1CW(P2k)-6-BAT were successfully prepared in 0.1 M ammonium citrate buffer (pH 5.5) and deionized water, respectively.

The average mean diameter of the liposomes and micelles was 111.9 ± 5.7 and 19.6 ± 7.4 nm, respectively (Table 2.1). The Z-average particle size of the liposomes was about 6-fold greater than that of the micelles. The zeta-potential of the liposomes and micelles was -15.6 ± 3.5 and -13.6 ± 1.4 mV under physiological pH, where the negative charge of micelles and liposomes results from PEG on the surface. ^{64}Cu was efficiently incorporated into the 6-BAT chelator on both particles resulting in an $80 \pm 19\%$ radiolabeling yield, which is comparable to the previous reports[39, 40]. The radiochemical purities of the

liposomes and micelles measured by instant thin-layer chromatography (ITLC) were above 98% after size-exclusion chromatography. The specific activities of the liposomes and micelles were 159 ± 50.1 μCi/mg (115.6 ± 36.4 μCi/μmol_{lipid}) and 75.3 ± 40.7 μCi/mg (559.8 ± 303.1 μCi/μmol_{lipid}), respectively; sufficient to evaluate the pharmacokinetics within the glioblastoma model.

Table 2.1. Characterization of liposomes and micelles with particle size and zeta potential

	Liposomes	Micelles
Z-average size (mean ± SD, nm)[a]	111.9 ± 5.7	19.6 ± 7.4
Zeta-potential (mean ± SD, mV)[a]	-15.6 ± 3.5	-13.6 ±1.4

a. Average mean and standard deviation is calculated from two measurements of particles used for two *in vivo* experiments under physiological pH (7.3-7.5).

3HM has been thoroughly characterized using TEM and DLS as reported previously[40]. To extract the PEG shell thickness on the outer layer of 3HM, solution SAXS experiments were performed. Figure 2.1 shows the solution SAXS profiles of 3HM with and without PEG750 attached to the micelle surface. A core-shell form factor model was used to fit the SAXS data and the parameters of best fit are listed in Table 2.2. Based on these data, the PEG750 chains form an outer layer with a thickness of ~0.8 nm.

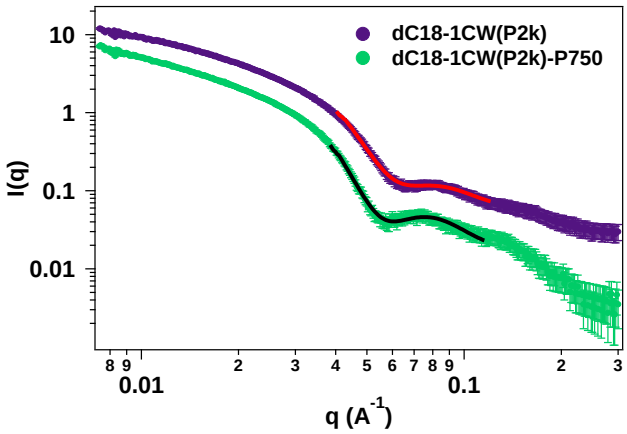

Figure 2.1. Solution SAXS results comparing micelles with and without PEG750 layer on the exterior of the micelle. The lines indicate best fit to the core-shell model. Data for dC18-1CW(P2k) has been offset vertically for clarity.

Table 2.2. Core-shell parameters from model fitting of SAXS data in Figure 2.1.

	Core radius (nm)	Shell thickness (nm)
w/o P750	3.0	5.2
with P750	3.0	6.0

2.2.2 *In vivo* positron emission tomography and magnetic resonance imaging

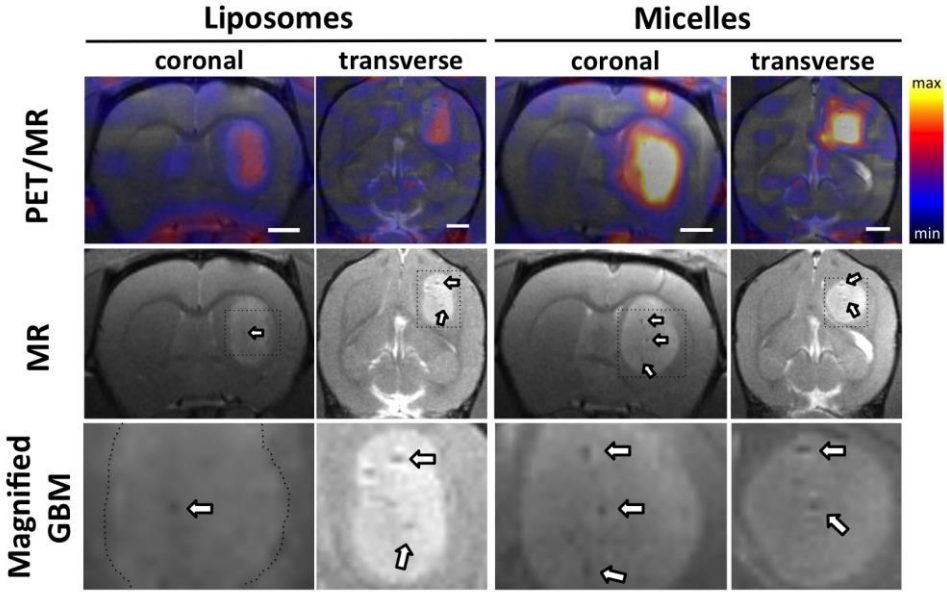

Figure 2.2. Coregistered PET/MR images (upper) and MR only images (lower) of the rat brain at 21 h post-injection of ^{64}Cu-liposomes and ^{64}Cu-micelles. Arrows indicate developed blood vessels in glioblastoma. Maximum and minimum color scale from PET images represent 1 and 0 %ID/cc, respectively and the size of the white scale bars in image is 2 mm.

T1w MRI contrast (without injection of an exogenous contrast agent) was sufficient to visualize the glioblastoma lesion in the right brain (Figure 2.2, lower row) and large blood vessels (white arrows in Figures 2.2 & 2.3) in the tumor center. MR images (Appendix A.1.1) demonstrated that intracranial injection of U87MG cells in the right brain resulted in a highly localized GBM within the right brain. The average tumor volume at 9 days after surgery (n = 6) was < 100 mm^3 (50 ± 15 mm^3) and 16 days after surgery (n = 5) was > 100 mm^3 (154 ± 36 mm^3) (Appendix A.1.2). Co-registered PET/MR images obtained 21 hr after injection of ^{64}Cu-liposomes and ^{64}Cu-micelles depict the enhanced accumulation of both particles within the tumor as compared with the adjacent striatum in the left brain (Figure 2.2). Accumulation of particles increased gradually from 0.5 to 21 h, with evident accumulation of micelles from the 3.5 hr time point (Figure 2.3a). The accumulation of 20

nm ^{64}Cu-micelles was substantially greater than that observed for 110 nm ^{64}Cu-liposomes. Radioactivity associated with both of the ^{64}Cu-labeled nanoparticles was first observed in the center of the tumor (3.5 h vs 21 hr, Figure 2.3a), reaching the periphery at later time points. ^{64}Cu-liposomes were also observed to localize around large vessels within the tumors (white arrow, upper row in Figure 2.3b). At 21 hr after injection, serial brain slices of the PET/MR images from posterior to anterior (Figure 2.3b) also demonstrate that the liposome and micelle concentration remained greater in the tumor center than in the periphery.

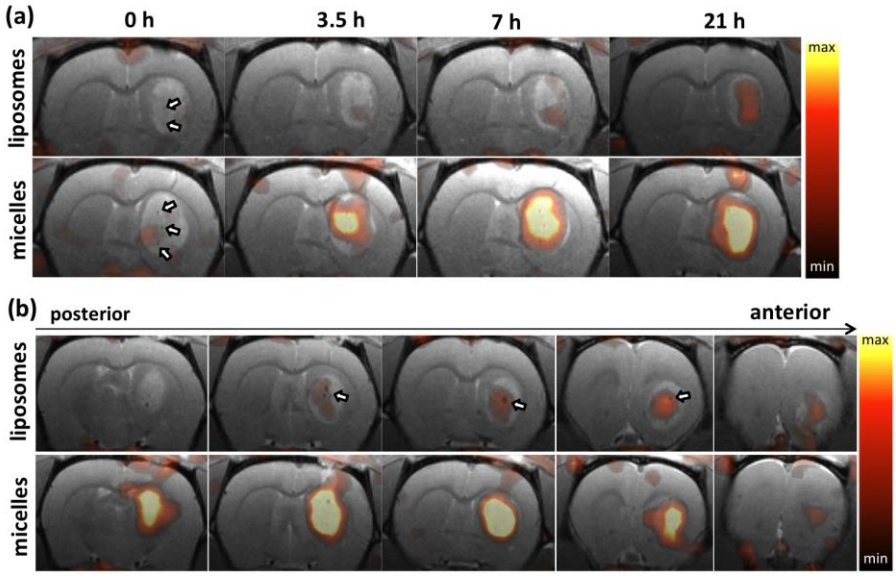

Figure 2.3. Coregistered PET/MR images of rat brain post injection of ^{64}Cu-liposomes (upper row) and ^{64}Cu-micelles (lower row). (a) From left to right, PET/MR images are acquired at 0, 3.5, 7.5 and 21 hr after injection. (b) PET/MR images acquired at 21 hr after injection, from left (posterior) to right (anterior). Each image represents a 1 mm thick slice image of the glioblastoma lesion. Arrows indicate blood vessels. Maximum and minimum values of the color scale are 1.0 and 0.3 %ID/cc, respectively.

2.2.3 Pharmacokinetics and biodistribution of 3-helix micelles

The pharmacokinetics of liposomes and micelles in blood were measured from the ROI analysis of radioactivity in the cardiac chambers. The clearance of ^{64}Cu-liposomes and ^{64}Cu-micelles in the blood pool was fit by a one-phase decay curve. The half-clearance time of liposomes and micelles was 16.5 and 15.5 hr, respectively (Figure 2.4a). Radioactivity quantified for ^{64}Cu-liposomes (2.36 ± 0.47 %ID/g, n = 6) and ^{64}Cu-micelles (2.29 ± 0.50 %ID/g, n = 5) from blood collected at 22 hr after injection (Figure 2.4b) was similar to the image-derived values (liposomes: 2.64 ± 0.16 %ID/cc, micelles: 2.74 ± 0.35 %ID/cc). The slightly lower values calculated for the image-derived estimates are expected due to partial volume effects.

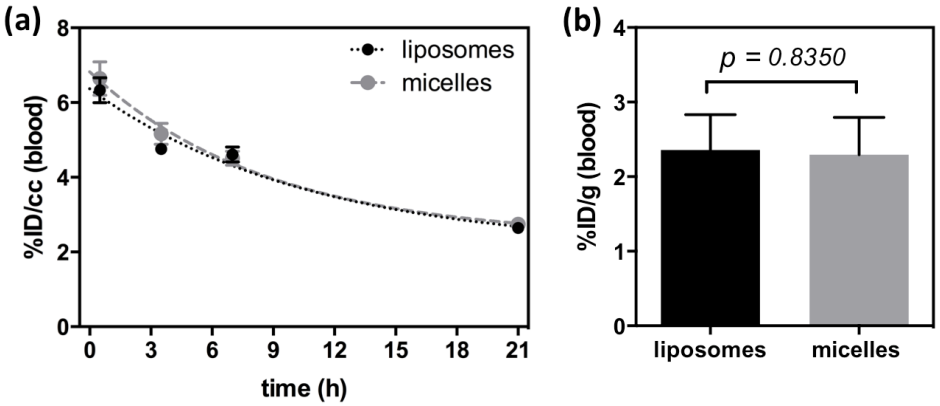

Figure 2.4. Blood clearance of ^{64}Cu-liposomes (black circle) and ^{64}Cu-micelles (gray circle) obtained from ROI analyses at 0, 3.5, 7 and 21 hr post-injection. Curve was fitted with a one phase decay ($Y_{liposomes}= 6.104exp^{-0.04206\times}$ (R^2 = *0.8330*) and $Y_{micelles}= 6.432exp^{-0.04461\times}$ (R^2 = *0.8167*). (b) Radioactivity (%ID/g) of liposomes (black bar) and micelles (gray bar) in blood at 22 hr post-injection.

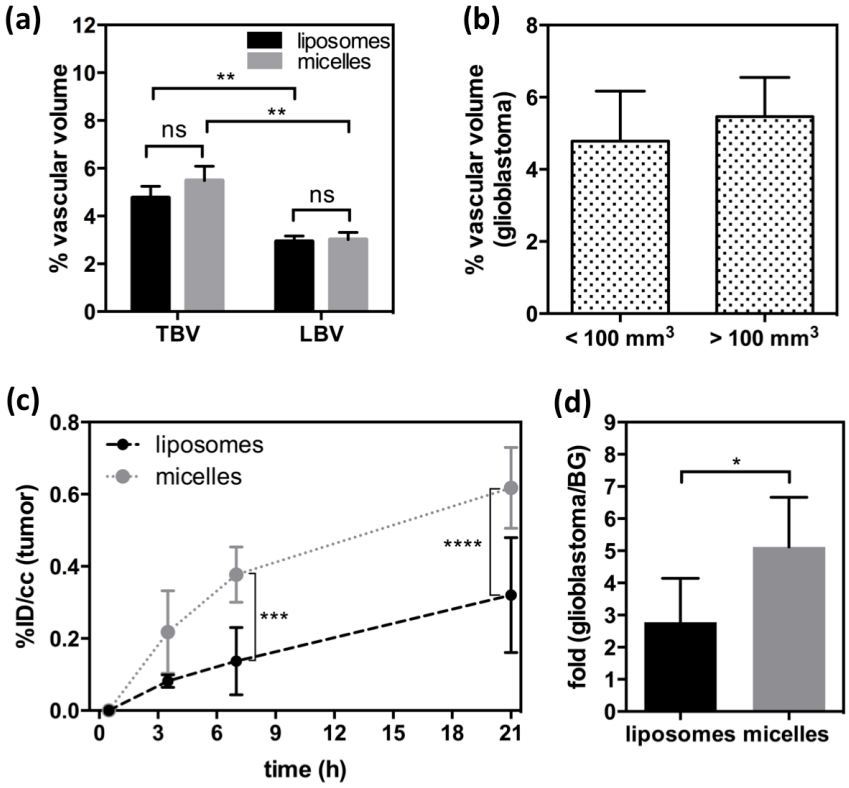

Figure 2.5. Quantification of liposomes (n = 6) and micelles (n = 5) in glioblastoma, obtained from ROI analysis (glioblastoma) of PET/MR images. (a) Tumor blood volume (TBV) and contralateral left brain blood volume (LBV) calculated by ROI analysis of glioblastoma

(right brain) and contralateral striatum (left brain) from ^{64}Cu-liposome (black bar) and ^{64}Cu-micelle (gray bar) injected rats. (b) Comparison of % vascular volume between two groups with different size of glioblastoma. (c) Blood radioactivity subtracted time activity curves of liposomes (round with dashed line) and micelles (square with dotted line). Data points represent 0, 3.5, 7, and 21 h post-injection. (d) Glioblastoma-to-background (BG) ratio of liposomes (black) and micelles (gray) in glioblastoma over contralateral left striatum, obtained from PET/MR images with blood radioactivity at 21 h (Statistical significance of (a) and (c) was determined by two-way ANOVA analysis corrected by Sidak's multiple comparison test and that of (d) was determined by an unpaired t test with Welch's correction, significance: * = P < 0.05, ** = P < 0.01, *** = P < 0.001, ****= P < 0.0001).

The biodistribution of the liposomes and micelles was then measured after perfusion of animals with Dulbecco modified eagle medium (DMEM) which was used to eliminate the remaining radioactivity contributed by the circulating nanoparticles (~2 %ID/g). The radioactivity within the glioblastoma-bearing right and left brain were gamma-counted without tumor dissection.

The increased accumulation of micelles within the right brain (containing the glioblastoma), as compared with liposomes, was validated by biodistribution. In Figure 2.6a, the accumulation of micelles and liposomes was 0.0924 ± 0.0012 %ID/g (n = 3) and 0.0372 ± 0.012 %ID/g (n = 3, $p = 0.0048$), respectively, in the right brain bearing a small tumor. This compares with (0.261± 0.015 %ID/g, n = 3) and (0.140 ± 0.029 %ID/g, n = 2, $p = 0.0086$) for micelles and liposomes, respectively, in the large xenograft. In addition, the accumulation of both liposomes ($p = 0.0143$) and micelles ($p = 0.0075$) was greater in larger xenografts relative to smaller. Surprisingly, in the contralateral left brain, accumulation of the micelles was also increased relative to that of the liposomes and the accumulation further increased in advanced xenograft peaking at 0.0304 ± 0.00041 %ID/g (Figure 2.6b).

The uptake of both nanoparticles in other organs (heart, lung, stomach, intestines, muscle, bone, liver and kidneys) was similar 22 hr after injection; however, splenic uptake of ^{64}Cu-micelles (1.39 ± 0.70 %ID/g, n = 5) was significantly lower in comparison to the ^{64}Cu-liposomes (14.8 ± 2.5 %ID/g, n = 6, $p < 0.0001$, Figure 2.6c). Intestinal radioactivity after the injection of liposomes was significantly higher, although the difference was only ~1 %ID/g.

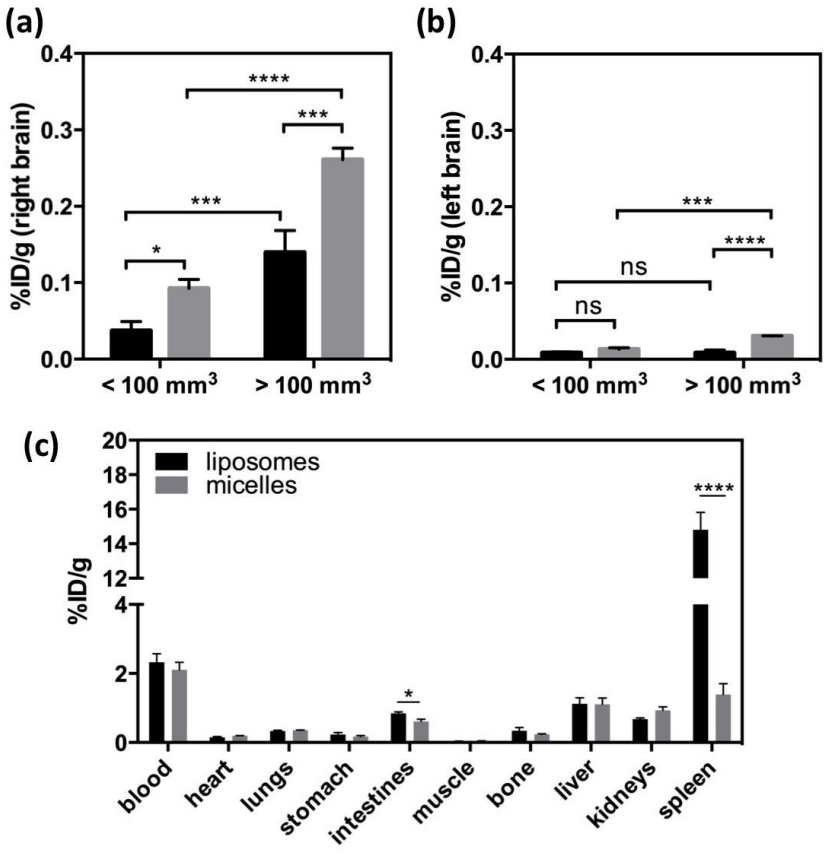

Figure 2.6. Biodistribution of ^{64}Cu-liposomes (black bar) and ^{64}Cu-micelles (gray bar) in (a) right and (b) left brain. Right brain bears glioblastoma. Percent injected dose per gram (%ID/g) was obtained after perfusion of blood at 22 hr post-injection of ^{64}Cu-liposomes (n=6) and ^{64}Cu-micelles (n=5). Right bar graphs are differentiated by tumor size. (c) Biodistribution of ^{64}Cu-liposomes (black bar, n = 6) and ^{64}Cu-micelles (gray bar, n = 5) at 22 hr post-injection. (Statistical significance of (a) and (b) was determined by two-way ANOVA analysis corrected by Sidak's multiple comparison test and that of (c) was determined by unpaired t test with Welch's correction, significance: * = $P < 0.05$, ** = $P < 0.01$, *** = $P < 0.001$, ****= $P < 0.0001$).

Applying methods for the synthesis of stable particles and PET labeling demonstrated in previous studies, here, we explore the accumulation of long-circulating liposomes and 3HM in glioblastoma using ^{64}Cu-labeled drug carriers and the combination of PET and MRI. The PEGylation on the surface of the carriers provided a similar charge and facilitated studies of the enhanced permeability and retention of nanoparticles based on differences in their diameters. Although previous studies have demonstrated that vascular permeability is reduced in brain tumors compared to tumors within other organs, enhanced delivery to brain tumors with small nanoparticles has not been clearly demonstrated. Here, we demonstrate that the uptake of 20 nm 3HM is significantly greater than 110 nm liposomes in glioblastoma 7 hr after injection (Figure 2.5c). Importantly, we observed that the micelles continued to

accumulate over the period studied here, and therefore these small particles were not clearing from the lesion, even in the absence of a targeting moiety. The micelles were well distributed throughout the tumor, potentially providing an opportunity to effectively treat disease when a drug or radiotherapy is attached.

The average fold increase for liposome and 3HM accumulation in glioblastoma compared to background (left striatum) were 2.78 and 5.12, respectively (Figure 2.5d). Although those values are lower than those measured for human glioblastoma, which has 13–19-fold higher accumulation of stealth liposomes vs. normal brain[45], the overall results demonstrate that liposomes and micelles enhanced accumulation in glioblastoma.

From the biodistribution data obtained after perfusion (Figure 2.6), the greater accumulation associated with a greater EPR effect in an advanced xenograft (>100 mm^3) was confirmed. Micelle accumulation was greater than that of liposomes regardless of the progression of the xenograft (Figure 2.6a). Although the radioactivity in the left brain was ~10-fold lower than in the right brain (Figure 2.6b), the accumulation in the normal left brain showed two significant effects associated with the adjacent disease. First, in the contralateral left brain, 3HM uptake increased with xenograft progression in the implanted right brain. The permeability of the contralateral brain could be affected by the pressure induced by the growing tumor or by cytokines and growth factors associated within the tumor[46]. Second, the 110 nm liposomal uptake in the left brain was similar (~0.008 %ID/g) regardless of the glioblastoma diameter. Thus, the extravasation of 110 nm liposomes was limited by the vascular pore size cutoff but the relatively small 20 nm 3HM crossed the BBB.

A major advantage of the PET-MRI techniques applied here is the opportunity to simultaneously view anatomy and accumulation and estimate the PK and the local blood volume. Large discrete blood vessels were detected within the tumor center with MRI. At the time of injection, the presence of these large vessels is expected to enhance the local radioactivity due to the significant blood volume within these vessels. Accumulation of nanoparticles via the EPR effect is expected to be greater in the periphery, occurring over tens of hours and peaking at the later time points. Here, with the combination of MRI and PET, radioactivity in the tumor center was observed initially with a gradual increase at the periphery.

The extended circulation of nanoparticles in the blood is crucial for the extravasation through leaky vasculature and accumulation in tumors. In our previous PK studies of liposomes and micelles in a mouse model[40, 47], the half-life of ^{64}Cu-liposomes and ^{64}Cu-micelles were 18 and 25 hr (one-phase decay), respectively. Here, we observed a shorter half-life for both particles in a rat model ($t_{1/2\ \text{liposomes and micelles}}$ = 16.5 and 15.5 hr). The observed circulation time was longer than ^{99m}Tc-labeled HYNIC-PEG liposomes previously studied in a rat model where only 52 %ID remained in the blood pool 4 hr after injection[48]. We assume that the reduced half-life observed here was due to differences in the vascular physiology between the two species. Here, the similar blood clearance of the nanoparticles in blood facilitated a direct comparison of the radioactivity in the tissues at the same time point.

When evaluating long-circulating nanoparticles, the blood volume can also be estimated by evaluating the radioactivity in the blood and tumor at the time of injection as calculated by a previously described radiometric method[49]. Previous MR studies in the rat brain reported a relationship between blood volume and vessel size where approximately 15% of C6 gliomas demonstrated an increased cerebral blood volume as compared to gray matter, and 90% demonstrated an increased average vessel size[50]. In a subsequent study, no correlation was found between blood vessel density and tumor progression in GBM[51]. Here, we observed a 62–82% increase in the % vascular volume in the tumor as compared to the contralateral LBV (Figure 2.5a) but the % vascular volume was not significantly different between small (<100 mm^3) and large tumors (>100 mm^3) (Figure 2.5b).

The biodistribution of both nanoparticles in organs such as the heart, lung, stomach, muscle, bone, liver and kidney was similar. Consistent with our previous study[40], micelle accumulation was significantly lower in the spleen than that observed with liposomes, which could ultimately reduce the treatment toxicity. Recently, 3HM were loaded with doxorubicin and prolonged drug bioavailability in circulation[42, 43], which may improve therapeutic efficacy and reduce splenic toxicity. Success in ongoing research with respect to loading or conjugating anticancer drugs to micelles could provide a promising method to treat glioblastoma[52, 53].

§ 2.3 Conclusion

Current GBM treatment includes invasive surgery, radiotherapy, and chemotherapy; however, drug delivery remains a major challenge. Here, we demonstrated that 3HM are more effective at traversing the BBB and accumulate within glioblastoma to a significantly greater extent than 110 nm liposomes. PET/MR co-registration of brain images with multiple imaging modalities may facilitate the monitoring of disease progression and planning of treatment regimens.

§ 2.4 Experimental methods

2.4.1 Preparation of ^{64}Cu-labeled liposomes and micelles

Preparation of liposomes and micelles followed our previously-reported methods[39, 40]. To facilitate post-labeling for PET, a custom lipid-PEG-chelator conjugate containing the BAT chelator is incorporated into the self-assembled liposomes and micelles. Synthesis of this conjugated was previously described [39, 40]. In brief, for liposome preparation: in a glass test tube, the dried lipid film (20 mg, HSPC:6-BAT-lipid:DSPE-PEG2k-OMe:cholesterol = 55.5:0.5:5:39, mole percent) was suspended in 0.1 M ammonium citrate buffer (pH 5.5, 0.5 mL) and the solution was incubated for 30 min at 60°C. The lipid mixture was then extruded 21 times through mini extruder with a 100 nm membrane filter under 60–65°C heating block. After cooling, the solution was kept at room temperature until ^{64}Cu labeling was complete. For micelle preparation, dC18-1CW(P2k)-P750 with 2 mol% dC18-1CW(P2k)-6-BAT (10 mg) was dissolved in double-distilled water (0.5 mL) and spontaneously self-assembled into

micelles with incubation at 70°C until the solution became clear (approximately 1 hr). Particle size and zeta-potential were measured via dynamic light scattering (DLS) with a Zetasizer Nano (Malvern Instruments Inc., Westborough, MA).

Liposomes (0.2 mL of 40 mg/mL solution) and micelles (0.4 mL of a 20 mg/mL solution) were added to $^{64}CuCl_2$ (Washington University, MA) buffered in 0.1 M ammonium citrate (pH 5.5, 0.1 mL) and incubated for 50 minutes. 0.1 M EDTA (20 mL) in double-distilled water was added in order to remove the non-specifically bound ^{64}Cu from the particles. Completion of ^{64}Cu labeling was monitored by ITLC eluted by a 0.1 M ammonium citrate solution (pH 5.5). The chemical purity of isolated ^{64}Cu-liposomes and ^{64}Cu-micelles after size-exclusion column chromatography (Sephadex-G75 superfine, 6 mL bed volume, DPBS) was determined by ITLC.

2.4.2 3-Helix micelle characterization

After dissolving the lyophilized amphiphile powder into aqueous solution, dynamic light scattering (DLS) reveals a hydrodynamic diameter of ~20 nm and a fairly uniform size distribution of micelles. We further performed solution small angle x-ray scattering studies to verify the particle size and the outer PEG layer thickness. The surface property of the micelle has significant effects on the *in vivo* behavior of nanocarrier. Although previous *in vivo* studies confirmed the effective stealth PEG layer on the 3HM surface, it is important to determine the PEG 750 conformation and the PEG brush layer density.

Small-angle x-ray scattering (SAXS) experiments were carried out at the Advanced Light Source (ALS) at the Lawrence Berkeley National Lab, Berkeley, California at the SAXS/WAXS/GISAXS beamline 7.3.3. The instrument was operated using an X-ray energy of 10 keV and a sample–detector length of 1.2 m and a 1 M Pilatus detector. Samples were contained in standard boron–quartz capillaries situated in a homemade sample holder. Using this setup, background subtraction could be made quantitatively. Samples were dissolved in phosphate buffer (25 mM, pH 7.4) at a concentration of ~5 mg/ml, annealed at 70ºC for 1 hour and allowed to equilibrate at room temperature overnight before SAXS measurements were performed.

2.4.3 Animal model

All animal experiments were conducted under a protocol approved by the University of California, Davis, Animal Use and Care Committee (Davis, CA). Eleven male athymic nude rats were purchased from Harlan Laboratories (Hayward, CA) and weighed ~250 g upon arrival. U87MG cells at 3 x 10^6 cells/10 µL were intracranially inoculated through a small burr hole in the skull into the right striatum of each rat. Imaging studies were completed at nine (n = 6) and sixteen days (n = 5) post-surgery; at this time the age ranged from 82 to 93 days and the average body weight was 294 ± 35 g.

2.4.4 Positron Emission Tomography/Magnetic Resonance (PET/MR) imaging

Radioactivity was handled under a university-approved radiation use authorization (Davis, CA). Glioblastoma-bearing rats were administered 200 µL of ^{64}Cu-liposomes (690 ±

325 μCi, 4.15 ± 0.75 mg, n = 6) and ^{64}Cu-micelles (284 ± 97 μCi, 4.22 ± 0.99 mg, n = 5) via tail vein under 1.5% isoflurane anesthesia. The critical micelle concentration (CMC) tested in this experiment is ~4 μM (~0.03 mg/mL). Thus, the micelle concentration (0.23 mg/mL) (calculated by dividing the average dose (4.22 ± 0.99 mg) of micelles by estimated blood volume (18.4 mL) [54]) was seven times higher than the CMC.

PET images were acquired with a Focus 120 scanner (Siemens Medical Solutions Inc., Malvern, PA) over 30 minutes at 0, 3.5, 7, and 21 hr after injection of nanoparticles. After PET scanning at 21 hr, MR imaging was immediately performed with a Bruker Biospec 7 Tesla (7T) small-animal scanner (Bruker BioSpin MRI, Ettlingen, Germany). A 72 mm internal diameter linear resonator was used for RF transmission and a four-channel rat brain phased array surface coil was used for signal reception. Rat brains were imaged coronally with a fast-spin echo sequence ("RARE"; axial: TE/TR = 8 ms/750 ms; FOV = 40 × 40 mm^2; MTX = 256 × 256; ST/SI = 1 mm/1 mm; ETL = 4. Coronal: TE/TR = 9ms/1200ms; FOV = 50 × 30 mm^2; MTX = 320 × 192; ST/SI = 1 mm/1 mm; ETL = 4.). Data were acquired and reconstructed with ParaVision 5.1 software (Bruker BioSpin MRI). PET/MR images were co-registered on Inveon Research Workspace 4.2 (Siemens Medical Solutions Inc., USA)

2.4.5 Biodistribution

After PET/MR imaging, animals were immediately euthanized with Euthasol (Western Medical Supply, Arcadia, CA). Blood was collected by syringe from the left ventricle and perfused from the body with Dulbecco's Modified Eagle's medium (DMEM, Invitrogen, Carlsbad, CA). Heart, lungs, stomach, intestine, muscle, bone, liver, kidneys, spleen and brain were harvested and placed in a gamma counter (Perkin-Elmer life Sciences). Values are presented as %ID/g.

2.4.6 Statistical Methods

Values are presented as means ± S.E.M. Statistical analyses were conducted using GraphPad Prism (v6). For the statistical analysis of tumor accumulation of liposomes and micelles (Figure 4a, 4c, 5a and 5b), two-way ANOVA corrected by Sidak's multiple comparisons was performed. Other values were analyzed using unpaired t-test (two-tailed) with Welch's correction. A corrected P value of * <0.05 was considered significant.

Chapter 3

Internal structure of 15 nm 3-helix micelle revealed by small-angle neutron scattering and coarse-grained MD simulation

3-helix micelles (3HM) formed by self-assembly of peptide-polymer conjugate amphiphiles have shown promise as a nanocarrier platform due to their long-circulation, deep tumor penetration, selective accumulation in tumor, and ability to cross the blood-brain barrier (BBB) for glioblastoma therapy. There is a need to understand the structural contribution to the high *in vivo* stability and performance of 3HM. Using selective deuteration, the contrast variation technique in small-angle neutron scattering, and coarse-grained molecular dynamics simulation, we determined the spatial distribution of each component within 3HM. Our results show a slightly deformed polyethylene glycol (PEG) conformation within the micelle that is radially offset from its conjugation site toward the exterior of the micelle and a highly solvated shell. Surprisingly, ~85 v/v% of 3HM is water, unusually higher than any micellar nanocarrier based on our knowledge. The result will provide important structural insights for future studies to uncover the molecular origin of 3HM's *in vivo* performance, and development of the nanocarriers.

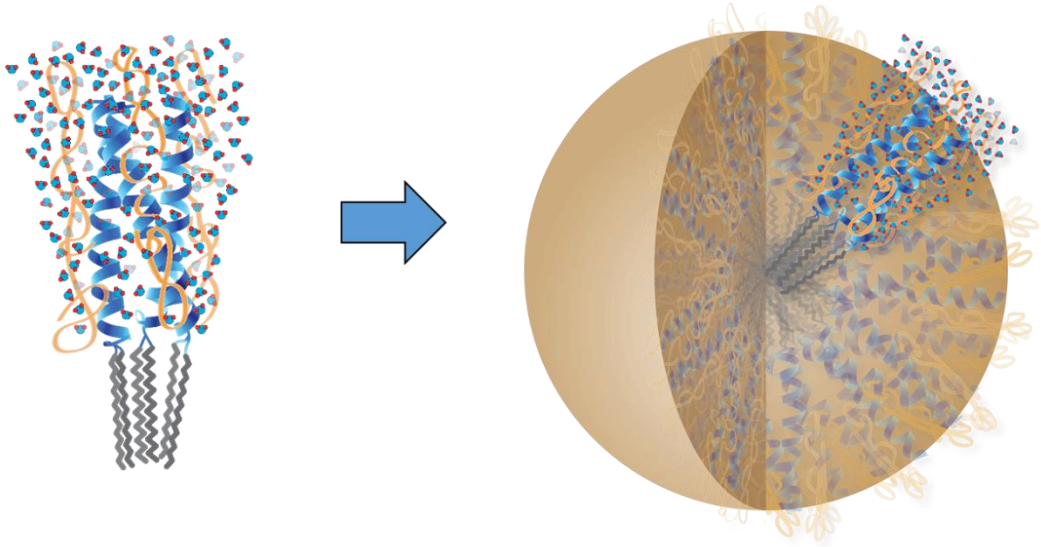

§ 3.1 Introduction

Nanocarriers of 10–30 nm are highly desirable as drug delivery and imaging probe vehicles due to their ability to cross different biological barriers and deep tissue penetration[1-4]. Stable, long circulating 3-helix micelles (3HM) based on amphiphilic peptide-polymer conjugates are attractive candidates as drug carriers. The unique sub-20 nm size regime of 3HM assures deep tumor penetration and the individual alkyl, peptide, and polymer building blocks allow for tunable micelle kinetic stability[5-7]. 3HM in mice displayed a long blood circulation half-life of 29 hours, selective accumulation in tumors, and minimal accumulation in the liver and spleen[8]. Systemic delivery of doxorubicin-loaded 3HM to tumor-bearing mice showed selective tumor accumulation over other organs[9]. Drug accumulation within the tumors also increased 2-fold from 24 to 72 hours, demonstrating that 3HM continues to accumulate within tumors significantly beyond the circulation half-life. 3HM showed higher mobility

within the tumor tissue compared to liposomes from time-dependent positron emission tomography (PET) imaging. Systemic administration of 3HM in a glioblastoma U87MG rat xenograft showed enhanced accumulation in the tumor compared to liposomes even though the two nanoparticles have a similar systemic half-life[10]. These results suggest that 3HM is more effective than liposomes in accumulating and distributing within tumor tissue as well as penetrating the BBB. However, the molecular origin is still yet to be determined. There is a great need to understand the *in vivo* performance from a structural standpoint to develop tunable, stable small nanocarriers.

3HM is a multicomponent system that is challenging to probe due to features at multiple length scales. We have conducted small-angle X-ray scattering (SAXS) studies on an absolute intensity scale to obtain the radial electron density profile of 3HM[7]. However, the low relative contrast between peptide and PEG of the amphiphile headgroup impeded extraction of PEG structural information such as conformation and distribution within 3HM. The distribution of water molecules and degree of hydration within 3HM is also unknown. Structural deconvolution of the micelle into its individual components is essential, especially for the headgroup containing peptide and PEG, to better understand the role of PEG and solvation in the structural stability of 3HM. We have previously studied the effect of alkyl chain length and PEG conjugation location along the helix backbone on the stability of 3HM[5, 7]. The complexity of 3HM is obvious and the parameter space is vast. For this contribution, we choose to focus on only one specific 3HM construct to address these questions and to shine light on the *in vivo* behavior of 3HM. Characterization of the PEG conformation and the hydration profile within 3HM will provide structural guidelines to understand the ability of 3HM to cross the BBB as well as accumulate and distribute within tumor tissue.

Understanding the internal structure of 3HM, especially the conformation of PEG and the distribution of water within 3HM, is fundamentally important to explain the structural contribution of PEG and hydration level to our previously reported *in vivo* results of 3HM. Here, we used small-angle neutron scattering (SANS) and coarse-grained MD simulation to obtain the radial distribution of PEG, conformation of PEG, radial distribution of water and overall water content within 3HM. SANS is sensitive to the large differential scattering between hydrogen and its isotope deuterium. The ability to vary the scattering length density (SLD) through hydrogen-deuterium exchange, known as contrast variation, is a key advantage of SANS over other scattering techniques including X-ray and light scattering. We used deuterated PEG and the contrast variation technique to perform multiple contrast measurements on 3HM to allow systematic decoupling of scattering contributions from the polymer and the remaining components of the amphiphile. The SLD values of the components in 3HM are shown in Table 3.1.

Table 3.1 Calculated Neutron SLDs of 3HM Components

component	SLD (10^{-6} Å^{-2})	Density (g/cm^3)
C16 alkyl	-0.08	0.85[11]
1CW peptide	1.77	1.4[12]
Deuterated PEG	6.77	1.2[13]

§ 3.2 Results and discussion

Detailed structural information of 3HM was extracted from SANS using a core-2shell model to globally fit the data on an absolute intensity scale. Figure 3.1a shows the experimental and fitted SANS profiles. The total scattering intensity is described by the sum of scattering amplitudes of the 3HM components and their interaction cross terms. The radial density profile for each component is then the Fourier transform of the corresponding scattering amplitudes (exact analytical description of the model can be found in §3.4.3). Self-consistent fits to all six solvent contrasts suggests convergence to a unique solution. As the percentage of D_2O increases from 20% to 100% D_2O, the scattering profile at 70% D_2O showed almost zero-contrast average, suggesting significant hydration of 3HM resulting in 3HM having almost the same SLD as the surrounding bulk water. In our previous studies of 3HM using SAXS, the differential electron density between peptide, polymer, and water is small. Hence, a simple core-shell model sufficed in describing the structure of 3HM using SAXS. However, a simple core-shell model with a Gaussian interface between the core and shell provided unsatisfactory fits to the SANS data (not shown), especially for high D_2O ratios where the neutron scattering contrast between the components of the shell layer is higher.

From the fits, the radial density profiles of the individual components within 3HM are extracted and shown in Figure 3.1b. The core of 3HM consists of alkyl chains (black) originating from the center of the micelle extending 25 Å radially outward. Assembly of 3HM is driven by the hydrophobic effect whereby the alkyl tails repel water and self-associate with alkyl chains from other amphiphilic subunits to form a water excluded lipid core. The size of the hydrophobic core is in good agreement with previous SAXS studies of 3HM[5, 6] and slightly larger than the maximum chain length[14, 15] of a saturated 16 hydrocarbon chain of ~22 Å possibly due to splaying of the double alkyl chains attached to the peptide[6, 16]. The shell layer of 3HM consists of 3 components – peptide (green), PEG (red), and water (blue). The peptide layer is 40 Å, in close agreement with crystallographic dimensions[17] as well as SAXS measurements[18] of the trimeric coiled-coil peptide bundle. The PEG layer has a broad ~60 Å distribution and the shell layer of 3HM is characterized by a large amount of water. At the interface between the core and the shell, water content starts to increase, reaching 75 v/v% hydration at 40 Å and in excess of 90 v/v% at 80 Å which coincides with the PEG layer. Chemical conjugation of PEG is commonly used to prolong the circulation of drugs, therapeutic proteins, and vesicles[19, 20]. The high degree of solvation around PEG chains is thought to be responsible for long blood circulation behavior of PEGylated liposomes. Tirosh et al.[21] used calorimetry to show a higher number of water molecules for PEG grafted onto the surface of liposomes in a brush conformation compared to free PEG chains in solution. The broad distribution of PEG in 3HM might allow more segments of PEG to interact with water molecules, leading to a high level of hydration. Based on the number of water molecules per PEG chain reported by Tirosh et al.[21], we calculated that the PEG chains in 3HM account for 40 – 60 % of the water in the shell layer.

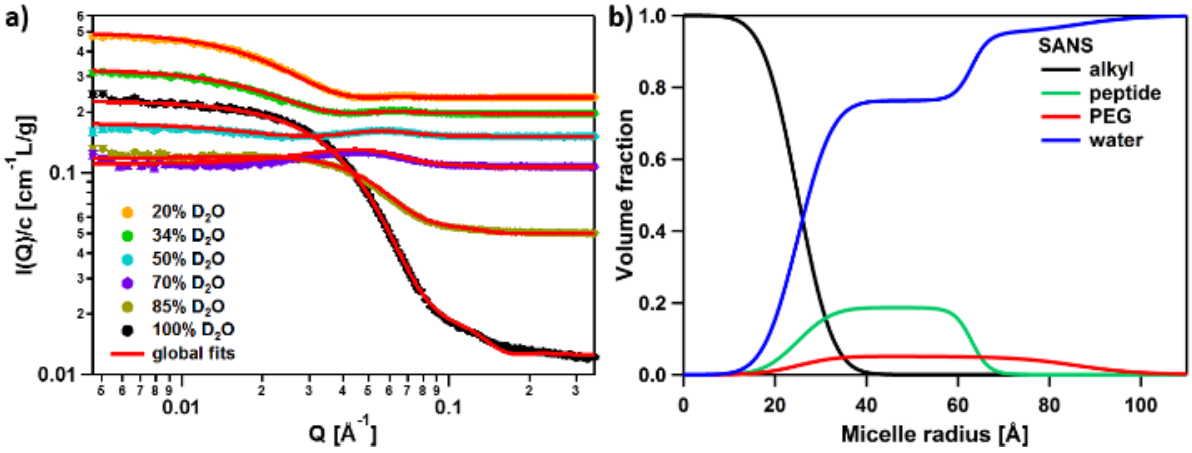

Figure 3.1. a) SANS profiles of 3HM in various amounts of D_2O/H_2O. Data sets are not offset. b) Radial distribution of 3HM components from global core-2shell modeling of SANS data. Thickness of each component is determined by the full width at half maximum (FWHM).

The overall water content of 3HM was found to be ~85% by volume, higher than block copolymer micelles of similar sizes[22, 23]. Water content of Pluronic P84[22, 24] and poly(oxybutylene-b-oxyethylene)[23] are ~40-60 v/v% depending on temperature and ~80 v/v%, respectively. G4-6 PAMAM dendrimers contain ~45% water, independent of generation[25]. PEG dendrons are stiffer and less hydrated than linear PEG analogs[26], highlighting the importance of PEG architecture in maintaining high hydration levels. Li et al.[27] used contrast variation SANS to resolve the intramicellar hydration level in block grafted copolymers and found the hydration increases with increasing PEG molecular weight. We speculate that the high level of hydration is essential to the *in vivo* performance of 3HM. If all the water molecules are excluded from 3HM, the resulting collapsed nanoparticle would have a ~9 nm diameter – significantly smaller than the hydrated 3HM. We hypothesize the high water content significantly affects the ability of 3HM to deform, extravasate into and deeply penetrate tumor tissue, as well as traverse the BBB. This is currently under investigation.

Coarse-grained molecular dynamics (CGMD) simulation was used to provide additional insight into the distribution of individual components within 3HM. Figure 3.2a shows the formation of stable, spherical micelles. To compare the weight fraction of different components (alkyl, peptide, PEG, and water) of 3HM as a function of radial distance from the micelle core, we investigated a micelle structure that has an aggregation number of 45, which is comparable to the experimentally observed aggregation number of 43. Comparison of the experimentally modeled SANS profile in Figure 3.1b with the theoretically simulated CGMD profile in Figure 3.2b reveals a similar radial distribution of the various components within 3HM. The 23 Å micelle core radius agrees well with the SANS measurement. However, the simulated 23 Å peptide layer and 37 Å PEG layer are less than that measured by SANS presumably due to the asymmetry of the radial distributions obtained by CGMD, and the difficulty of estimating interface thicknesses from SANS data. Similar trends are seen when

component thickness is taken as the range of the distribution that represents 95% of the data for each component (Appendix A.2.5). SANS and CGMD results agree that there is minimal water penetration into the core of 3HM.

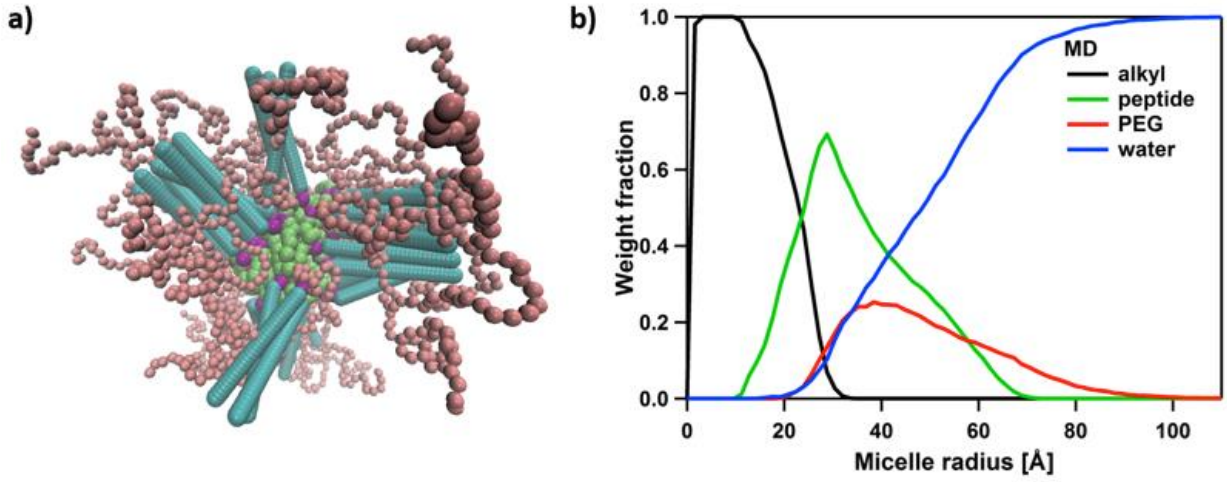

Figure 3.2. CGMD simulation. a) Snapshot of 3HM formation. The helical strands are shown in cyan while their conjugated PEG chains are pink. The alkyl chains beads are shown in green, and their connection points to the helical strands in magenta. b) Radial weight fraction of components within 3HM. The thickness of each component is determined by the FWHM, as in the case with the SANS profiles.

Considering the PEG chain distribution along the backbone of the peptide, SANS and MD results agree that the PEG chain extends beyond the peptide layer and onto the exterior surface of 3HM. Even though PEG was conjugated to the midpoint of the peptide, the polymer chain actually adopts a broader distribution along the helix backbone than we had previously expected through modeling of our SAXS results[7] using a simple core-shell model. However, using a core-2shell model to describe the SAXS profile (Appendix A.2.2) produced a PEG radial distribution profile consistent with results obtained from SANS and CGMD.

The 60 Å PEG layer measured by SANS is $2R_{ee}$ (end-to-end distance), since PEG is conjugated to the middle of the peptide sequence, giving a radial R_g (radius of gyration) of 12.2 Å using the relationship $R_{ee} \simeq \sqrt{6}\, R_g$. Based on the volume of the micelle occupied by PEG (125.3 nm^3) in the hydrophilic shell, the tangential radius of PEG is 10.7 Å. This is based on the experimentally determined aggregation number of 43 amphiphiles and assuming the PEG conformation to be an ellipsoid. The dimensions of PEG within 3HM suggests a compressed PEG chain in the tangential direction compared to free PEG in solution while the PEG chain is slightly elongated along the radial direction of 3HM. Our previous studies showed that PEG conjugated to a monomeric helical peptide in solution led to conformational changes compared to free PEG in solution due to favorable interactions between PEG and lysine residues[28, 29]. In a micellar environment, where steric confinement effects are expected

to be more pronounced, deformation of PEG was anticipated to be more severe. However, SANS showed larger elongation of the PEG chain in the radial direction of the micelle than CGMD results suggest. This was accompanied by more severe compression of PEG in the tangential direction. This might be due to limitations in experimental fitting of the SANS data, as well as the coarse-grained model where the peptide and PEG have less interaction surface area. MD results are in agreement with SANS measurements that the PEG chain is slightly extended in 3HM radially compared to free PEG in solution. Table 3.2 shows similar analysis of the PEG conformation from CGMD simulation within a single 3-helix bundle and in a micelle.

Table 3.2. Radial and tangential radius of gyration of free PEG in solution, PEG conjugated to a 3-helix bundle, and PEG in micelle.

	Radial (Å)	Tangential (Å)
Free PEG[a]	8.4±3.4	13.0±3.5
PEG in single bundle[a]	9.5±2.8	11.3±2.3
PEG in micelle[a]	9.2±0.6	13.4±0.6
PEG in micelle[b]	12.2	10.7

[a]CGMD simulation, [b]SANS modeling

Figure 3.3 shows the conformational density distribution of PEG in a single bundle compared to PEG in a micelle. The conformation of PEG between the two does not change significantly in the radial direction. In 3HM, the PEG chain is increased in the tangential direction compared to a single bundle. CGMD results indicated that the inter-PEG interaction between bundles of 3HM is responsible for modulating the PEG chain conformation. Furthermore, the slight restoration of the PEG chain conformation upon self-assembly into a micelle could have been induced by the high level of solvation within the outer shell of the micelle. Competing effects between chain expansion due to solvation and chain compression due to favorable interactions with charged amino acids on the peptide leads to an overall R_g of PEG within the micelle of 16.2 Å from SANS which is slightly smaller compared to the scaling law $R_g \propto M_w^{0.588}$ (18.8 Å) which describes the PEG2k chain in a good solvent[30]. These are potentially important findings for fundamental understanding of the role of polymer conformation in peptide-polymer interactions as well as the development of stable, long circulating hybrid micellar nanocarriers.

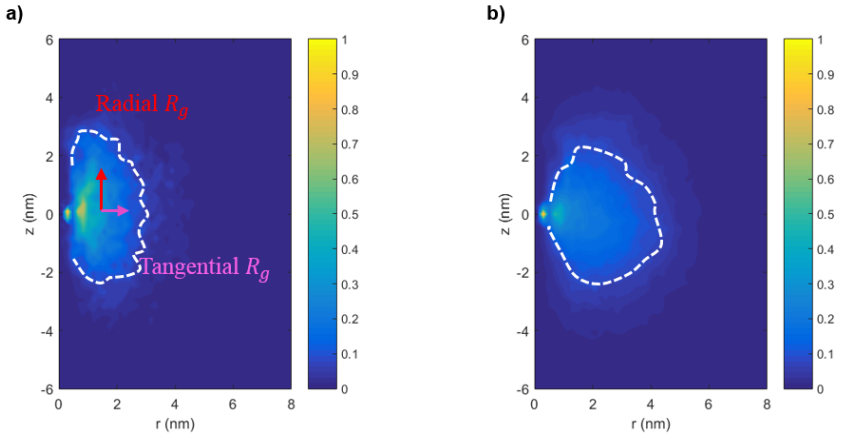

Figure 3.3. CGMD simulation showing the conformational distribution of PEG attached to (a) a single bundle and (b) in 3HM. The white dashed lines outline the PEG chain distribution with a probability larger than 0.2. The red arrow and pink arrow in (a) schematically show radial R_g and tangential R_g respectively.

§ 3.3 Conclusion

In summary, characterization of the 3HM internal structure using SANS and MD simulation revealed important insights into the distribution of side-conjugated PEG and degree of solvation along the radial direction of the micelle. A combination of SANS contrast variation and CGMD simulation was used to elucidate the distribution of PEG within 3HM. These results demonstrate that PEG has a slightly deformed conformation in the micelle compared to free PEG in solution and the PEG chain adopts a broad distribution within the hydrophilic shell of 3HM. The internal structure of 3HM from SANS modeling is consistent with the MD simulation indicating a highly solvated micelle structure, with up to ~85 v/v% of the micelle composed of water. An appreciation of the high degree of hydration within 3HM will allow us to understand the role of solvation in the *in vivo* performance of 3HM as a nanocarrier and to better design micellar nanocarriers with tunable stability for potential drug delivery applications.

§ 3.4 Experimental methods

3.4.1 Synthesis and characterization of deuterated amphiphiles

Synthesis and characterization of the materials used herein have been previously published in detail[6] and will only be described briefly. The peptide used is based on a *de novo* designed 3-helix bundle-forming peptide, referred to hereafter as 1CW (EVEALEKKVAALECKVQALEKKVEALEHGW, M = 3379 Da). PAL-PEG-PS resin (0.17 mmol/g loading, ThermoFisher Scientific) was used to conduct solid-phase synthesis of the 1CW peptide on a Prelude peptide synthesizer (Protein Technologies). The N-terminus of the

peptide was modified with a 6-(Fmoc-amino)hexanoic acid linker and the alkyl tails were conjugated to the N-terminus of the peptide through reaction of palmitic acid (C16) with deprotected Fmoc-Lys(Fmoc)-OH to generate a branched alkyl tail. Cleavage of the amphiphile was achieved using a cocktail of 90:8:2 TFA/TIS/H_2O for 3 hours. The crude peptide was precipitated in cold ether, isolated, and dried in vacuo for subsequent conjugation of deuterated PEG (dPEG). Cysteine at position 14 facilitates the site-specific coupling of maleimide-functionalized deuterated polyethylene glycol to the middle of the peptide sequence. α-Amino-ω-hydroxy poly(ethylene oxide) (>99% deuterated, M_n = 2300 g/mol, PDI = 1.08) was reacted with 8 mol equiv of N-α-maleimidoacet-oxysuccinimide ester, a short amine-to-sulfhydryl cross-linker, for 3 hours in pH 8 buffer. Excess cross-linker was removed by dialysis in DI water for 2 days (0.5–1 kDa MWCO, Spectrum Laboratories). The resulting α-maleimide-ω-hydroxy-dPEG was then reacted with cysteine at position 14 overnight in pH 7.4 buffer. Purification was achieved using HPLC, the final product dC16-1CW(dPEG) eluted at ~85% acetonitrile, using an acetonitrile/water (with 0.1% trifluoroacetic acid) gradient from 30–100% acetonitrile at a flow rate of 8 mL/min on a Beckmann Coulter HPLC. MALDI-TOF (Applied Biosystems) confirmed the presence of dPEG conjugated to the amphiphile (Appendix A.2.1).

3.4.2 Small-Angle Neutron Scattering (SANS)

SANS experiments were conducted at beamline NG3 at the National Institute of Standards and Technology (NIST, Gaithersburg, MD)[31] using cold neutrons (6 Å) with two detector distances (5m and 13m) to cover an effective range of momentum transfer, $Q = 4\pi\sin\theta/\lambda$ (θ is the scattering angle and λ is the wavelength of incident neutrons), from 0.005 – 0.35 $Å^{-1}$. Six different solvent contrasts were prepared – 20%, 34%, 50%, 70%, 85%, and 100% D_2O corresponding to neutron SLDs of 0.83, 1.80, 2.91, 4.29, 5.33, and 6.34 x 10^{-6} $Å^{-2}$, respectively. All micelle samples were prepared in a 25 mM KH_2PO_4 buffer at pH 7.4, annealed at 70^0C for 1 hour and allowed to equilibrate at room temperature overnight before conducting SANS measurements. The SANS scattering intensity profiles were reduced to absolute scale with the NIST data reduction macros in IGOR Pro available from NIST[32]. SANS data were normalized by the concentration of micelles. The concentration of micelles in various D_2O/H_2O mixtures were prepared in the aforementioned buffer at a concentration of ~4 mg/mL corresponding to ~660 μM which is >160 times greater than the critical micelle concentration of 3HM[6].

3.4.3 SANS modeling and fitting

A core-2shell model was used to describe the radial SLD profile of 3HM. The total scattering intensity can be written as:

$$I_{C2S}(Q) = \frac{\phi}{PV_{tot}}(P^2V_{lip}^2\Delta\rho_{lip}{}^2 \cdot A(Q)_{core}^2 + P^2 \cdot V_{sp}^2 A(Q)_{shell}^2$$
$$+ 2P(P - F(0)) \cdot V_{lip}V_{sp}\Delta\rho_{lip} \cdot A(Q)_{core}A(Q)_{shell} + V_{PEG}^2\Delta\rho_{PEG}{}^2 \cdot F_{chain}(Q))$$

where P is the aggregation number, $V_{tot} = V_{lip} + V_{sp}$ is the total volume of a single amphiphile,

$V_{sp} = V_{pep} + V_{PEG}$, and $\Delta\rho_j = \rho_j - \rho_0$.

The scattering amplitude of the shell layers can be described by:

$$A(Q)_{shell} = 1/V_{sp}(V_p \cdot \Delta\rho_p \cdot A(Q)_p + V_{PEG} \cdot \Delta\rho_{PEG} \cdot A(Q)_{PEG})$$

The radial density profile is:

$$n(r, \delta_j, R_j) = \frac{1}{1+\exp(\frac{r-R_j}{\delta_j})}$$

- $n(r)_{lip}$ = 1 for j=lipid
- $n(r)_{pep} = n(r, \delta_{pep}, R_{pep})$ for j=peptide
- $n(r)_{PEG} = n(r, \delta_{PEG}, R_{PEG})$ for j=PEG

where r is the distance from the center of the micelle, δ_j is the outer smearing factor for the component j, and $R_{pep} = R_c + dR$ is the cutoff thickness.

$$R_c = \left(\frac{3PV_{lip}}{4\pi}\right)^{1/3}$$

$V_j = \frac{M_j}{N_A d_j}$ where M_j is the molecular weight, N_A is Avogadro's number, and d_j is the density of the component j.

The scattering amplitude of the individual components can be calculated according to:

$$A(Q)_i = e^{-q^2\sigma_j} \int_k^\infty n(r)_j 4\pi r^2 \frac{\sin(qr)}{qr} dr$$

- For lipid: $j = 0,\ \sigma_j = \sigma_{lip} = \sigma_{core},\ k = 0$
- For peptide: $j = 1, \sigma_j = \sigma_{pep} = \sigma_{core},\ k = R_i = R_c$
- For PEG: $j = 2, \sigma_j = \sigma_{PEG},\ k = R_c$

The effective form factor[33], $F(Q)_{chain}$, can be calculated from the form factor of a single chain[34], $P(Q)_{chain}$, according to the following equation:

$$F_{chain}(Q) = P(Q)_{chain}/(1+\upsilon P(Q)_{chain})$$

$$P(Q)_{chain} = \exp(-Q^2 R_g^2/3) + d_f/R_g^{d_f}\Gamma(d_f/2)\times(\mathrm{erf}(R_g Q\times 1.06/2.44948)^3/Q)^{d_f}$$

3.4.4 Coarse-Grained Molecular Dynamics simulations (CGMD)

CGMD was performed using a variation of the dissipative particle dynamics (DPD) approach[35, 36] with the LAMMPS software[37]. DPD is a coarse-grained simulation technique that enables fast coarse-grained simulations by employing primarily repulsive interactions to describe phase separation in materials. The major benefit of this approach is the lack of kinetic

traps that may be difficult to overcome in classical MD. As such, this method has been highly useful in studying the self-assembly behavior of mesoscopic biomaterials, like lipid bilayers[38, 39], copolymers[40], and nanoparticles[41].

In previous experimental and simulation studies on PEG conjugated coiled coils, the secondary structure of helices and tertiary structure of the coiled coil were found to be fairly stable under different conjugation sites and density[28, 42-44]. Given that the coiled-coil structure is fairly stiff and short, we employed a homogeneous rigid rod model for the coiled-coils for computational efficiency[45, 46]. In order to mimic the coiled-coil tertiary structure, each rigid rod was rotated 16.71° to fit the helix end-to-end vectors. As for the alkyl tails and their linker to the N-terminus of the peptide, a similar approach modeling lipid hydrophobic beads with DPD is adopted[38, 39]. In our simulation, the hydrophobic tail can be represented as $C_2(A_4)_2$, where C and A represent the linker and alkyl tails respectively. To correctly reproduce the conformational behavior of PEG chains in the micelle, a coarse-grained model similar to MARTINI for PEG[12, 18, 47] was employed in our simulations. A previous study for PEGylated nanoparticles conducted by Li et al.[41] has validated this model by comparing the radius of gyration and end-to-end distance of PEG chains with those reported by Lee et al.[47]. The interaction parameters were adopted from Li et al.[41], which was built upon earlier work by Groot et al.[35, 36]. Here, the peptide-PEG interaction is tuned down from 26.3 to 20 (Appendix A.2.4) to achieve good agreement with the experimental data of PEG R_g in an isolated helix bundle.

An NVT ensemble was adopted for simulations, periodic boundary conditions were applied in three dimensions. Here, dimensionless Lennard-Jones unit was employed, particle mass, length scale, time scale and energy were chosen in units such that $\mathrm{m} = R_C = \tau = \mathrm{kT} = 1$. The system requires a time step $\Delta t = 0.006$, here the time scale $\tau = 24.32ps$, length scale $R_C = 0.8nm$, other DPD parameters like particle density $\rho = 3$, random noise parameter $\sigma = 3$, dissipation parameter $\gamma = 4.5$ were taken from the work of Groot et al.[35, 36]. The convergence of simulations was assured by checking the micelle aggregation number as a function of simulation time (Appendix A.2.3). The simulations were run for over 1000 ns. The reported aggregation number was obtained by taking the average aggregation number from the final 150 ns of the simulation.

Chapter 4

Understanding Peptide Oligomeric State in Langmuir Monolayers of Amphiphilic 3-Helix Bundle-forming Peptide-PEG Conjugates

Coiled-coil peptide-polymer conjugates are an emerging class of biomaterials. Fundamental understanding of the coiled-coil oligomeric state and assembly process of these hybrid building blocks is necessary to exert control over their assembly into well-defined structures. Here, we studied the effect of peptide structure and PEGylation on the self-assembly process and oligomeric state of a Langmuir monolayer of amphiphilic coiled-coil peptide-polymer conjugates using x-ray reflectivity (XR) and grazing-incidence x-ray diffraction (GIXD). Our results show that the oligomeric state of PEGylated amphiphiles based on 3-helix bundle-forming peptide is surface pressure dependent, a mixture of dimers and trimers was formed at intermediate surface pressure but transitions into trimers completely upon increasing surface pressure. Moreover, the inter-helical distance within the coiled-coil bundle of 3-helix peptide-PEG conjugate amphiphiles was not perturbed under high surface pressure. Present studies provide valuable insights into the self-assembly process of hybrid peptide-polymer conjugates and guidance to develop biomaterials with controlled multivalency of ligand presentation.

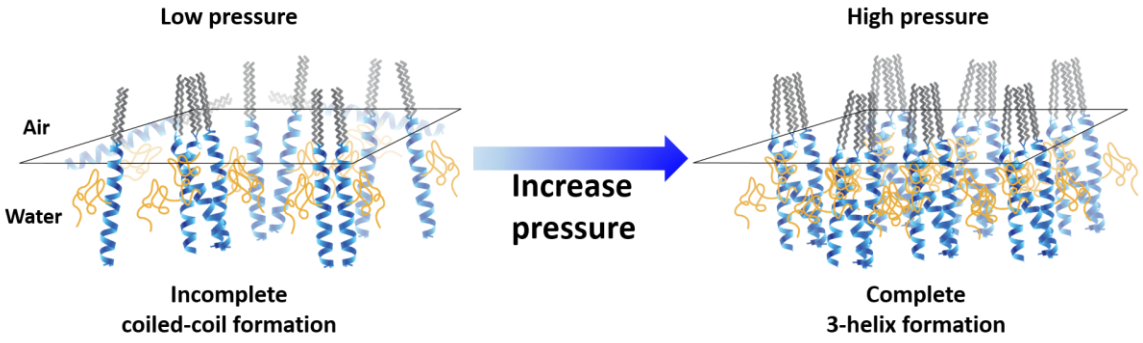

§ 4.1 Introduction

The clustering of multiple copies of ligands is a common strategy in nature to overcome weak binding of individual ligand-receptor interactions[1] and achieve high-affinity interfacial interactions[2-5]. Natural systems routinely use the coiled-coil motif to modulate ligand-receptor interactions[6, 7]. The ability to control ligand presentation on surfaces, e.g. density, multivalency, and inter-ligand distance, represent new opportunities for functional control and have great potential to meet demands for tissue engineering[8-10], regenerative medicine[11, 12], and drug delivery[13-15].

A new class of hybrid materials based on 3-helix coiled-coil peptide-polymer conjugates was reported recently[16-26]. The 3-helix peptide-polymer conjugate amphiphiles form monodisperse 3-helix micelles (3HM) with long *in vivo* circulating times[19], selective accumulation within tumors over other organs in rodents[22], and are more effective than liposomes in bypassing the blood-brain barrier and accumulating within glioblastoma U87MG xenograft tumors[25]. Parameters such as peptide structure[20], alkyl length[23], and position of side-conjugated PEG[24] allows control over the 3HM kinetic stability. The coiled-

coil structure presents a plausible platform for ligand presentation with well-defined multivalency on the surface of 3HM. To this end, it is important to understand the coiled-coil assembly process of peptide-polymer conjugate amphiphiles in solution and at surfaces. Our previous studies highlighted the importance of peptide structure[20] and PEGylation[24] on micelle kinetic stability. However, the effects of peptide structure and PEGylation on the amphiphile oligomeric state and its assembly process are unknown.

Previous studies have shown that PEGylation of 3-helix and 4-helix bundles does not adversely affect the coiled-coil formation and oligomeric state[16]. Recently, small-angle x-ray scattering (SAXS) of 3-helix and 4-helix peptide-polymer conjugates showed that the oligomeric state and polymer chain conformation can be determined through detailed modeling of the bundle form factor[18, 21]. However, it is challenging to accurately model the oligomeric state of coiled-coil amphiphiles in a micellar environment using SAXS. Coiled-coils are characterized in solution[27-31] by circular-dichroism (CD) spectroscopy, size-exclusion chromatography (SEC), and analytical ultracentrifugation (AUC) , and their atomic structures can be determined by x-ray crystallography[32]. Spectroscopically, CD studies of 3HM showed the formation of coiled-coil bundles[19, 20]. However, there is no direct structural information of the oligomeric state in bulk solution, especially whether if all the headgroups form coiled-coils rather than a fraction.

On Langmuir monolayers, XR and GIXD provide out-of-plane structure[21, 22] and in-plane spatial correlations[33, 34] of lateral molecular organization of amphiphiles, respectively. The orientation and packing of amphiphiles is usually a function of surface compression[35]. At different compressions, the out-of-plane structures would reflect various structural orientations and phase transitions of the amphiphiles at the interface[36, 37]. The in-plane structure would reflect the lateral packing and correlations between ordered domains[38-41], if any. The out-of plane structure and oligomeric state of amphiphilic 4-helix bundles[42-44] and palmitoylated 4-helix bundles[45] have previously been studied at the air-water interface using XR and GIXD. However, the coiled-coil formation process and peptide oligomeric state have yet to be studied for hybrid 3-helix peptide-polymer conjugate amphiphiles. To simplify the micelle formation problem in solution (a 3-D process), we choose to investigate the oligomeric state of coiled-coil formation of the 3-helix peptide-polymer conjugate amphiphiles at the air-water (2-D) surface.

Detailed structural studies confirmed that the PEGylated helical amphiphiles form a mixture of dimers and trimers at intermediate surface pressures. Upon increasing surface pressure, peptides in the amphiphile headgroups form trimers completely. This is in stark contrast to the amphiphile with a scrambled peptide sequence that does not form any higher oligomeric states under all surface pressures studied. The present study indicates the possibilities to engineer surfaces with different coiled-coil oligomeric states and opens up a viable platform to present multiple copies of ligands such as small molecules or short peptides on sub-20 nm nanoparticles in a precise and controlled manner. The structural complexity coupled with the specificity of peptide-based systems, opens up new possibilities to tailor the stability of micelles and target specific therapeutic destinations within the body.

§ 4.2 Results and discussion

To decouple the effects of peptide primary structure and side-conjugated PEG on the coiled-coil formation process at the air-water interface, we synthesized 3 variants of peptide-polymer conjugate amphiphiles – dC16-1CW (non-PEGylated 3-helix amphiphile), dC16-1CW(PEG2k) (PEGylated 3-helix amphiphile), and dC16-SC(PEG2k) (PEGylated scrambled amphiphile) to study Langmuir monolayers of self-assembled structures and oligomeric states using XR and GIXD. dC16-SC(PEG2k) forms a mostly random coil structure with only ~20% helicity[20] whereas the PEGylated and non-PEGylated 3-helix peptide amphiphiles form highly helical coiled-coil structures in aqueous solutions (Appendix A.3.2).

4.2.1 Langmuir isotherms

The pressure-area isotherms of Langmuir monolayers of the various amphiphiles on a buffer subphase are shown in Figure 4.1. Consider dC16-1CW (Figure 4.1a) where the transitions are more pronounced, the isotherm can be divided into roughly three regions. First, at large mean molecular areas between 600 – 800 $Å^2$/molecule, the surface pressure is essentially constant. This corresponds to a dilute amphiphile concentration at the water surface where the amphiphiles exist in a "gaseous" phase with little or no energy needed to compress the surface. The second region occurs at intermediate mean molecular areas between 150 – 600 $Å^2$/molecule where the surface pressure increases rather abruptly to ~12 mN/m at ~420 $Å^2$/molecule then gradually to ~20 mN/m upon further compression to 150 $Å^2$/molecule. This transition is indicative of physical contact between the α-helices and they behave like a liquid-expanded phase. In this region, the hydrophobic face of the helical peptide is likely to face the air and the hydrophobic alkyl chains protrude the interface. The final, third region occurs upon further compression below 150 $Å^2$/molecule where the surface pressure increases steeply with decreasing area. This condensed phase is likely to reflect an increase in amphiphile alignment perpendicular to the surface. From a previous study using solution SAXS experiments combined with theoretical modeling, the dimensions of a single 1CW α-helix was found to be reasonably well approximated by a cylinder with $R \cong 5$ Å in radius and a length of about $L \cong 45$ Å. From these dimensions we can estimate the area of an amphiphile aligned perpendicularly or horizontally to the interface as $A_{perp} = \pi \cdot R^2 \simeq 80$ $Å^2$ and $A_{hor} = 2R \cdot L \simeq 450$ $Å^2$. Comparing these values to the isotherm data for dC16-1CW, we see the first transition occurs in the range of 400 – 500 $Å^2$, while the steeper second transition occurs at smaller areas between 80 – 120 $Å^2$. These values correlate well with the estimated cross-sections of the α-helical amphiphile. This supports the proposition that at low pressure most amphiphiles lie parallel to the interface and upon increasing the pressure, the amphiphiles orient normal to the interface.

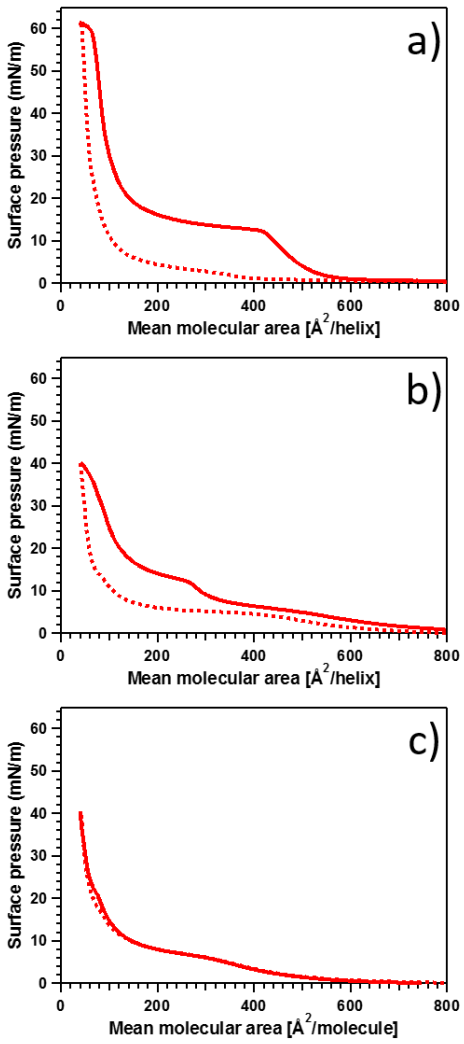

Figure 4.1. Isotherms of amphiphilic peptide-polymer conjugates at 25°C. a) dC16-1CW, b) dC16-1CW(PEG2k), and c) dC16-SC(PEG2k). The solid and dotted lines represent compression and expansion, respectively. No significant hysteresis was found in the case of the scrambled amphiphile.

The effect of PEGylation on the surface behavior of the helical amphiphile is shown in Figure 4.1b. First, dC16-1CW(PEG2k) undergoes the first transition at a smaller molecular area of ~300 Å^2/molecule compared to its non-PEGylated counterpart albeit reaching the same surface pressure. At the largest compression of 40 Å^2/molecule, dC16-1CW(PEG2k) reached a surface pressure of 40 mN/m whereas dC16-1CW obtained a surface pressure of 60 mN/m at the same compression. The first phase transition also occurs more gradually for the PEGylated dC16-1CW(PEG2k) indicating that PEG occupies a significant fraction of the interface and mediates the interaction between α-helices. This is not surprising since PEG is known to have a large exclusion volume and steric hindrance due to the high hydration layer around PEG chains[46, 47]. The second transition at low molecular area, however, is only

decreased by ~10 – 20 $Å^2$/molecule for the PEGylated amphiphile compared to the non-PEGylated amphiphile at the same surface pressure. This is indicative that upon inter-helix contact, the presence of PEG does not significantly affect the horizontal to perpendicular transition of the amphiphiles.

Altering the peptide sequence from a helical coil-coil forming peptide (1CW) into a scrambled sequence peptide (SC) resulted in minimal hysteresis of the compression/expansion cycle as shown in Figure 4.1c. In stark contrast, amphiphiles composed of the α-helical 1CW peptide (Figures 4.1a and 4.1b) displayed large hysteresis loops. The origin of the monolayer hysteresis loop under compression and expansion is likely due to the formation of coiled-coils between individual peptides at the air-water interface. Adsorption/desorption Langmuir monolayer isotherms of proteins have shown that conformational changes occur under adsorption conditions, resulting in hysteresis loops[48]. In the case of the scrambled peptide, no coiled-coil formation occurs, resulting in an absence of hysteresis in the isotherm. The phase transitions, however, occurred at similar molecular areas as that of dC16-1CW(PEG2k). At the highest compression ratios, both PEGylated 1CW and SC amphiphiles attained the same surface pressure of 40 mN/m.

4.2.2 X-ray reflectivity (XR)

XR was performed over an extended Q_z range up to about 0.6 $Å^{-1}$ covering about 9 decades in intensity. To cover the relevant regions of the isotherm, XR data were collected at the various surface pressures, 10, 20, 30, and 40 mN/m. The reflectivity profiles for all samples, normalized to the Fresnel reflection for flat, homogeneous surfaces, are given in Figure 4.2.

All three variants of peptide-polymer conjugates at all surface pressures show an excess reflectivity compared to that of a Fresnel surface. Upon compression of the samples at the interface, fringes emerge indicating that the monolayers become more structured at the interface. Well-defined fringes appear at 20 mN/m for dC16-1CW. However, the two other amphiphiles with side-conjugated PEG2k only displayed ordered structures at a higher surface pressure of 30 mN/m. This indicates that side-conjugation of PEG requires higher compression to self-assemble into ordered structures at the air-water interface.

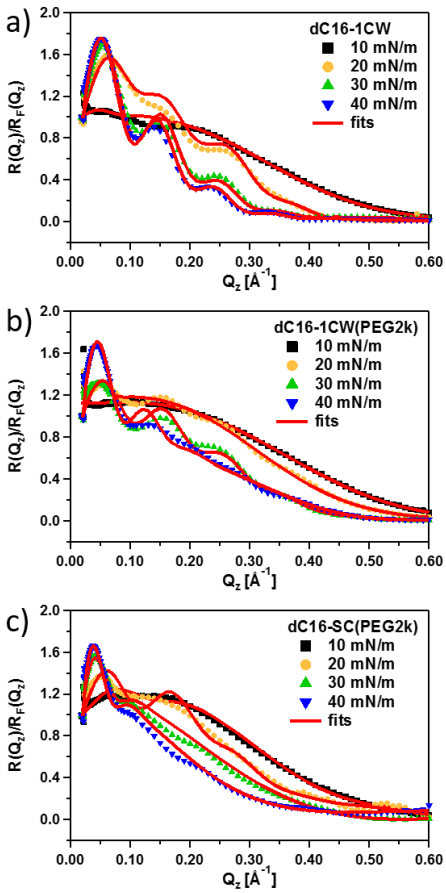

Figure 4.2. Fresnel-normalized XR data of the various amphiphilic peptide-polymer conjugates. a) dC16-1CW, b) dC16-1CW(PEG2k), and c) dC16-SC(PEG2k). The lines show the best fits based on the model described in the text.

The thickness of an interfacial layer can be determined by the period between fringes given by $d = \frac{2\pi}{\Delta Q_z}$. Qualitatively, the decrease in fringe periodicity corresponds to an increase in the film thickness. The rather pronounced decrease in fringe periodicity at low Q_z and the increase in amplitude of the fringes correspond to a significant increase in the thickness of the monolayer in real space and reflects an accumulation of amphiphiles at the surface. To extract the out-of-plane structure of the amphiphiles at the air-water interface, XR data was fitted using a box slab (optical matrix) model where the interface is modeled as discrete layers. In addition, Gaussian smearing was used to account for interfacial roughness between layers. The electron density profiles along the air-water interface obtained from the fits are shown in Figure 4.3.

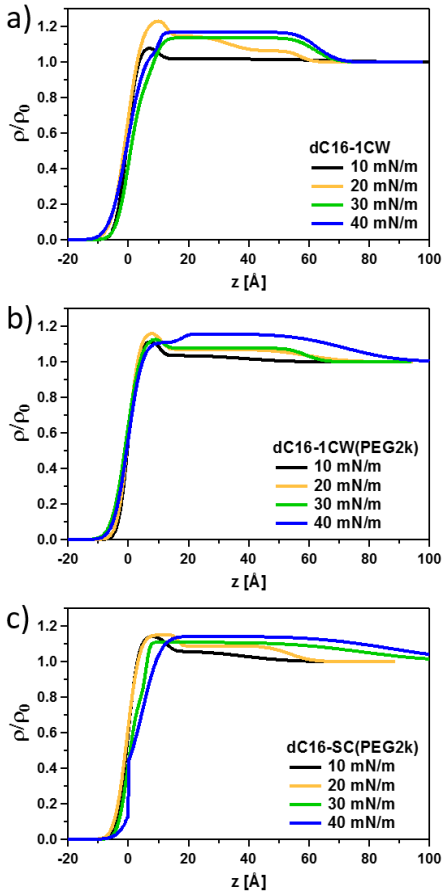

Figure 4.3. Density profiles along the air-water interface obtained by model fits of the data displayed in Figure 2 for a) dC16-1CW, b) dC16-1CW(PEG2k), and c) dC16-SC(PEG2k).

First, the lowest pressure at 10 mN/m for all three amphiphiles indicate an accumulation of amphiphiles occupying a thickness of about 10 Å at the interface. This corresponds to the diameter of a single helix indicating that the peptides are lying flat on the surface as non-bundled single helices. The alkyl chains are likely to be oriented up in the air occupying the portion of the surface with electron densities in the parts where ρ/ρ_0 is less than about 0.8. The rather thin layer indicates that the alkyl chains are collapsed and lie in the plane of the air-water interface. At 20 mN/m, the total thickness of the film increases to ~ 50 – 60 Å. The thickness of this layer corresponds well to the length of the helices indicating that the peptides now are oriented normal to the interface. Upon increasing the pressure to 30 mN/m and subsequently 40 mN/m, the electron density increased to about $\rho/\rho_0 \approx 1.15$, indicating increased packing of peptide-polymer conjugate amphiphiles at the interface. The electron density is smaller than what was expected for a layer of pure peptides ($\rho/\rho_0 \approx 1.34$) suggesting that the peptides pack with a volume fraction of about 0.44, the rest being water. It is interesting to compare this to the maximum packing fraction[49] achievable with hexagonal packing of aligned cylinders of 0.9. Hence, water still considerably swells the peptide helices at high pressure indicating a significant hydration as well as inefficient

packing due to bundle formation, imperfect parallel cylinders etc. This finding is in good agreement with our recent small-angle neutron scattering contrast variation study that showed ~85% of 3HM is composed of water[26].

The main difference between the PEGylated and non-PEGylated dC16-1CW amphiphiles, is the more pronounced and well-defined layer in the case of the non-PEGylated peptide. For dC16-1CW(PEG2k), the electron density decreases more gradually towards the interior (bottom) of the film indicating more inhomogeneous packing at the interface. For the amphiphile comprised of the scrambled peptide sequence, the behavior looks rather different and the density profiles are generally much broader indicating that the peptide amphiphiles adsorbs like amphiphilic polymers due to the absence of α-helices and bundle formation. The layer structure is not as well-defined and the segments are more statistically distributed at the interface in a more diffuse manner resembling the monolayer structure of polymers previously observed[50-53].

4.2.3 Grazing-incidence X-ray diffraction (GIXD)

Reflectivity provides out-of-plane (z-direction) information of the film at the air-water interface. Grazing incidence diffraction at the air-water surface provides information on the in-plane (xy-direction) structure and will therefore reveal any ordered structure formation such as bundling of the peptides to form coiled-coil structures. Figure 4.4 shows the GIXD spectra as a function of the in-plane wavevector momentum transfer, Q_{xy}. No significant Q_z-dependence was found and thus the spectrum was integrated over a constant region.

Figure 4.4 shows the presence of well-defined Bragg peaks at 40 mN/m for both dC16-1CW amphiphiles regardless of the presence of PEG2k. However, dC16-SC(PEG2k) did not exhibit any Bragg peaks even at the highest surface pressure studied of 40 mN/m. Thus, there is no evidence of 2-D structures found for the amphiphile containing the scrambled peptide sequence. The monotonic decay of the GIXD profile for dC16-SC(PEG2k) could be described by a power-law decay in the form of $I \sim Q_{xy}^{-0.6}$. Such power-law decay, $I \sim Q_{xy}^{-\alpha}$, is expected for capillary waves. $I \sim Q_{xy}^{-2}$ power-law has been found for air-water interfaces without additives (pure water). A smaller exponent can be potentially influenced by experimental smearing effects. In this work, we are not concerned with surface fluctuations and $I \sim Q_{xy}^{-0.6}$ is used as a simple phenomenological description in order to subtract any contributions from capillary waves to the coherent signal from peptide in-plane structure. In order to further analyze the data, the $I \sim Q_{xy}^{-0.6}$ background signal deduced from the dC16-SC(PEG2k) data was subtracted from those of dC16-1CW with and without PEG2k. The results are shown in Figure 4.5 for the two respective amphiphiles at surface pressures of 30 mN/m and 40 mN/m.

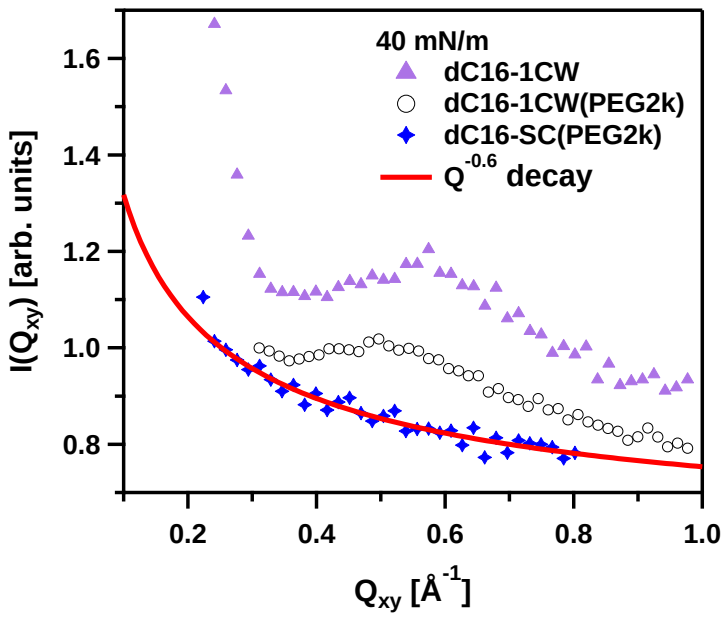

Figure 4.4. Integrated GIXD data showing the Q_{xy}-dependence of the in plane scattering of the three amphiphiles at a surface pressure of Π=40 mN/m. The line displays a fit to a power-law reflecting the diffuse scattering characterizing the capillary wave fluctuations. Note that a predominant peak is visible for the α-helical forming peptide-conjugates but not for scrambled dC16-SC(PEG2k).

GIXD data of dC16-1CW amphiphiles in Figure 4.5a show a well-defined peak in the range of 0.5 – 0.6 Å^{-1} indicating well-defined lateral ordering at the interface. The data at both surface pressures of 30 mN/m and 40 mN/m can be well-described by the presence of only perpendicularly aligned 3-helices (f_3 =1) at the air-water interface. The peaks at Q_{xy} ~ 0.557 Å^{-1} at 30 mN/m and Q_{xy} ~0.596 Å^{-1} at 40 mN/m correspond to inter-helical spacings of d ~ 11.3 Å and d ~ 10.5 Å, respectively. The value observed for 30 mN/m is in excellent agreement with the results from solution SAXS[18, 21] where an inter-helical distance was found to be about 11.6 Å. This small reduction in the inter-helical distance at 40 mN/m suggests more severe compression of the helices within the 3-helix bundle in the absence of PEG.

The dotted line in Figure 4.5 illustrates a similar GIXD peak position for dC16-1CW(PEG2k) at both 30 mN/m and 40 mN/m to that of its non-PEGylated counterpart at 30 mN/m. The inter-helical distance corresponds to about 11.5 Å. The absence of surface pressure dependence on the inter-helical distance of dC16-1CW(PEG2k) indicates that the PEG chains do act as "springs". Steric repulsion of the PEG chain mediates the inter-bundle interactions and prevents compacting of the helices within the coiled-coil bundle. Although the pressure dependence on the inter-helical distance was not found for dC16-1CW(PEG2k) at 30 mN/m and 40 mN/m, the shape of the GIXD profiles appears to be slightly different at

the two pressures, indicating some differences in the coiled-coil structures formed at the surface under various surface compressions.

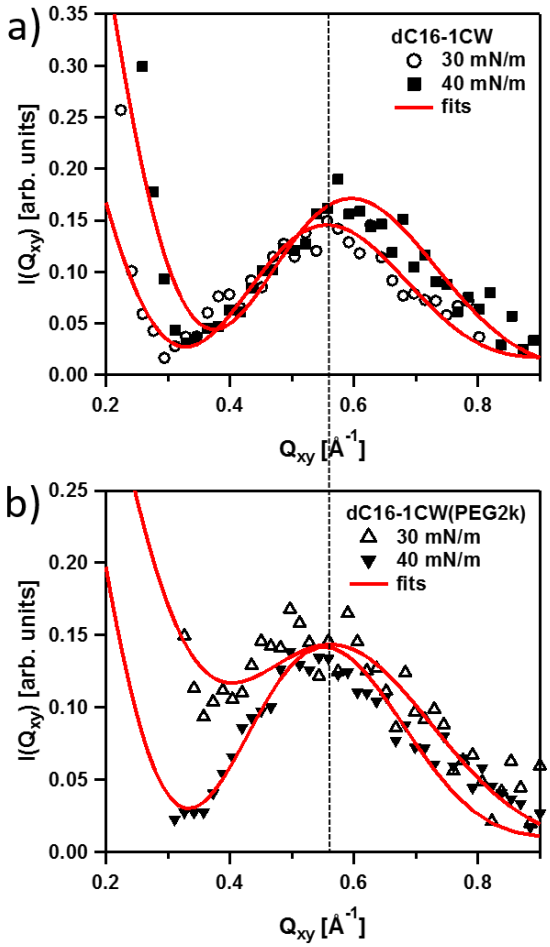

Figure 4.5. GIXD data showing the Q_{xy}-dependence of the in plane scattering of a) dC16-1CW and b) dC16-1CW(PEG2k) at surface pressures of 30 and 40 mN/m. The solid lines represent fits using the bundle model described in the text.

Detailed modeling of the GIXD spectra was performed to understand this behavior. A similar approach to previous solution SAXS description of coiled-coil/polymer conjugates was used. The model consisted of a collection of parallel cylinders to describe the helices and attached Gaussian chains to model the PEG chains. For simplicity, a two state model was used – either perpendicular or parallel perfectly aligned bundles relative to the air-water interface. Contributions for cylinders or bundles lying perfectly parallel to the surface are not expected to give a coherent signal in Q_{xy} as the scattering correlations along the length of the cylinder is parallel to Q_z. Using this model, we allowed the peptide to form single helices,

dimers (2-helices), or trimers (3-helices). The data in Figure 6 were fitted to mixtures of 1-, 2- and 3-helices (Eq. 4.4).

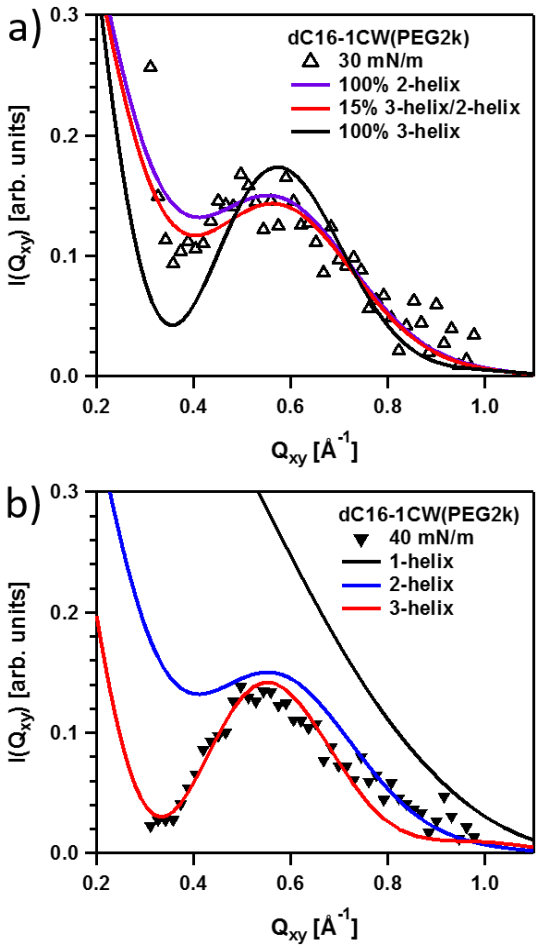

Figure 4.6. A comparison of fit results using 2-helix/3-helix bundles and mixtures of the dC16-1CW(PEG2k) data at a) 30 mN/m and b) 40 mN/m.

The fit results in Figure 4.6a reveal that at 30 mN/m the data can be better described by a predominant fraction of 2-helix rather than 3-helix bundles. The best fits to the data indicate that 85% 2-helix rather than a 100% 2-helix bundle composition applies to the surface oligomeric state at 30 mN/m. Attempting to fit the data assuming a composition of 100% 3-helices returned a significantly worse fit, especially at low Q_{xy}. At 40 mN/m, the results in Figure 4.6b show the data are better fitted by 100% 3-helix composition. This result indicates that complete coiled-coil bundle formation in the presence of conjugated PEG can be promoted under high compressions.

Klok and coworkers have found that α-helical coiled-coil peptides retain their structures upon PEGylation[29, 30]. PEGylation has been also found to adversely affect β-sheet

formation from the conversion of α-helix within an alanine-rich peptide at elevated temperatures[54]. Nanotubes were formed by PEGylation of tetraphenylalanine due to formation of anti-parallel β-sheets and π-π-stacking[55]. As the PEG chain length increased, the nanotubes were observed to transition into fibrils[56]. The delicate interplay between steric hindrance of the conjugated PEG and inter- and intra-molecular interactions of the peptide governs the self-assembly of hybrid peptide-PEG materials. Here, at intermediate pressures (~30 mN/m), un-PEGylated amphiphiles completely form 3-helix bundles whereas the PEGylated amphiphile exhibited mostly 2-helix formation. The observed differences between the dC16-1CW and its PEGylated analogue can be attributed to steric hindrance of the polymer chains within the monolayer. At higher pressures (40 mN/m), the inter-peptide distance is supposed to be shorter and may contribute to complete 3-helix structure formation for both dC16-1CW and dC16-1CW(PEG2k). The non-PEGylated analog displayed slight compression of the helices within the coiled-coil bundle. While the conjugated PEG chain may mediate the lateral pressure and avoid the lateral compression of helices.

§ 4.3 Conclusion

In summary, we studied two important parameters – peptide structure and effect of PEGylation – in governing the oligomeric state and self-assembly process of coiled-coil peptide-polymer conjugate amphiphiles at the air-water interface. Combining the results from Langmuir isotherm, XR, and GIXD measurements, coiled-coil formation is highly dependent on peptide structure. PEGylated 3-helix amphiphiles exhibited a surface pressure dependent transition from a mixture of dimers and trimers at intermediate pressure to complete trimers at high pressure. Furthermore, the PEGylated 3-helix amphiphile was able to preserve the inter-helical distance at high surface pressure whereas the non-PEGylated analog experienced a slight decrease in the inter-helical distance upon high surface compression. The results shown here illustrate the role of peptide structure and PEGylation in the self-assembly process and oligomeric state of amphiphilic peptide-polymer conjugates in a Langmuir monolayer. Coiled-coil bundles are a promising strategy to generate ligands presented in a well-defined oligomeric state for high affinity, high specificity ligand-receptor applications.

§ 4.4 Experimental methods

4.4.1 Synthesis and purification of amphiphiles

The amphiphiles were synthesized using synthetic routes described previously[20]. Briefly, 1CW (EVEALEKKVAALESKVQALEKKVEALEHGW) and SC (EGKAGEKAGAALKSGVQELEKGAEAGEGGW) peptides were synthesized using solid phase peptide synthesis. The N-terminus of the peptides were modified with a 6-(Fmoc-amino)hexanoic acid linker and the alkyl tails were conjugated to the N-terminus of the peptide through reaction of palmitic acid (C16) with deprotected Fmoc-Lys(Fmoc)-OH to generate a branched alkyl tail. Cleavage of the amphiphile was achieved using a cocktail of 90:5:5 TFA/TIS/H_2O for 3 hours. The crude peptide was precipitated and washed in cold ether, isolated, and dried in vacuo. For amphiphiles with side-conjugated PEG2k, S14C

mutations were performed to facilitate the site-specific coupling of maleimide-functionalized polyethylene glycol (PEG) of molecular weight 2000 g/mol to the middle of the peptide sequences (Scheme 4.1). The resulting amphiphiles were purified using HPLC (Beckman Coulter) on a C4 column (Vydax) using a gradient of water:acetonitrile (A:B) in the presence of 0.1% TFA from 30% B to 100% B in 30 minutes at a flowrate of 8 mL/min. The purified non-PEGylated amphiphile fraction was collected at ~90% B whereas fractions of PEGylated amphiphiles were collected at ~85% B.

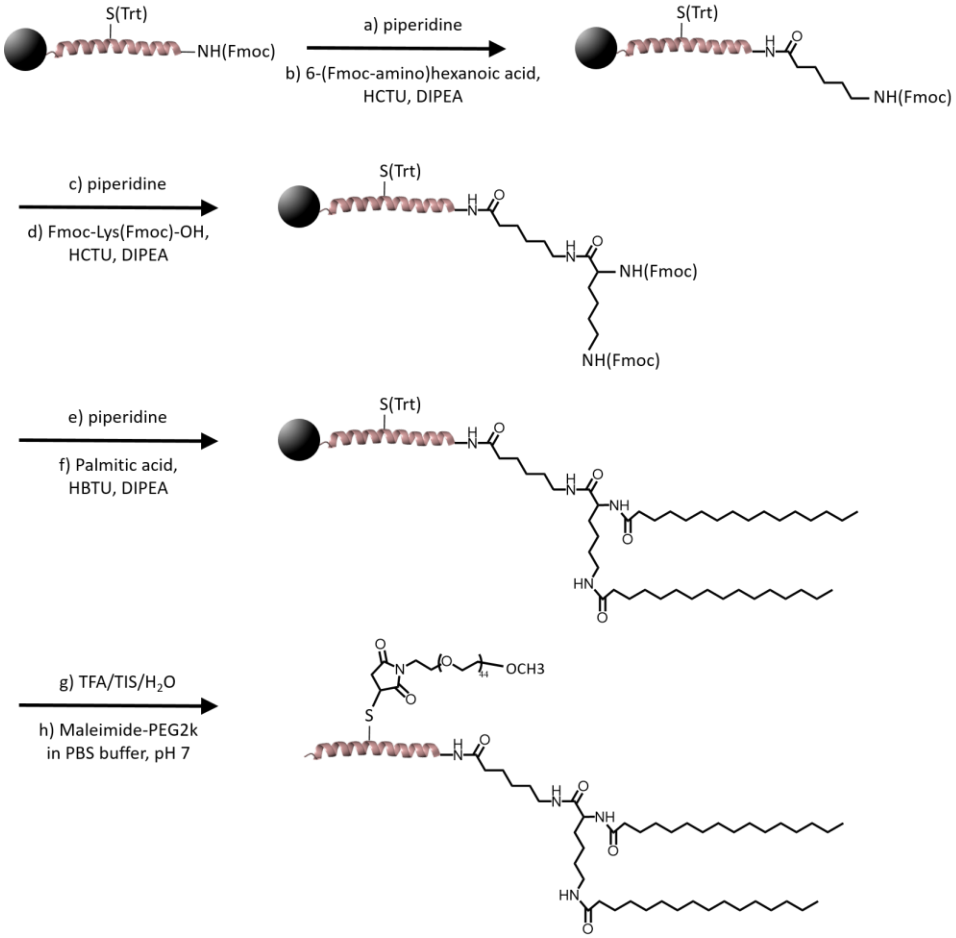

Scheme 4.1. Synthetic scheme of amphiphilic peptide-polymer conjugates. For PEGylated conjugates (dC16-1CW(PEG2k) and dC16-SC(PEG2k)), S14C mutation was used to facilitate site-specific coupling of PEG2k. For non-PEGylated dC16-1CW, residue 14 of the peptide sequence remained as serine and step (h) of the synthetic scheme was not performed.

4.4.2 Langmuir monolayers

Isotherms were collected using a KSV 2000 Langmuir trough (Biolin Scientific) on a vibration isolation table. Typically, a ~100 µM solution of amphiphile dissolved in methanol was used to spread onto a phosphate buffer (25 mM, pH 7.4) subphase. To promote the

formation of a monolayer, a microliter glass syringe (Hamilton) was used to deposit the solution dropwise at the thin film of water provided by the meniscus that forms over a glass capillary penetrating the air-water interface at an oblique angle. The monolayer was allowed to equilibrate for 10 min before compression begins at a rate of 10 mm/min. The surface pressure defined as $\Pi = \gamma_0 - \gamma$ was measured as a function of surface area assuming a monolayer and was monitored using a platinum Wilhelmy plate.

4.4.3 Liquid surface XR and GIXD

XR and GIXD were performed at the 15ID-C Liquid Surface Scattering Beamline/ChemMatCARS[57] of the Advanced Photon Source/Argonne National Laboratory (APS/ANL) using monochromatic 10 keV x-rays. For XR measurements, the spectrometer was kept in the reflectivity condition, where $\delta = \beta$, to collect the photons scattered with momentum transfer perpendicular to the liquid surface ($Q_z = 4\pi \sin(\delta)/\lambda$). The high brilliance of the x-ray beam at APS provides high-quality XR data from 0.018 to 0.6 $Å^{-1}$. For GIXD measurements, the incident angle was set such that $Q_z = 0.016$ $Å^{-1}$, below the critical angle of water ($Q_z = 0.0217$ $Å^{-1}$). GIXD was scanned in the region $3.5° < 2\theta_{xy} < 11.1°$ which corresponds to $0.31 < Q_{xy} < 0.98$ $Å^{-1}$. After deposition of the monolayer as described above, the monolayer was allowed to equilibrate for 10 min. Compression was carried out at 10 mm/min until the desired target surface pressure was achieved, then constant pressure was maintained during the XR measurements. The trough was translated 1 mm transverse to the beam to expose a fresh portion of the sample to the beam after each reflectivity scan and thereby avoided any potential radiation damage to the monolayer.

4.4.4 XR data reduction and analysis

The reflectivity is calculated by subtracting the measured background intensity from the specular beam intensity, and then normalizing to the incident beam intensity measured by a detector placed before the sample. The fits were performed with a self-consistent approach using the program "Stochfit"[58]. First, the reflectivity data were analyzed using a model independent approach where layers were subdivided into typically 40 sublayers and a (non-unique) solution was found by using a stochastic search algorithm. The advantage of the program is that only the overall thickness needs to be assumed. However, the disadvantage is that the solution is likely to give unphysical oscillations. Thus the obtained density profile was only used as a guide for further modeling. Next, this density profile was fitted using a simpler box model with a minimal number of layers (two or in a few cases, three). Subsequently, the obtained density profile was used to calculate the reflectivity curve and compared to the experimental data. Finally, refinements to the fitted curves were made by a slight variation of the parameters until a satisfactory agreement was found.

In most cases, the data could be described reasonably well using two layers by which five parameters are involved: thickness of each layer, t_i, a Gaussian width describing the roughness of the air-water surface, $\sigma_{a\text{-}w}$, between the layers σ_j, and the layer-subphase interfacial width, σ_{sub}. In some cases, satisfactorily fits could only be achieved by adding a third layer and thus two additional parameters were added (t_{j+1} and σ_{j+1}).

4.4.5 Theoretical modeling of GIXD data

Analytical Form Factor of aligned α-Helical Bundle-forming Peptide-Polymer Conjugates
Cylinders aligned perpendicular to the air-water interface was used to facilitate the description of the α-helical forming peptides. Furthermore, we assume only single scattering events. For a single cylinder assuming any orientation we have:

$$P(Q)_{cyl} = \int_0^{\pi/2} \left| A(Q,\alpha)_{cyl} \right|^2 \sin\alpha d\alpha \,, \qquad \text{(Eq. 4.1)}$$

where $A(Q,\alpha)_{cyl} = \frac{2J_1(QR\sin\alpha)}{QR\sin\alpha}\frac{\sin(QL\cos\alpha)}{QL\cos\alpha}$

where R and L are the radius and length of the cylinder, α is its angle to the scattering vector Q, and $J_1(x)$ is the first order Bessel function.

For GIXD experiments, we only consider the Q-component in the plane of the surface, Q_{xy}. Eq. 4.1 can be significantly simplified by assuming that the cylinder is perfectly aligned perpendicular to the interface. Thus we set $\alpha = \frac{\pi}{2}$ and obtain:

$$P(Q_{xy})_{cyl} = \left(A_{cyl}(Q_{xy})\right)^2, A_{cyl}(Q_{xy}) = \frac{2J_1(Q_{xy}R)}{Q_{xy}R} \qquad \text{(Eq. 4.2)}$$

As in our previous work[18] to describe solution small-angle scattering data, we employed a model describing the peptide-polymer side-conjugates as cylinders with polymer chains grafted to the sides, where the cylinders assemble into bundles with oligomeric states of either dimers or trimers. In this case contributions from polymer chains, which nevertheless decay at lower Q, are disregarded.

Assuming that the 3-helix bundles are arranged in a trigonal (equilateral) arrangement, we obtain:

$$S(Q)^{(i)}_{bundle} = \begin{cases} \frac{1}{4}\cdot(2+2J_0(2QRf)) & 2-helix \\ \frac{1}{9}\cdot(3+3J_0(2QRf)) & 3-helix \end{cases} \qquad \text{(Eq. 4.3)}$$

The scattering from an arbitrary mixture of 2-and 3-helix bundles, together with single helix peptide-polymer conjugates of fractions f_2, f_3, and $(1- f_2-f_3)$, respectively, can then be written as:

$$I(Q)_{bundles} = C\cdot\varphi\cdot P_{cyl}(Q)\cdot\left[(1-f_2-f_3)+2f_2S(Q)^{(2)}_{bundle}+3f_3S(Q)^{(3)}_{bundle}\right] \qquad \text{(Eq. 4.4)}$$

where φ is the total volume fraction and f_1, f_2, and f_3, are the fractions of 1-, 2-, and 3-helices respectively. Since the GIXD measurements were not performed on an absolute intensity scale a scaling constant, C, was included.

Chapter 5

Kinetic Pathway of 3-Helix Micelle Formation

A subtle but highly pertinent factor in the self-assembly of hierarchical nanostructures is the kinetic landscape. Self-assembly of a hierarchical multicomponent system requires the intricate balance of non-covalent interactions on a similar energy scale that can result in several self-assembly processes occurring at different timescales. We seek to understand the hierarchical assemblies within an amphiphilic 3-helix peptide-PEG-lipid conjugate system en route to the formation of highly stable 3-helix micelles (3HMs). 3HM self-assembles through multiple parallel processes – helix folding, coiled-coil formation, micelle assembly, and packing of alkyl chains. Our results show that the kinetic pathway of 3HM formation is mainly governed by two confounding factors: lateral diffusion of amphiphiles to form coiled-coils within the micelle corona and packing of alkyl tails within the hydrophobic micelle core. 3HM has exhibited highly desirable attributes as a drug delivery nanocarrier; understanding the role of individual components in the kinetic pathway of 3HM formation will allow us to exert better control over the kinetic pathway, as well as to enhance future design and eventually manipulate the kinetic intermediates for potential drug delivery applications.

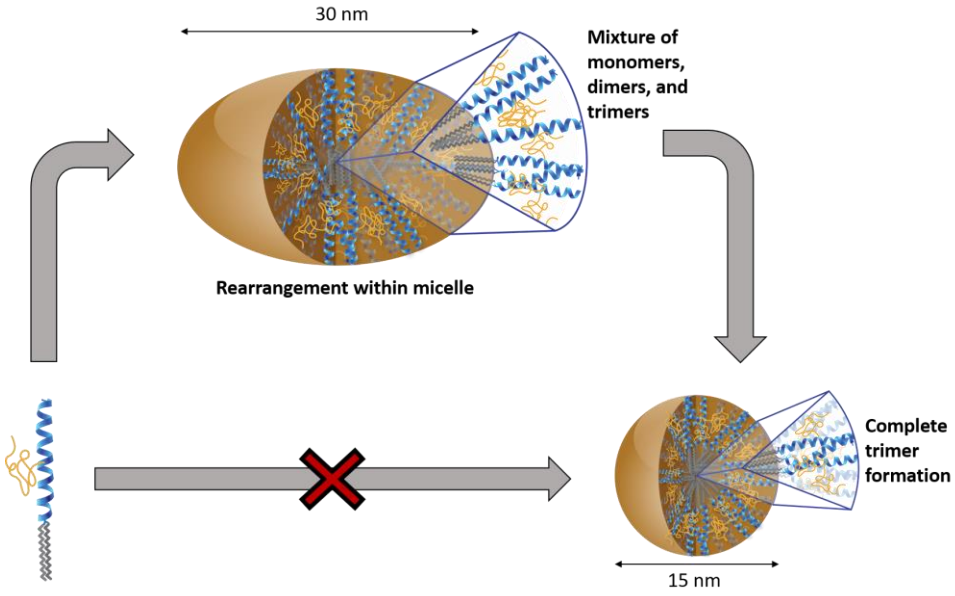

§ 5.1 Introduction

Solution self-assembly of molecular amphiphilic building blocks offers an efficient, bottom-up approach to generate well-defined nanostructures[1-3]. Self-assembly of multicomponent systems have competing interactions at similar energies and at hierarchical lengthscales which dictates the kinetics of formation and overall energy of the system[4-10]. Delineating the contributions of individual components to the self-assembly energy landscape of multicomponent systems will greatly enhance our understanding of the kinetic pathway and is crucial to exert control over the properties of the system[11-17]. Size and kinetic stability are important design parameters to consider in nanotechnological applications[18, 19]. Specific to drug delivery, these factors critically influence a nanocarrier's pharmacokinetics,

biodistribution, tissue penetration, and cellular uptake[20-23]. Fundamental understanding of the energy landscape as well as the dynamics of synthetic self-assembled nanoparticles is imperative when interfacing them with biological systems *in vivo*.

We have developed uniform, sub-20 nm 3-helix micelles (3HMs) based on hierarchical self-assembly of hybrid 3-helix peptide-polyethylene glycol (PEG) conjugate amphiphiles[24-29]. While PEGylated nanoparticles require additonal surface modifications[30] such as polysorbate 80 or ligands that target active blood-brain barrier (BBB) transporters, 3HM is the only PEGylated nanocarrier to be able to effectively penetrate the BBB without further surface modification for drug delivery[31]. Moreover, 3HM accumulates within GBM tumors significantly greater than stealth liposomes[31]. In non-human primates studies, 3HM displayed perfusive distribution in brain regions through cerebrospinal fluid (CSF) delivery[32]. Local administration to rat stratium through convection-enhanced delivery (CED) of doxorubicin (DOX)-loaded 3HM showed broader and more homogeneous distribution compared to free DOX[26]. In rodents, 3HM exhibited long circulation (29.5 hr) and favorable biodistribution with low accumulation in major reticuloendothelial system organs such as the liver, spleen, and kidneys[24]. Time-dependent positron emission tomography (PET) of intraveneously administrated DOX-loaded 3HM showed that 3HM is highly mobile within tumors[26]. The desirable *in vivo* behavior of 3HM highlights the unique kinetic stability of 3HM due to multicomponent self-assembled interactions at the molecular level.

Self-assembly of uniform and highly stable 3HM is instructed by the information encoded within the multicomponent peptide-PEG-lipid conjugate building block. We have thus far been able to tailor the kinetic stability of 3HM by changing various parameters such as alkyl length[27], peptide structure[25], and PEG conjugation position[28]. However, the kinetic pathway of 3HM is not yet understood and knowledge of 3HM formation is complicated to uncover as there are numerous factors that influence the assembly pathway. Energetic contributions of competing interactions such as enthalpy of alkyl packing[27], entropic repulsion of side-conjugated PEG[25, 28, 29], interaction between PEG and the peptide[33, 34] are of similar magnitude, which can lead to formation of non-equilibrium states in the system. Self-assembly of 3HM requires a delicate balance of attractive and repulsive non-covalent interactions on a similar energy scale, albeit on multiple lengthscales – folding of peptides into helices, association between helices to form coiled-coil tertiary structure, and assembly of amphiphilic subunits into micelles. We seek to understand these competing interactions that contribute to the equilibrium self-assembled structure of 3HM and thereby bridge the gap between fundamental understanding of the 3HM assembly process and the excellent biological performance of 3HM.

Presently, our results show that time-dependent molecular reorganization of the amphiphilic subunits is directed by the formation of 3-helix coiled-coils in the 3HM corona although alkyl length provides kinetic barriers for lateral diffusion within the micelle during the rearrangement process. Micelle kinetic stability improved as a function of time through exchange of subunits with other micelles and intramicellar reorganization. Decoupling the role of the individual components in the kinetic pathway of 3HM is imperative to understand and exploit for the design of future peptide-polymer-lipid conjugate nanocarriers.

§ 5.2 Results and discussion

We systematically investigated the temporal evolution of 3HM by preparing the following samples of 3HM – freshly prepared, 1 day, and 1 week at room temperature after dissolution of the lyophilized 3HM powder into phosphate buffer solution. Furthermore, we compared the properties of 3HM solutions after various incubation times at room temperature with that of an annealed (heat to 70°C, gently cool down) 3HM sample which represents the thermodynamic equilibrium of the system[25]. The molecular contributions of alkyl chain packing in the micelle core, amphipathic formation of coiled-coil in the micelle corona, and amphiphilic subunit desorption were studied to decouple their individual contributions to the overall energy landscape of hierarchical 3HM assembly.

5.2.1 Alkyl packing in hydrophobic core

Micelle formation is strongly driven by the tendency of hydrophobic alkyl chains to self-associate and the stability of micelles is highly correlated to the thermal phase behavior of the hydrophobic alkyl core[27, 28, 35, 36]. DSC was employed to study the thermal phase transition and alkyl chain packing within the hydrophobic core of 3HM as a function of incubation time at room temperature. Figure 5.1 shows the time-dependence of 3HM(C16) and 3HM(C18) alkyl phase transitions. DSC measurement of a freshly dissolved lyophilized 3HM(C16) powder into PBS yielded two poorly resolved peaks at 15°C and 25°C. A fresh solution of 3HM(C18) yielded a broad endothermic peak that can be deconvoluted into two transitions, 31°C and 37°C, at higher temperatures than the C16 analog which is consistent with the longer alkyl chain length. The observation of two phase transitions for both C16 and C18 micelles is indicative of alkyl chain splaying[25, 28, 35] within the hydrophobic core of 3HM.

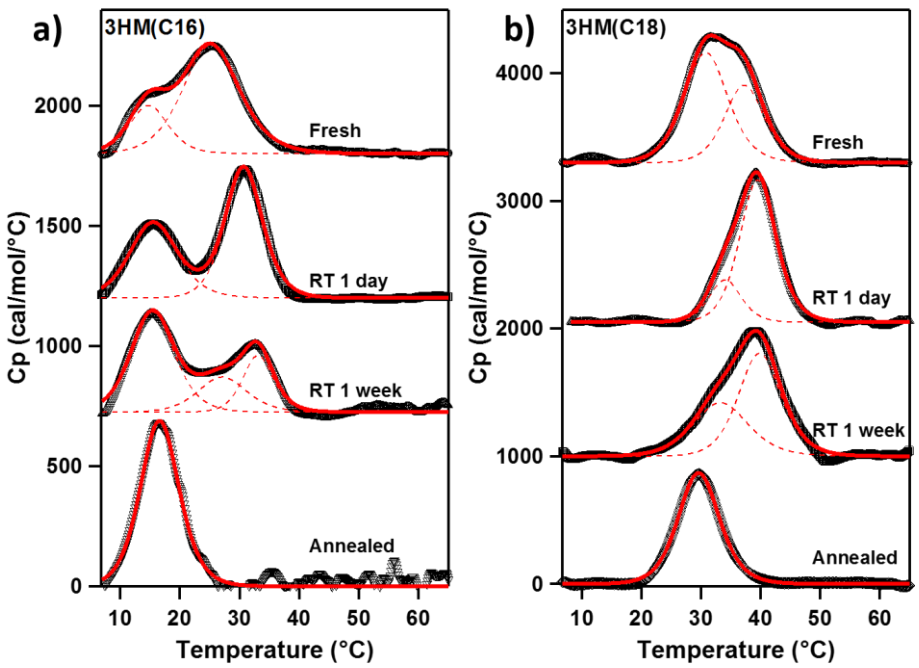

Figure 5.1. DSC measurements of (a) 3HM(C16) and (b) 3HM(C18) after various thermal equilibration times: freshly prepared, 1 day, 1 week, and annealed. Data are shown in black, fits to the data in red solid lines, and deconvolution of the fits are in red dotted lines.

Table 5.1. Alkyl transition temperatures and total enthalpy of transitions for various thermal treatments of 3HM(C16) and 3HM(C18) corresponding to Figure 5.1.

	3HM(C16)		3HM(C18)	
	T_m (°C)	ΔH (kJ/mol)	T_m (°C)	ΔH (kJ/mol)
Fresh	15, 25	31.2 ± 0.3	31, 37	57.8 ± 1.3
RT 1 day	16, 31	31.0 ± 0.2	33, 40	53.8 ± 3.6
RT 1 week	16, 27, 33	30.3 ± 3.2	34, 40	47.9 ± 1.4
Annealed	17	25.1 ± 0.1	30	33.5 ± 0.1

As the 3HM(C16) and 3HM(C18) solutions were allowed to stand at room temperature over a period of a day or a week, the relative intensities of the two respective phase transitions undergo different evolutions. The lower temperature peak of 3HM(C16) at ~15°C intensifies from 7.3 ± 0.1 kJ/mol (fresh) to 13.0 ± 0.1 kJ/mol (1day) then 16.9 ± 0.4 kJ/mol (1 week) while the higher temperature transition decreased from 23.8 ± 0.2 kJ/mol (fresh) to 18.0 ± 0.1 kJ/mol (1 day) then 13.4 ± 2.8 kJ/mol (1 week). However, 3HM(C18)

experienced an intensification of the transition at the higher temperature of ~40°C from 22.3 ± 0.6 kJ/mol (fresh) to 31.3 ± 3.6 kJ/mol (1 day) then 38.0 ± 0.7 kJ/mol (1 week) whereas the lower temperature transition decreased over time from 35.5 ± 0.6 kJ/mol (fresh) to 21.7 ± 3.7 kJ/mol (1 day) then 9.9 ± 0.7 kJ/mol (1 week). Finally, thermal annealing of the samples at 70°C, then slowly cooling led to a single transition for both 3HM(C16) and 3HM(C18) at 17°C and 30°C, respectively. Moreover, the total enthalpy associated with the phase transitions decreased as a function of incubation time for both 3HM(C16) and 3HM(C18) as shown in Table 5.1.

The stark difference in behavior of melting transitions as a function of equilibration time between C16 and C18 alkyl chains of 3HM is indicative of the different kinetic pathway during the micelle assembly process. Conjugation of alkyl chains to a bulky headgroup leads to depression of the alkyl melting temperature (T_m)[25, 35, 37]. We have previously shown that tertiary structure of the headgroup affects the melting temperature of alkyl chains in peptide-polymer-lipid conjugate micelles[25]; alkyl chains attached to monomeric helix headgroup resulted in T_m of ~32°C whereas a trimeric coiled-coil headgroup resulted in T_m of ~17°C. Based on our results here, the transition at T_m ~25°C is likely to be that of a dimeric species. For 3HM(C16), the intensification of the lower T_m transition as a function of time suggests that there is sufficient mobility of the amphiphile subunits within the micelle to diffuse laterally at room temperature, thereby shifting the population of micelles to the lower T_m transition, forming 3-helix bundles within the corona of 3HM. However, 3HM(C18) displayed the opposite behavior, with the higher T_m transition at ~40°C increasing as a function of time indicative of the inability of C18-micelles to overcome the kinetic barrier imposed by the more hydrophobic character of C18 alkyl chains. Thermal annealing of 3HM(C18) at elevated temperature provides the subunits with sufficient mobility to reorganize the alkyl chains, resulting in the annealed sample having a single homogeneous T_m at ~30°C.

5.2.2 Subunit desorption kinetics

The kinetic stability of 3HM(C16) after various incubation time was assessed by tracking the recovery in fluorescence intensity of FAM-labeled 3HM(C16) after addition of excess non-labeled 3HM(C16)[28]. An increase in fluorescence intensity corresponds to an attenuation in fluorescence self-quenching, suggesting that the FAM-labeled amphiphiles are further apart than the Forster radius and unable to effectively quench the fluorescence emitted from a neighboring fluorophore. Figure 5.2 shows that as equilibration time of 3HM(C16) at room temperature was increased, the rate of fluorescence recovery decreased. Freshly dissolved 3HM showed ~38% increase in fluorescence intensity whereas a day old 3HM showed ~15% increase, and finally annealed 3HM showed only ~8% increase in fluorescence intensity over the same 4-hour period. Since the Forster radius of fluorescence self-quenching for fluorescein[38] is ~4–5 nm, the increase in fluorescence intensity suggests that the labeled amphiphiles are being redistributed to other micelles in solution during the incubation period. Assuming that the rate-limiting step is subunit desorption, the fluorescence intensity can be fitted using Eq. 5.1 with two first-order dissociation constants:

$$I(t) = I(\infty) + [I(0) - I(\infty)][fe^{-k_1 t} + (1-f)e^{-k_2 t}] \quad \text{(Eq. 5.1)}$$

The first rate constant, k_1, accounts for the initial dilution of the labeled micelles with non-labeled micelles. The second rate constant, k_2, represents subunit desorption from labeled micelles into non-labeled micelles. Fitting of the recovery data provided rate constants of 9.01 x 10^{-4}, 5.64 x 10^{-4}, and 2.05 x 10^{-4} min^{-1} at 20°C and first-order half-lives of 12.8, 20.5, and 55 hr for fresh, 1 day, and annealed 3HM(C16), respectively. This result indicates that freshly prepared 3HM is in a non-equilibrium state, and the subunits have high mobility and experience much higher rates of subunit desorption. As the 3HM(C16) samples were allowed to stand at room temperature for an extended period of time, the subunit desorption rate decreases and the kinetic stability of 3HM(C16) is dramatically improved.

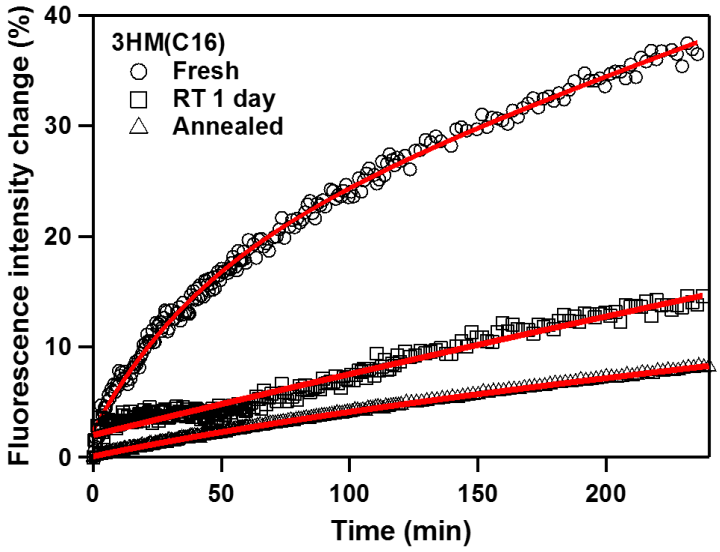

Figure 5.2. Temporal evolution of fluorescence recovery of fluorescein-labeled 3HM(C16) upon addition of non-labeled 3HM(C16). Fresh (circles), 1 day (squares), and annealed (triangles) data were fitted to first-order exchange kinetics (red solid lines) and rate constants obtained.

To obtain the energy required for subunit desorption, temperature-dependent fluorescence recovery of annealed 3HM(C16) was conducted as shown in Figure 5.3. Increasing the temperature led to more rapid exchange of the fluorescently-tagged subunits with other non-labeled micelles, leading to an increase in fluorescence intensity. Fitting of the fluorescence recovery data yielded 1.16 x 10^{-5}, 1.41 x 10^{-5}, 2.01 x 10^{-5}, and 6.90 x 10^{-4} min^{-1} corresponding to 45, 50, 55, and 65°C, respectively. The first-order rate constants obtained at the various temperatures can be fitted using the Arrhenius relation, Eq. 2, with an activation energy:

$$k = A\exp(-\frac{E_a}{RT}) \quad \text{(Eq. 5.2)}$$

The activation energy, E_a, for subunit desorption from 3HM(C16) was found to be 137 ± 11 kJ/mol. This indicates that due to the unique headgroup tertiary structure, there is a significant energetic barrier to overcome for subunits to desorb from an assembled 3HM.

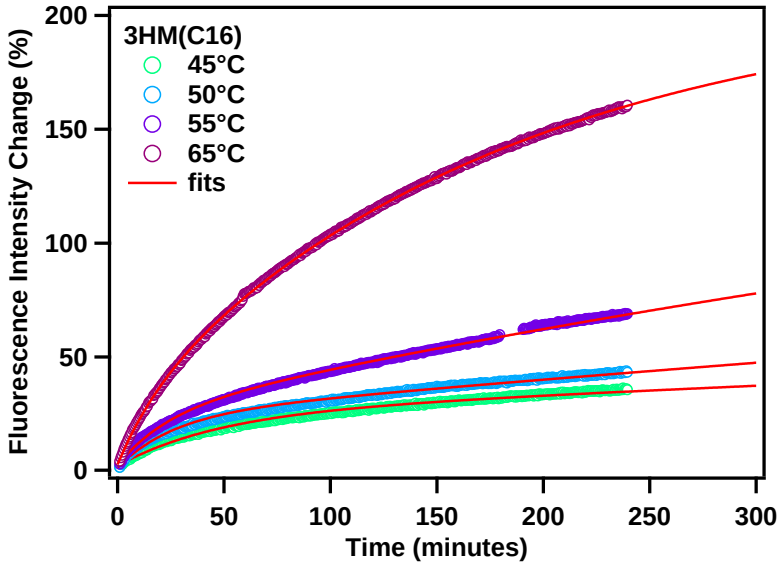

Figure 5.3. Temperature-dependent fluorescence recovery of annealed fluorescein-labeled 3HM(C16) upon addition of excess non-labeled 3HM(C16).

5.2.3 Temperature-dependent peptide secondary and tertiary structure

Next, to understand the time-dependence of the peptide secondary and tertiary structure upon fresh dissolution of 3HM, we studied the α-helical and coiled-coil content of 3HM(C16) using temperature-dependent CD. Figure 5.4a shows that for all samples, well-defined α-helices were formed at low temperatures, regardless of incubation time or thermal treatment. Moreover, the ratio of $\theta_{222}/\theta_{208}$, indicative of the presence of coiled-coils, was above 1 at temperatures below 60°C and did not fall below 0.86 for the entire range of temperature studied, shown in Figure 5.4b, indicating that the coiled-coils do not dissociate into single helices even up to 110°C. This result is consistent with previous studies of coiled-coil peptide-polymer conjugates in solution[39]. Even though $\theta_{222}/\theta_{208} \geq 1$ indicates formation of coiled-coils, it is unknown whether dimers or trimers are present. Coiled-coil formation is dependent on helical content, the high helical content observed here for 3HM solutions are likely to have a high degree of coiled-coil formation due to lateral pressure exerted on the amphiphiles[40] within the sterically confined environment of 3HM.

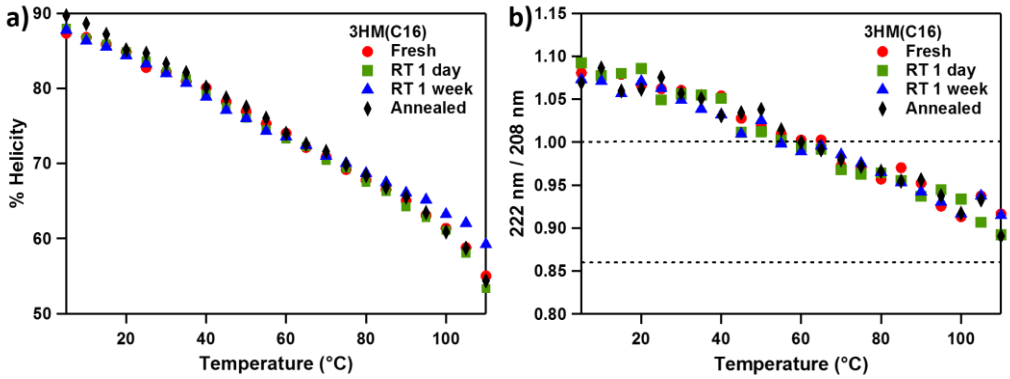

Figure 5.4. Temperature-dependent circular dichroism of 3HM(C16) after various thermal treatments. (a) Percentage helicity of 3HM(C16) and (b) $\theta_{222}/\theta_{208}$ of 3HM(C16), $\theta_{222}/\theta_{208} \geq 1$ indicates presence of coiled-coils and $\theta_{222}/\theta_{208} \leq 0.86$ indicates isolated helices. Freshly prepared (red circles), 1 day (green squares), and annealed (black triangles).

Dissociation constants of coiled-coils with 4 heptad repeats have been found to be in the nM to pM range[41] whereas the critical micelle concentration of 3HM had been determined to be ~4 μM[25]. Since the coiled-coil assembly has a lower dissociation constant than micelle formation, it seems probable that at least part of the monomeric helices self-associate to form populations of dimeric and trimeric coiled-coils before the self-assembly of amphiphilic subunits to form 3HM. The known experimental unfolding free energy of a similar trimeric coiled-coil was found to be ~77 kJ/mol per helix[42]. The free energy of unfolding the PEGylated coiled-coil in the corona of 3HM is presumably higher due to the stabilizing effect of PEG on the stability of α-helices. Our result indicates that the peptide-PEG-lipid conjugate forms α-helixes spontaneously upon dissolution of the lyophilized powder into aqueous solution and formation of a mixture of dimeric and trimeric coiled-coils ensues rapidly.

5.2.4 Size distribution

Figure 5.5a shows the size distributions of 3HM(C16) as a function of incubation time, measured by DLS. Freshly prepared 3HM(C16) solution had a mean hydrodynamic diameter of ~30 nm. A time-dependent decrease in the size of 3HM(C16) was observed from fresh (~30 nm) to 1 day (~25 nm) and one week (~20 nm) at room temperature. The size of 3HM(C16) as a function of time approaches that of the annealed sample. A similar time-dependent decrease in size was observed for 3HM(C18) (Appendix A.4.2). Fitting of SAXS measurements using a core-shell model, showed by the red lines in Figure 5.5b, displayed a similar decrease in the size of 3HM(C16) from fresh to one week then annealed (Table 5.2). The size of 3HM(C16) after one week again converges toward that of the annealed sample.

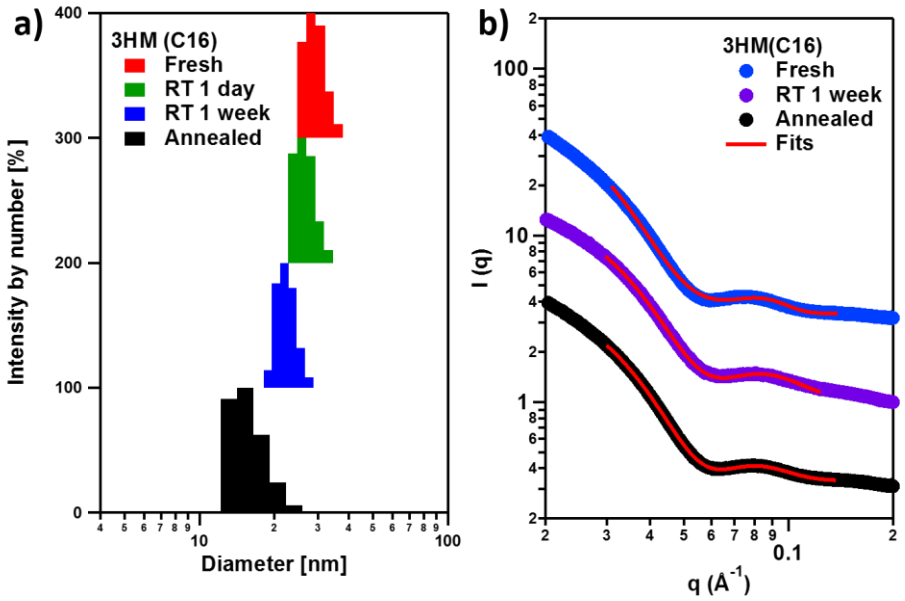

Figure 5.5. Size of 3HM(C16) as a function of time measured by (a) DLS and (b) solution SAXS. Red lines indicate best fit to the core-shell model. Data are vertically offset for clarity.

Table 5.2. Core-shell parameters from model fitting of SAXS data in Figure 5.5b.

Sample	Core radius (nm)	Shell thickness (nm)
Fresh	3.5	6.1
RT 1 week	2.5	4.1
Annealed	2.5	4.2

5.2.5 Effect of doxorubicin encapsulation on alkyl packing

To gain insight into the kinetic pathway of 3HM in the presence of a therapeutic cargo, the molecular interaction of 3HM with a model anticancer drug, DOX, was studied using DSC, CD, and DLS. DOX encapsulation within C16 and C18 micelles were 7.3 wt% and 8.8 wt%, respectively. DSC measurements of annealed 3HM(C16)-DOX in Figure 5.6a show a broad transition centered around 28°C, which is ~10°C above 3HM(C16) in the absence of DOX (Figure 5.1a). The increase in phase transition temperature upon encapsulation of DOX has previously been observed for the interaction of DOX with 3HM(C18)[26]. A similar result is observed here, in Figure 5.6b, where the transition temperature of 3HM(C18)-DOX (39°C) is 9°C higher than 3HM(C18) without DOX (30°C). DOX-encapsulation in both C16 and C18 analogs of 3HM resulted in ~10°C increase in the

transition temperature. However, the enthalpy associated with the phase transition for 3HM-DOX experienced a ~30% decrease (Table 5.3) compared to 3HM in the absence of DOX (Table 5.1). The increase in transition temperature yet depression in the enthalpy indicates that the coassembly of DOX with the alkyl chains of 3HM resulted in a distinct thermodynamic phase behavior different from that of the pristine 3HM in the absence of DOX. However, DLS (Appendix A.4.2) and CD (Appendix A.4.3) show that the size distribution and peptide structure of 3HM in the presence of DOX are very similar to that of pristine 3HM formulations without DOX. This further affirms our belief that the interaction of DOX with 3HM is strictly confined to the hydrophobic environment of the 3HM alkyl core.

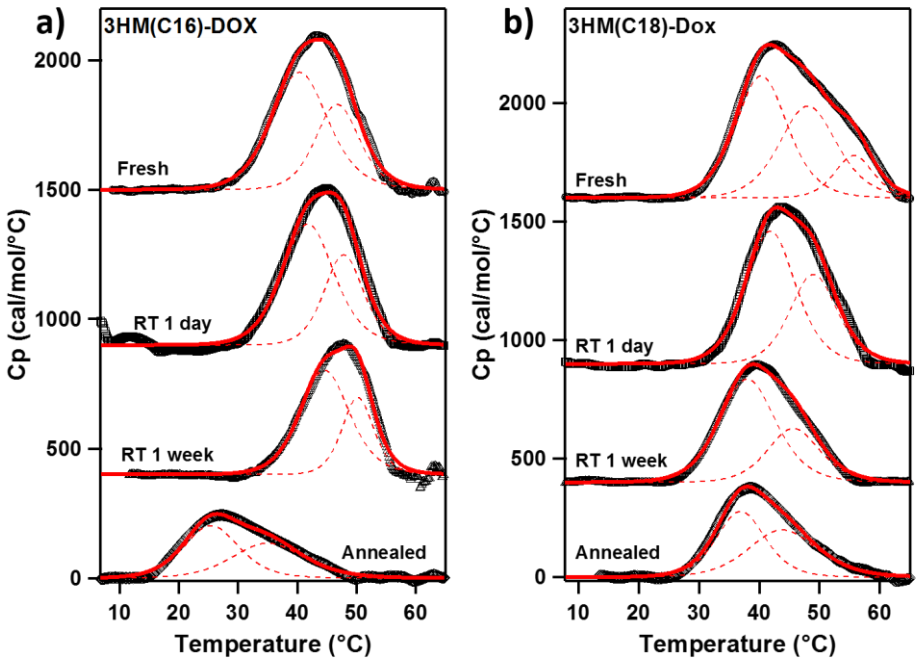

Figure 5.6. DSC measurements of (a) 3HM(C16)-DOX and (b) 3HM(C18)-DOX.

Table 5.3. Transition temperatures and total enthalpy of 3HM(C16)-DOX and 3HM(C18)-DOX formulations corresponding to data in Figure 6.

	3HM(C16)-DOX		3HM(C18)-DOX	
	T_m (°C)	ΔH (kJ/mol)	T_m (°C)	ΔH (kJ/mol)
Fresh	40, 47	37.7 ± 0.2	40, 48, 56	51.6 ± 6.8
RT 1 day	42, 48	35.8 ± 3.5	42, 49	42.4 ± 1.9
RT 1 week	45, 50	27.6 ± 2.4	38, 46	33.7 ± 1.5
Annealed	26, 35	19.6 ± 1.0	37, 44	25.3 ± 0.2

The time-dependent behavior of alkyl packing, size distribution, and kinetic stability of 3HM provided insight into the hierarchical molecular assembly of 3HM. We found that the phase transition of alkyl packing in the hydrophobic core of 3HM evolved as a function of time due to rearrangement of the amphiphiles within the micelle and the kinetic pathway was dependent on alkyl chain length. The time evolution of phase transitions was accompanied by an improvement in the kinetic stability of 3HM along with a gradual decrease in the size of 3HM. Encapsulation of DOX in 3HM was found to increase the T_m by ~10°C for both C16 and C18 micelles, albeit accompanied by a ~30% decrease in the enthalpy. Distinct thermal phase transitions were formed upon coassembly of DOX with 3HM. The time-dependent behavior of 3HM at room temperature over a period of days or weeks approaches that of an annealed 3HM sample at equilibrium. This is indicative of a slow reorganization of 3HM on the molecular level of the amphiphilic subunits through inter-micellar exchange as well as intra-micellar rearrangement. Thermal annealing can be used to overcome the energetic barriers and expedite the formation of monodisperse and stable 3HM. This study revealed important insights into the molecular contributions to the kinetic processes during the assembly process of a multicomponent peptide-PEG-lipid hybrid conjugate system toward its equilibrium state.

Some macromolecular assemblies are known to be kinetically trapped on timescales of days to weeks[43-46]. The unique hierarchical structure of 3HM provides enhanced kinetic stability compared to simple n-alkyl-poly(ethylene oxide) micelles. Micelle formed by poly(ethylene oxide) end-capped on both sides with C16 alkyl chains has an E_a ~73 kJ/mol[47]. For n-alkyl-poly(ethylene oxide) micelle with a similar subunit desorption E_a to 3HM, alkyl chain length of between 24 and 27 is required[48], significantly increasing the hydrophobicity of the system. Moreover, in the n-alkyl-poly(ethylene oxide) system, the activation energy was found to be independent on the length of the soluble PEO block[49]. From the dimensions of the PEG chain in 3HM[29], based on small-angle neutron scattering contrast variation measurements and coarse-grained molecular dynamics simulation, we calculated the entropic stabilization energy to be ~20 kJ/mol. The unique headgroup structure of amphiphilic peptide-PEG-lipid conjugates in 3HM provides enhanced kinetic micelle stability compared to traditional polymeric micelles. The high activation barrier required for subunits to desorb from 3HM indicates that the micelles are stable even under sink conditions such as that experienced by micelles administered through intravenous routes. C16- and C18-micelles displayed different circulation lifetimes *in vivo*[27], we show here that the different kinetic pathways could be used to further tune their respective stabilities for future biotechnological applications.

§ 5.3 Conclusion

The formation of 3HM is strongly driven by the hydrophobic interaction of the alkyl chains between subunits. Time-dependent rearrangement of amphiphiles during the micelles assembly process was governed by the association of helices into 3-helix bundles in the corona as supported by the changes in transition temperatures as shown by DSC. Intermicellar subunit exchange as well as intramicellar subunit reorganization are important

mechanisms, equilibrating 3HM into highly stable, monodisperse ~15 nm micelles. Decoupling the contributions of individual components in the kinetic formation of 3HM and how encapsulated cargo affects this formation will allow us to design micellar nanocarrier systems with enhanced control over the kinetic stability for predictable and tunable drug delivery applications.

§ 5.4 Experimental methods

5.4.1. Synthesis of amphiphilic peptide-polymer conjugate and fluorescein-labeled peptide-polymer conjugate

Synthesis of amphiphilic peptide-polymer conjugates has been previously described in detail[25]. The trimeric coiled-coil peptide 1CW (EVEALEKKVAALECKVQALEKKVEALEHGW) was modified at the N-terminus with a short C6 alkyl linker, Fmoc-6-aminohexanoic acid, followed by a lysine residue. This allowed for conjugation of two saturated carboxylic acid molecules, either hexadecanoic acid (C16) or octadecanoic acid (C18), to the N-terminus, generating a branched alkyl tail. The cysteine residue at position 14 facilitates conjugation of a maleimide-PEG chain (MW 2000) to the exterior of the coiled-coil bundle. Fluorescein (FAM) was attached to the C-terminus of the C16 conjugate by selective deprotection of alloc-protected lysine followed by coupling of 5(6)-carboxy-fluorescein. Specifically, 0.2 eq. of $Pd(PPh_3)_4$ was used as a catalyst with 24 eq. of phenylsilane as an allyl acceptor in dichloromethane. The reaction was carried out for 30 mins each, repeated 5 times.

The conjugates were purified by RP-HPLC (Beckman Coulter) using a C-4 column (Vydac, Phenomenex). Purification of the C16 conjugate was facilitated by a linear AB gradient where solvent A is water plus 0.1% (v/v) TFA and solvent B is acetonitrile plus 0.1% (v/v) TFA. The purified C16 conjugates eluted at ~85% B. The C18 and C16-FAM conjugates were purified using isopropanol plus 0.1% (v/v) TFA as solvent B and the desired conjugates eluted ~90% B. The masses of the purified conjugates were verified by MALDI-TOF (Appendix A.4.1).

5.4.2 Sample preparation

Lyophilized powder of 3HM was dissolved in phosphate buffer (25 mM, pH 7.4) to yield ‘fresh’ 3HM. Room temperature (~20°C) samples were allowed to equilibrate for 1 day and 1 week (‘RT 1 day’ and ‘RT 1 week’ respectively). ‘Annealed’ samples were heated in a water bath at 70°C for 45 mins and allowed to cool down to room temperature for 30 mins before measurements.

5.4.3 Differential Scanning Calorimetry (DSC)

DSC measurements were conducted using a VP-Microcal calorimeter (GE). ~550 uL of sample and buffer solutions were loaded into two hermetically sealed tantalum alloy cells at a pressure of ~28 psi to prevent water evaporation during the heating cycle. The temperature was increased from 5°C to 65°C at a scanrate of 1°C/min with 15-minute

equilibration at 5°C. Baseline correction, concentration normalization, data fitting and deconvolution were performed using the Origin software provided by Microcal.

5.4.4 Circular Dichroism (CD)

Circular dichroism measurements for secondary and tertiary structure characterization were conducted on a J-815 spectrometer (Jasco) using a quartz cell with 0.1 cm pathlength. All samples were prepared at a concentration ~100 μM in phosphate buffer (25 mM, pH 7.4). The temperature was increased from 5°C to 110°C at a rate of 1°C/min and samples were allowed to equilibrate for 1 minute before each measurement at 5°C intervals. CD spectra were recorded from 250 nm to 190 nm at 0.2 nm intervals with a scanrate of 100 nm/min and a response time of 4 s. The measured ellipticity was normalized by concentration and converted to molar residual ellipticity. The mean residue ellipticity for a 100% helix peptide of infinite length[50-52] was taken to be -37400 deg cm^2 dmol^{-1}.

5.4.5 Dynamic Light Scattering (DLS)

Size distributions of 3HM were measured using a BI-200SM light scattering system (Brookhaven Instruments). Laser light (637 nm, 30 mW) was scattered from aqueous dispersions of 3HM (~100 μM) at a 90° scattering geometry with a 100 μm filter. The temperature of the sample cell was maintained at 25°C using a water bath. The autocorrelation function of the scattered light was collected for 1 minute and analyzed to determine the size distribution.

5.4.6 Small-Angle X-ray Scattering (SAXS)

Small-angle X-ray scattering (SAXS) experiments were carried out at the Advanced Light Source (ALS) at the Lawrence Berkeley National Lab, Berkeley, California at the SAXS/WAXS/GISAXS beamline 7.3.3. The instrument was operated using an X-ray energy of 10 keV and a sample-detector length of 1.9 m and a 1 M Pilatus detector. Samples were contained in standard boron–quartz capillaries situated in a custom-made sample holder. Using this setup, background subtraction could be performed quantitatively. Samples were prepared in phosphate buffer (25 mM, pH 7.4) at a concentration of ~5 mg/ml.

5.4.7 Fluorescence recovery

Fluorescence spectroscopy was measured using a LS-55 fluorescence spectrometer (Perkin Elmer). Briefly, 50 μM of fluorescein-labeled 3HM (3HM-FAM, donor) was prepared ‘fresh’, ‘RT 1 day’, and ‘annealed’ as described in the previous section. 400 μM of unlabeled 3HM (acceptor) was annealed at 70°C then allowed to gently cool to room temperature for 30 mins before mixing with the donor solution for fluorescence recovery experiments. The two solutions were mixed in a 1:5 volume ratio to give a final donor:acceptor molar ratio of 1:40. The sample was loaded into a 1 cm pathlength quartz cell (Starna Cells). Temporal evolution of fluorescence intensity was recorded every 30 seconds at 522 nm using an excitation wavelength of 490 nm at a scan rate of 200 nm/min. Temperature control of the sample cell was achieved using a Peltier temperature controller

(PTP-1, Perkin Elmer). Fluorescence recovery experiments were conducted with the sample cell maintained at 20°C for 4 hours.

5.4.8 Doxorubicin encapsulation

Loading of DOX in 3HM was performed using the thin film hydration method as previously described[26, 27]. Briefly, doxorubicin hydrochloride (Sigma-Aldrich) was dissolved in methanol at a concentration of 2 mg/ml and 3HM was added to achieve a concentration of 10 mg/ml. The methanol was evaporated under vacuum at 60°C for 3 hours to yield a thin film. Phosphate buffer (pH 7.4, 25 mM) was added to rehydrate the film to obtain a 1 mg/ml solution for further DSC, DLS, and CD characterization.

Chapter 6

Self-Assembled 'Patchy' Micelles with Controlled Multivalency Based on Coiled-coil Peptide-PEG-Lipid Conjugates

Coiled-coil peptide-polymer-lipid conjugates are an emerging class of hybrid biomaterials. Here, we present a mixture of two amphiphilic 3-helix and 4-helix peptide-PEG-lipid hybrid conjugates that hierarchically self-assemble into patchy mixed micelles. The local multivalent ligand cluster size on the micelle surface can be controlled based on the coiled-coil oligomeric state. The oligomeric states of mixed peptide bundles were found to be in their individual native states. Similarly, mixed micelles indicate the orthogonal self-association of coiled-coil amphiphiles. Using differential scanning calorimetry and fluorescence recovery, the mixed micelle showed nanodomains enriched in either 3-helix or 4-helix coiled-coil bundles. This report provides important insights into the assembly and formation of patchy micelles with control over the local multivalent state of ligands on the micelle surface.

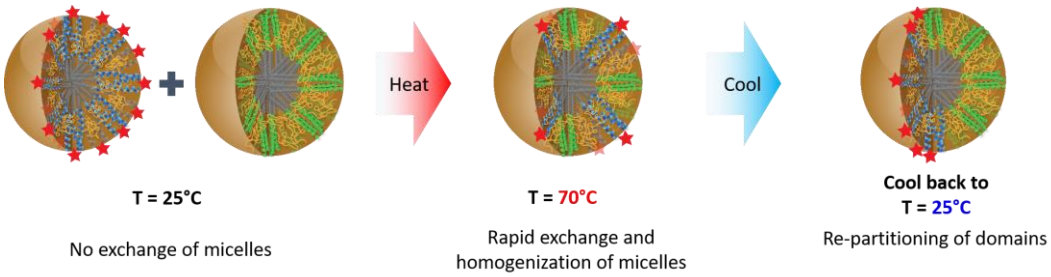

§ 6.1 Introduction

Nanocarriers exploit characteristics of tumor growth, such as leaky vasculature and poor lymphatic drainage, for the use of passive targeting via the enhanced permeation and retention (EPR) effect[1, 2]. In addition to the EPR effect, nanocarriers can also be actively targeted to upregulated cellular receptors or components that are present on tumor cells by incorporating surface grafted recognition moieties, such as sugar moieties[3], epidermal growth factor[4], folate[5, 6], antibodies[7] and peptides[8, 9], to improve the efficacy of treatment and minimize side effects. Active targeting is of particular importance since many drug carriers encounter difficulties in accessing cancer cells deep in the tumor tissues and to interact with target cells after accumulation[10]. A wide variety of nanocarriers can be readily prepared, including liposomes[11-13], dendrimers[14, 15], micelles[16, 17], and virus-like particles[18, 19] and targeting ligands can be conjugated to the nanocarrier surface[20]. Multivalent ligands can be a viable route to improve the targeting efficiency of nanocarriers; biological multivalent inhibitors can increase binding avidity by 10–10^9 fold[21-24]. Experimentally, a 30 nm nanoparticle with four RGD peptides showed 25-fold enhancement in endothelial cell binding[25]. Three folate groups led to 2,500-fold enhancement in dendrimers binding to a surface[26]. However, in contrast to well-regulated structural control seen in viruses[21], there is limited structural control in existing nanocarriers over the spatial distribution of ligands and the orientation of ligand relative to the particle surface that determines the availability of ligand binding sites. To this end, we have developed a new class of 3-helix micelle (3HM) nanocarrier based on amphiphilic coiled-coil peptide-polymer-lipid conjugates[27-33] that has the potential to exert control over the local multivalency of presented ligand clusters.

3HM has many desirable attributes as an effective drug delivery nanocarrier such as long circulation, deep tumor penetration, minimal cargo leakage in serum, and renal clearance[28-30, 32]. 3HM is based on a common protein tertiary structure, i.e. coiled-coil, that is routinely used to present ligand clusters on cell surfaces[34-36]. Coiled-coil self-assembly has high fidelity and orthogonal coiled-coil sequences[37] have been conjugated and used to assemble higher ordered nanostructures such as protein-like nanoparticles[38] and nanocages[39, 40]. Mixed micelles generated from two or more building blocks have been used to tune stability and drug loading capacity of conventional polymeric micelles for drug delivery[41]. This approach also allows for the incorporation of multiple functionalities, including ligand targeting, into the system. One can envision the use of mixed micelles based on coiled-coil peptides would allow the generation of ligand clusters with well-defined local multivalency determined by the oligomeric state of the coiled-coils within the mixed micelle. This approach also opens new possibilities to generate multicompartment micelles with the two coiled-coil building blocks possessing different functionalities.

The generation of micron-sized inorganic multicompartment, Janus, or patchy particles has been well studied and optimized, whereas development of sub-100 nm patchy particles have been more challenging[42]. patchy particles have been generated from linear dendritic polymers[43, 44], di- and tri-block copolymers[45-51], polymersomes[52], and other systems that exploit surface roughness[53], layer-by-layer deposition[54], self-assembled monolayers[55-57], host-guest binding[58], metal coordination[59], polymer grafting[60] to produce the patches. However, none of these approaches allow control over the precise ligand cluster size, or local multivalency, on the surface of the nanoparticles. Ligand clustering with controlled cluster size observed in viruses is vital to improve binding selectivity and accuracy, and yet, has not been systematically investigated due to the lack of a platform that can regulate the clustering of ligands.

In this contribution, we present a micellar platform that utilizes hierarchical self-assembly of amphiphilic coiled-coil peptide-PEG-lipid hybrid conjugates to control the local multivalency of ligands on the micelle surface based on the coiled-coil oligomeric state. A mixture of 3-helix and 4-helix peptide bundles were shown to retain their individual native oligomeric states. Mixed micelles with excellent stability in the presence of bovine serum albumin can be generated from mixtures of 3-helix and 4-helix amphiphilic peptide-PEG-lipid conjugates at various ratios. Mixed micelles at various mixing ratios showed similar stability compared to the individual micelles. At a 1:1 mixing ratio of 3HM:4HM, the thermal transition associated with alkyl chain packing within the hydrophobic core of the mixed micelle was found to re-distribute from a single homogeneous transition for an annealed sample to two distinct transitions indicating the formation of distinct domains as it was cooled down to room temperature. Fluorescence self-quenching and recovery experiments further affirmed the formation of nanodomains within the mixed micelles. This study provides valuable insight into the self-assembly of orthogonal coiled-coil peptide-PEG-lipid conjugate amphiphiles into patchy micelles and guidance to develop biomaterials with controlled local multivalency for ligand cluster presentation.

§ 6.2 Results and discussion

6.2.1 Oligomeric state of mixed coiled-coil peptides

A mixture of 3-helix and 4-helix peptides showed retention of their individual oligomeric states as shown in Figure 6.1.

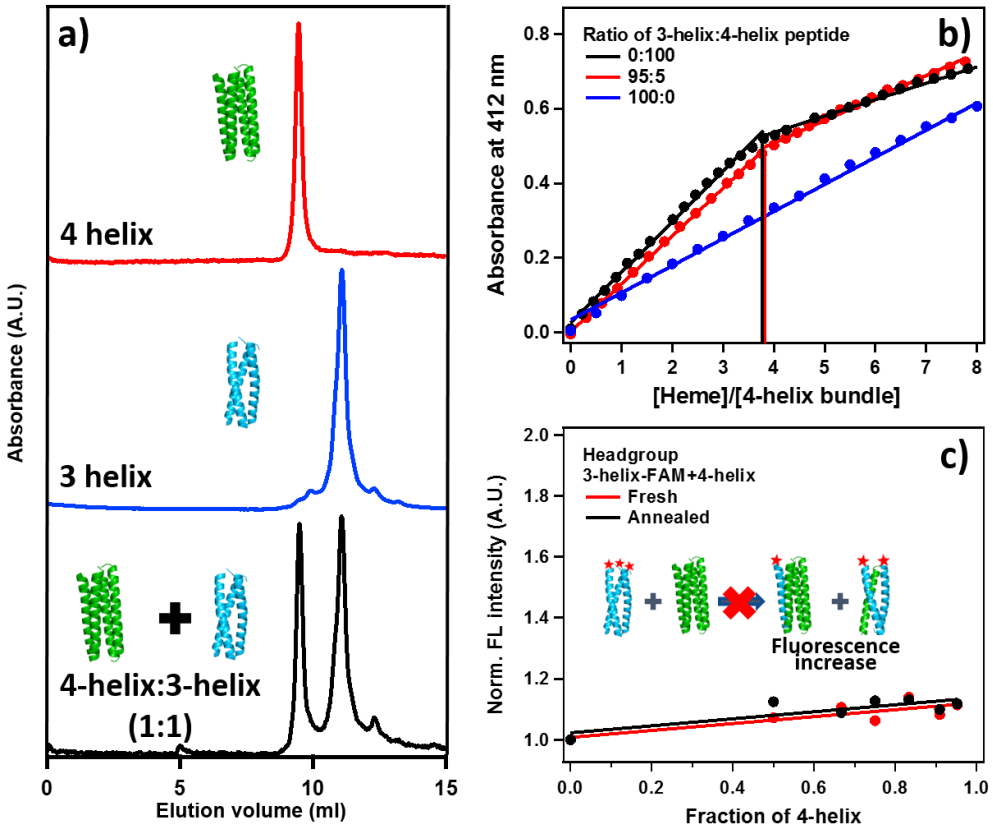

Figure 6.1. Mixtures of 3-helix and 4-helix peptides. (a) SEC traces of 4-helix peptide (blue), 3-helix peptide (red), and a 1:1 mixture of 3-helix and 4-helix peptides (black). (b) UV titration of heme bound to 4-helix peptide bundles in the absence of 4-helix peptide (purple), 5% 4-helix peptide (red), and 100% 4-helix peptide (black). (c) Fluorescence recovery of various ratios of 3-helix to 4-helix mixtures. Freshly prepared mixtures and annealed samples show no significant difference in fluorescence intensity.

Figure 6.1a shows that the SEC trace of a 1:1 mixture of 3-helix:4-helix peptide (black) can be deconvoluted into two distinct peaks corresponding to the individual 3-helix and 4-helix peptides (blue and red, respectively). This is the first indication that mixture of the peptides does not result in cross-oligomerization since they retain their original bundle sizes. Next, Figure 6.1b shows the absorption at 412 nm due to binding of heme to the bis-

histidyl ligation pockets of the 4-helix peptide[61-63]. The ratio at which the slope of the data changes corresponds to the number of heme molecules bound to each 4-helix bundle. 4-helix peptide in presence of 5% 3-helix peptide (red) indicates ~3.8 hemes bound per 4-helix bundle, close to the native state (in the absence of 3-helix peptides, shown in black) binding capacity of 4 heme molecules per 4-helix bundle. Retention of the heme binding pocket of the 4-helix peptide suggests minimal perturbation of the 4-helix bundle oligomeric state in the presence of 3-helix peptides. Absence of an inflection point when there is no 4-helix peptide available for heme to bind is shown in blue. Figure 6.1c shows the fluorescence intensity change as a function of unlabeled 4-helix peptide mixed with FAM-labeled 3-helix peptide. Minimal increase in the fluorescence intensity of FAM-labeled 3-helix peptide when mixed with 4-helix peptide at various mixing fractions (red trace) indicates that there is a lack of cross-oligomerization between the two coiled-coil peptides. Furthermore, the similar behavior of the mixtures even in the presence of thermal annealing (black trace) does not promote cross-oligomerization. This further suggests that the self-assembly of the two peptides are orthogonal and there is an absence of cross-oligomerization when the two peptides are mixed.

6.2.2 Mixed coiled-coil micelles – oligomeric state and stability

We seek to understand the oligomeric state of the coiled-coil bundles upon conjugation of alkyl tails and self-assembled into micelles. 3-helix peptide-polymer-lipid conjugate amphiphiles have previously been observed to retain its native trimeric state at the air-water interface[64]. Since amphiphiles of both 3-helix and 4-helix peptides form micelles of similar sizes in aqueous solution (Appendix A.5.2), SEC is not a viable method to study the individual oligomeric states of the peptides within mixed micelles. However, cofactor binding of heme to the coiled-coil bundle headgroup of 4-helix amphiphiles, as elucidated for the peptide mixtures in Figure 6.1b, allows us to probe the oligomeric state when mixed micelles are formed in the presence of 3-helix amphiphiles. Figure 6.2a shows the UV-vis heme titration into an aqueous solution of ~8 μM 4HM. Incorporation of heme into the hydrophobic pocket of the 4-helix peptide is evident from the increase in the Soret peak at 412 nm and the poorly resolved Q_α and Q_β bands at 560 and 529 nm, respectively[61, 65, 66]. As more heme is added, the absorption maxima experienced a blue shift, due to the absorbance of free heme in solution. Figure 6.2b plots the absorbance at 412 nm as a function of heme per 4-helix amphiphile. In the absence of 3HM, the tertiary structure of 4-helix bundle within 4HM (black) retained native-like heme binding capability[61], indicating that there is no substantial deleterious effects of di-alkyl conjugation to the N-terminus and PEGylation of the coiled-coil exterior. More importantly, in the presence of excess 3-helix amphiphiles (red), the number of heme molecules bound to the 4-helix amphiphiles was not compromised indicating that the tertiary structure is likely to be preserved. Once again, no change in slope was observed for a solution of 3HM in the absence of 4HM for heme binding (blue). The orthogonality and peptide native oligomeric states were preserved when the peptides were conjugated with two hexadecanoic acid tails at the peptide N-terminus and the resulting amphiphiles mixed.

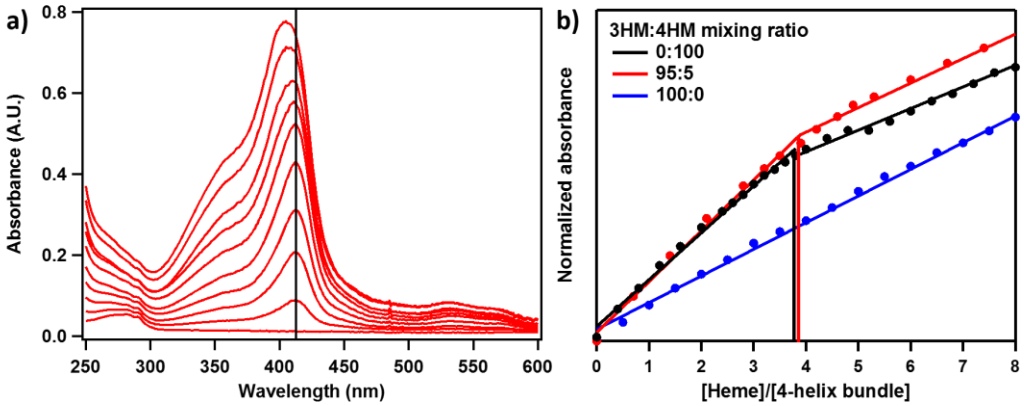

Figure 6.2. (a) UV-vis spectra of heme titrated into a ~8 μM solution of 4HM upon addition of 0, 0.4, 1.2, 2, 3, 4, 4.8, 6, 7.2, and 8 eq. of heme per 4-helix bundle. The vertical black line indicates the peak at 412 nm which corresponds to the absorbance of heme within the hydrophobic interior of the 4-helix bundle. (b) Absorbance at 412 nm monitored as a function of heme molecules per 4-helix bundle ratio for pure 4HM (black), pure 3HM (blue), and at 4HM:3HM ratio of 5:95 (red). The ratio at which the slope changes indicates the number of heme molecules bound to each 4-helix bundle.

To assess if mixed micelles were created and quantify their stability[67-69], we measured the change in emission of an encapsulated FRET pair in the presence of bovine serum albumin (BSA) at various 3HM:4HM ratios. When both FRET molecules were encapsulated within the same micelle, appropriate excitation of the donor molecule can lead to energy transfer to the acceptor molecule due to the close proximity between the two molecules. As a result, excitation at 450 nm (donor excitation) leads to a strong emission at 565 nm (acceptor emission). If the mixed micelles dissemble, the encapsulated FRET molecules are released and diffused apart, eliminating the energy transfer. As such, a shift from 565 to 505 nm would be observed. Figure 6.3a shows the change in normalized FRET ratio over a 24-hour period. All micelles created from various 3HM:4HM ratios displayed good stability over the time period studied with FRET ratios above 0.9. Two formulations in particular, 3HM:4HM ratios of 50:50 and 0:100, displayed higher stability than the remaining of the micellar ratios with FRET ratios maintained ~ 0.99 over 24 hrs. The good stability presumably stems from the unique architecture of the coiled-coil peptide-polymer headgroup that can direct polymer entropic repulsion between subunits of the micelle[27]. To further illustrate the high kinetic stability of 3HM and 4HM, the FRET pair, DiO and DiI, was independently encapsulated within each of 3HM and 4HM and mixed in equal molar ratios at room temperature as shown in Figure 6.3b. The emission spectra over 16 hrs essentially remained constant, indicating no cargo leakage and slow subunit kinetic exchange of the two micellar populations. The high kinetic stability of micellar formulations at various 3HM:4HM ratios indicates that they do not undergo significant disassembly in the presence of serum albumin. The stability of the mixed micelles demonstrated in the presence of BSA suggests that these mixed micelles may be compatible *in vivo*, which is critical for intravenous drug delivery applications.

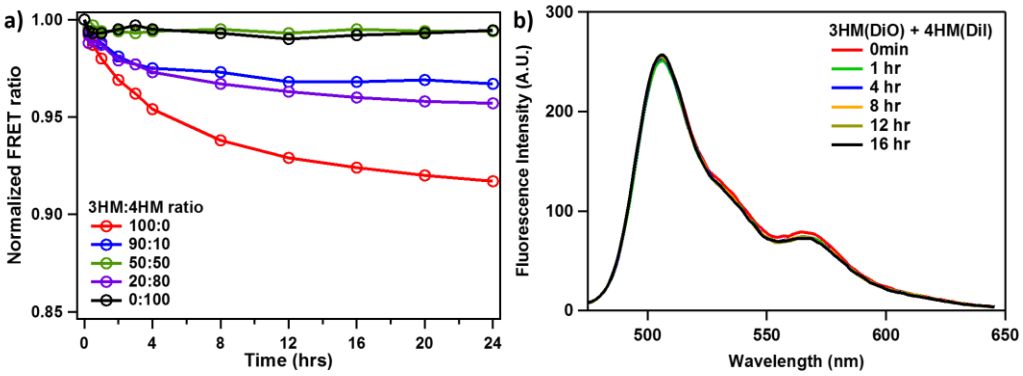

Figure 6.3. (a) Plot of normalized FRET ratio as a function of time for mixed micelles at various ratios of 3HM:4HM. (b) Time-resolved fluorescence showing a 1:1 mixture of 3HM and 4HM, each independently encapsulated with DiO and DiI, respectively.

6.2.3 Phase separation of coiled-coil domains within mixed micelle

Since the 50:50 ratio of 3HM:4HM showed higher stability than mixed micelles composed of other ratios, we decided to further investigate the mixed micelle at this 50:50 ratio. To probe the distribution of the two coiled-coil amphiphiles within the mixed micelle, we first studied micelles composing of the individual components – pristine 3HM and pristine 4HM. Figure 6.4a shows DSC measurements of the individual pristine micelles having very distinct phase transition temperatures at 17°C and 40°C for 3HM and 4HM, respectively. Two separate micelle solutions of 3HM and 4HM mixed in a 1:1 ratio displayed two prominent transitions at 17°C and 40°C, indicative of discrete 3HM and 4HM populations in solution. However, a single homogeneous transition ~21°C is apparent in Figure 6.4b upon thermal annealing of this mixture and subjected to immediate DSC measurement (t = 0 hr). As the 1:1 mixture was allowed to equilibrate at room temperature after thermal treatment, a separate transition at a higher temperature of ~33°C appears and the enthalpy associated with the 33°C transition continued to increase from 1 hr to 16 hr while the transition at 20°C decreased in enthalpy over the same time period. This suggests that returning the thermally treated mixed micelles that are phase-mixed back to ambient temperature led to the formation of distinct 3-helix and 4-helix domains within the mixed micelles over the span of several to tens of hours.

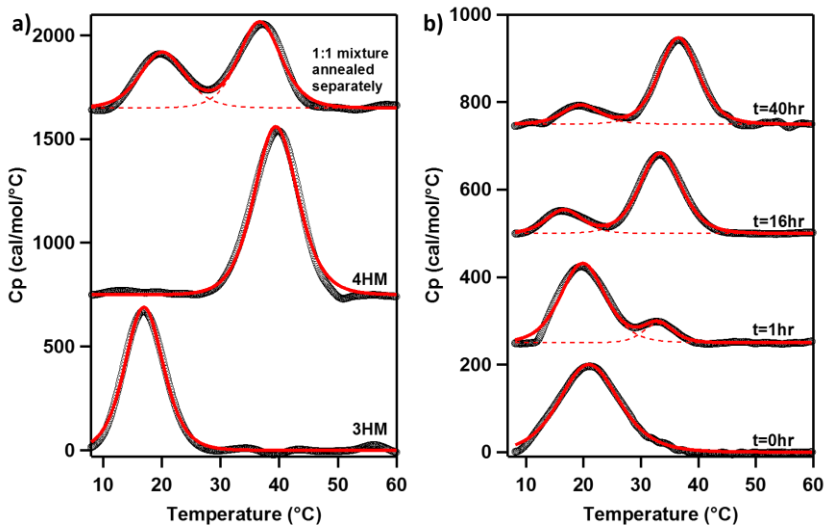

Figure 6.4. DSC measurements of (a) pristine 3HM, 4HM, and 1:1 mixture of separately prepared 3HM and 4HM, (b) time evolution of 1:1 ratio of 3HM:4HM mixed micelle at times 0, 1, 16, 26, and 40 hrs after thermal annealing. Solid red lines are fits to the data while dotted red lines indicate the deconvoluted peaks.

Table 6.1. Phase transition temperatures and enthalpy for the data shown in Figure 6.4.

Sample	**T_m (°C)**	**ΔH (kJ/mol)**	**Total ΔH (kJ/mol)**
3HM	17	25.1 ± 0.1	25.1 ± 0.1
4HM	40	33.5 ± 0.2	33.5 ± 0.2
1:1 t = 0hr	21	11.5 ± 0.04	11.5 ± 0.04
1:1 t = 1hr	20	7.84 ± 0.06	9.12 ± 0.11
	33	1.28 ± 0.05	
1:1 t = 16hr	17	1.85 ± 0.02	9.20 ± 0.04
	33	7.35 ± 0.02	
1:1 t = 40hr	20	1.56 ± 0.02	9.11 ± 0.06
	37	7.60 ± 0.02	

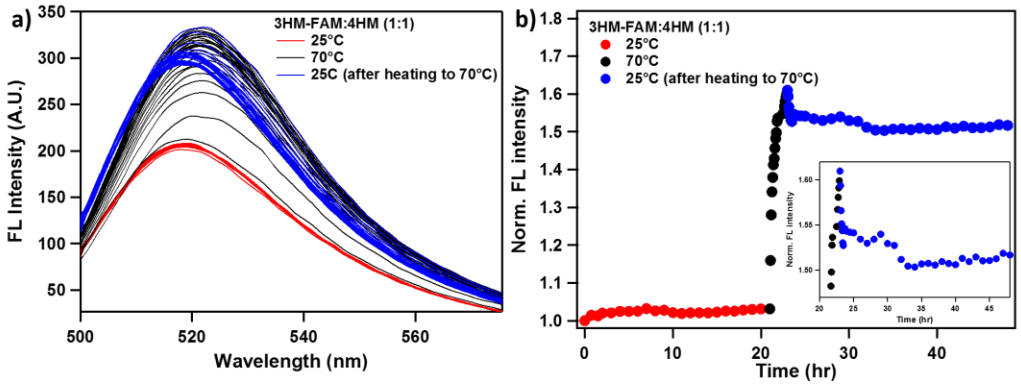

Figure 6.5. (a) Fluorescence spectra of 3HM-FAM mixed with 4HM at a 1:1 ratio as a function of temperature. (b) Normalized fluorescence intensity at 520 nm plotted as a function of incubation time at the different temperatures. Data points for 25°C, 70°C, and cooled down to 25°C in red, black, and blue, respectively.

To further examine the phase separation behavior of nanodomains within the 1:1 ratio of 3-helix and 4-helix mixed micelles, we studied the formation process of mixed micelles from 3HM and 4HM using fluorescence self-quenching and recovery. Figure 6.4a shows the fluorescence spectra of unlabeled 4HM added to a solution of FAM-labeled 3HM in a 1:1 mixture as a function of time at three temperatures – 25°C (red), heated to 70°C (black), then cooled down to 25°C (blue). Figure 6.4b plots the normalized fluorescence intensity as a function of time and the data at the three temperatures are in the same color scheme as Figure 6.4a. The mixture of two separate micellar populations of 3HM and 4HM at the initial temperature of 25°C experienced a slight ~3% increase in fluorescence intensity over a period of 22 hrs. This modest increase in fluorescence is due to the excellent kinetic stability of 3HM and 4HM with minimal subunit exchange between the two micelle populations[31]. However, when the temperature of the mixture was raised to 70°C, the fluorescence intensity greatly increased by 58% in 2 hrs. This large increase in fluorescence intensity is due to subunit exchange as the FAM-labeled 3-helix amphiphiles are desorbed from the self-quenched 3HM-FAM and inserted into non-labeled 4HM. As the sample cell was cooled back down to 25°C, the fluorescence intensity decreased 10% over ~10 hrs. The FAM-labeled 3-helix amphiphiles reorganize themselves closer to each other, thereby self-quenching the fluorescence and resulting in a decrease in fluorescence intensity. This sequence of results show that 3HM and 4HM are kinetically stable at room temperature and minimal subunit exchange occurs in the presence of the other micellar species. Addition of thermal energy promotes the rapid exchange of amphiphiles between 3HM and 4HM, blending to form mixed micelles. However, cooling down to ambient temperature resulted in spatial rearrangement of the 3-helix and 4-helix amphiphiles within the mixed micelles to form 3-helix rich and 4-helix rich nanodomains within the same micelle.

The results shown here strongly suggest that the lack of cross-oligomerization between two orthogonal 3-helix and 4-helix coiled-coil bundles, even when modified with di-alkyl chains and PEG, indicates the oligomeric state of coiled-coils can be an effective

platform to specify the local multivalency of ligand clusters. Here, we show that highly stable sub-20 nm mixed micelles can be generated from a pair of orthogonal coiled-coil peptide-PEG-lipid conjugates. Furthermore, the 3-helix and 4-helix amphiphiles were observed to phase segregate within the mixed micelles, forming 'patches' of 3-helix and 4-helix rich domains. Further work is needed to quantify the spatial distribution and domain size of 3-helix and 4-helix regions within the mixed micelles. The phase separation is likely driven by incompatible geometric packing of the coiled-coil headgroups in the micelle corona and alkyl tails in the hydrophobic core. 4-helix amphiphiles have a higher density of alkyl chains attached to each bundle compared to 3-helix amphiphiles. Although the length of the 4-helix bundle is longer than 3HM[70], 4HM forms micelles that are smaller than 3HM, suggesting that the alkyl chains in 4HM extend significantly less than those in 3HM. The mismatch in alkyl chain length could cause phase separation in mixed micelles. The domain size of nanodomains of lipids, also known as lipid rafts, in membranes is directly correlated to the mismatch in degree of alkyl unsaturation and subsequently bilayer thickness[71, 72]. We hypothesize a similar effect of interfacial energy minimization between 3-helix and 4-helix amphiphiles that dominates the phase separation phenomenon described here. This study is a first important step to elucidate the properties of these new hybrid self-assembled mixed micellar structures, and to allow their optimization regarding different fields of application, in particular the design of drug delivery nanosystems with targeting capability using clustered ligands with well-defined oligomeric states using either the 3-helix or 4-helix domain.

§ 6.3 Conclusion

In this report, we show the retention of coiled-coil bundle oligomeric states and the orthogonality of 3-helix and 4-helix peptide-PEG-lipid amphiphiles in mixed micelles with potential utility for control over the local multivalency of ligands. Additionally, the mixed micelles displayed high stability in serum albumin which is crucial for intravenous drug delivery applications. Temporal evolution of alkyl packing and tracking the relative distribution of FAM-tagged 3-helix amphiphiles within mixed micelles indicated partitioning of 3-helix and 4-helix rich domains to form self-assembled sub-20 nm patchy micellar particles. The proposed approach described here for generating mixed micelles with well-defined ligand cluster sizes is extremely versatile due to the ability to engineer a variety of coiled-coils with different oligomeric states. Coiled-coil based peptide-PEG-lipid conjugates are a promising class of materials to specify the oligomeric state of ligands on surfaces for a wide range of diagnostic and therapeutic applications.

§ 6.4 Experimental methods

6.4.1 Synthesis of and purification of peptide-PEG-lipid conjugates

Synthesis of amphiphilic peptide-polymer conjugates using solid-phase peptide synthesis based on standard Fmoc-chemistry have been previously described in detail[27, 30, 31] and will only be outlined here. The two peptides studied here are based on a 3-helix coiled-coil peptide sequence[73] (EVEALEKKVAALECKVQALEKKVEALEHGW) and a 4-helix

coiled-coil peptide[74] (GGGEIWKLHEEFLCKFEELLKLHEERLKKL). PAL-PEG-PS resin (0.17 mmol/g loading, ThermoFisher Scientific) was used to conduct solid-phase synthesis of the peptides on a Prelude peptide synthesizer (Protein Technologies). The N-termini of the peptides are modified with a short C6 alkyl linker, Fmoc-6-aminohexanoic acid, followed by a lysine residue. This allowed for conjugation of two palmitic acid molecules to the N-terminus. Both peptides contain a cysteine residue at position 14 to facilitate conjugation of a maleimide-PEG chain (MW 2000) to the exterior of the coiled-coil bundles. Fluorescein was attached to the C-terminus of the 3-helix peptide by selective deprotection of alloc-protected lysine followed by coupling the amine with 5(6)-carboxy-fluorescein. Specifically, 0.2 eq. of $Pd(PPh_3)_4$ was used as a catalyst with 24 eq. of phenylsilane as an allyl trapper in dichloromethane. The reaction was carried out for 30 mins each, repeated 5 times.

The conjugates were purified by RP-HPLC (Beckman Coulter) using a C-4 column (Vydac, Phenomenex). Separation of the conjugates was facilitated by using a linear AB gradient where solvent A is water plus 0.1% (v/v) TFA and solvent B is acetonitrile plus 0.1% (v/v) TFA. Elution of the conjugate was ~85% B. Purification of the FAM-labeled conjugate was achieved using solvent B as isopropanol plus 0.1% (v/v) TFA and the purified product eluted ~90% B. The masses of the purified conjugates were verified by MALDI-TOF (Appendix A.5.1).

6.4.2 Size-exclusion chromatography (SEC)

The sizes of 3-helix peptide, 4-helix peptide, and a 1:1 mixture of the two peptides were studied using SEC on a BioSep-SEC-S4000 column (Phenomenex) at a concentration of ~100 μM. Elution was carried out using a flowrate of 1 mL/min with phosphate buffer (pH 7.4, 25 mM) for 15 minutes. The elution profiles were monitored with a UV-Vis detector at wavelengths of 220 nm and 280 nm.

6.4.3 UV-vis heme titration

Titration experiments were performed with 1 mL of ~8 μM solutions of 4-helix peptide or 4HM dissolved in phosphate buffer (25 mM, pH 7.4) in the presence of excess 3-helix peptide or 3HM, respectively. Spectra from 250–600 nm were recorded on a Hewlett-Packard 8453 spectrophotometer using a 1 cm pathlength quartz cuvette after addition of each 2 μL aliquot of a ~800 μM stock hemin solution in DMSO.

6.4.4 Fluorescence self-quenching and recovery

Fluorescence spectroscopy was measured using a LS-55 fluorescence spectrometer (Perkin Elmer). Briefly, 200 μM of fluorescein-labeled 3HM (donor) and 400 μM of unlabeled 4HM (acceptor) were independently annealed at 70 °C then allowed to cool to room temperature before mixing for self-quenching experiments. The two solutions were then mixed in a 1:2 (donor:acceptor) volume ratio at a total volume of 400 μL, giving a donor:acceptor molar ratio of 1:1. The sample was loaded into a 1 mm by 10 mm quartz cell (Starna Cells). Temporal evolution of fluorescence intensity at 520 nm was recorded every 30 seconds using an excitation wavelength of 450 nm. Self-quenching and recovery

experiments were conducted with the sample cell maintained at 25°C for 22 hrs, increased to 70°C for 2 hrs, and finally decreased to 25°C for a further 20 hrs.

6.4.5 Forster Resonance Energy Transfer (FRET)

A pair of lipophilic FRET pair, 3,3′-dioctadecyloxacarbocyanine perchlorate (DiO, donor) and 1,1′-dioctadecyl-3,3,3′,3′-tetramethylindocarbocyanine perchlorate (DiI, acceptor), was dissolved in methanol (1 wt%) along with various 3HM:4HM ratios. The methanol was evaporated under vacuum at 60°C for 3 hrs to form a thin film in a glass vial. Phosphate buffer was added to rehydrate the film at a concentration of 1 mg/ml. The solutions were annealed at 70°C for 45 mins then allowed to equilibrate over 16 hrs at room temperature and subjected to spin dialysis using a 3K MWCO filter (Amicon Ultra-4, Millipore) to remove any soluble free dye in solution. The samples were incubated with BSA (20 mg/mL) at 37°C and time-resolved fluorescence emission intensity was monitored every 15 mins on a LS-55 fluorescence spectrometer (Perkin Elmer) from 475–650 nm for 24 hrs using an excitation wavelength of 450 nm.

6.4.6 Differential scanning calorimetry (DSC)

DSC measurements were conducted using a VP-Microcal calorimeter (GE). ~550 uL of sample and buffer solutions were degassed for 10 mins before being loaded into two hermetically sealed tantalum cells at a pressure of ~28 psi to prevent water evaporation during the heating cycle. The temperature was increased from 5°C to 60°C at a scanrate of 1 °C/min with 15-minute equilibration at 5°C. Baseline correction and concentration normalization were performed using the Origin software provided by Microcal.

6.4.7 Dynamic light scattering (DLS)

Size distributions of 3HM were measured using a BI-200SM light scattering system (Brookhaven Instruments). Laser light (637 nm, 30 mW) was scattered from aqueous dispersions of 3HM (1 mg/mL) at a 90° scattering geometry with a 100 μm filter. The temperature of the sample cell was maintained at 25°C using a water bath. The autocorrelation function of the scattered light was collected for 1 minute and analyzed to determine the size distribution of 3HM.

Chapter 7

Influence of Di-alkyl Conjugation Architecture on 3-Helix Micelle Stability

§ 7.1 Introduction

Self-assembled nanostructures with tunable properties by controlling the structure or architecture of the building block represents a versatile and highly desirable platform for drug delivery. The self-assembled structures are a result of intricate balance between many competing non-covalent interactions such as electrostatic, hydrophobic, van der Waals, and hydrogen bonds. Although these interactions are individually weak, collectively, they can generate stable assemblies. By tuning the architecture, one can selectively choose to enhance or weaken the interaction between components, thereby changing the energy landscape and subsequently the resulting structure and functionality.

Mono or di-alkyl tails attached to the amine- or carboxy-terminus of peptides have been reported to influence their aggregation and secondary structure in water for synthetic[1, 2] and natural[3, 4] systems. Stupp[5-10] and Tirrell[11-16] have generated peptide amphiphiles by conjugating hydrophobic alkyl chains to hydrophilic amino acid sequences at either the N- or C-terminus. The formation of extensive nanofibers from peptide amphiphiles requires a minimum alkyl chain length of at least 10 carbons[6]. Alkyl chain length can modulate the stability of 3-helix micelles[17]. In addition to alkyl chain length, the architecture of hydrophilic peptide headgroups of peptide amphiphiles have been studied[7, 10]. Branching of the peptide resulted in lower packing efficiency[8] and allows additional space for improved cellular recognition and adhesion properties[9] for artificial matrix applications. Previous studies in our group has shown that the architecture of the trimeric coiled-coil headgroup in 3-helix micelles is crucial for the enhanced kinetic stability and slow subunit desorption rates[18]. Although alkyl chain length and peptide headgroup architecture has been investigated for many systems, the effect of alkyl chain conjugation architecture to peptide headgroups has yet to be explored.

The molecular architecture of building blocks affects internal order of the self-assembled nanostructure and subsequently can have a large impact on the biological performance of self-assembled nanocarriers. We hypothesize that the architecture of conjugated di-alkyl chains could have an impact on the stability of 3-helix micelles by altering the efficiency of alkyl packing. Here, we study the effect of modifying di-alkyl conjugation architecture on the packing of alkyl chains within the micelle hydrophobic core as well as the micellar stability. Peptide-PEG-alkyl hybrid conjugates with different alkyl architectures were generated while maintaining a similar hydrophilic–lipophilic balance. The results show that alkyl chains conjugated to ε-amine of adjacent lysine residues of a coiled-coil peptide display a higher melting transition temperature and enhanced micellar stability.

§ 7.2 Synthesis of N-alkylated and C-alkylated conjugates

1CW (EVEALEKKVAALESKVQALEKKVEALEHGW) peptide was synthesized at a 50 μmol scale on PAL-PEG polystyrene resin (ThermoFisher Scientific) using solid phase peptide synthesis. Depending on whether N-alkylation or C-alkylation was desired, Fmoc-Lys(Fmoc)-OH or Fmoc-GG-Lys(Alloc)-Lys(Alloc)-OH modifications was made to the 1CW peptide at the N- or C-terminus, respectively. Scheme 7.1 shows the synthetic route to achieve (A) C-alkylated and (B) N-alkylated amphiphiles.

Prior to C-alkylation, the N-terminus of the peptide was either acetylated using acetic anhydride:pyridine (1:1 volume ratio) or PEGylated with α-carboxy-ω-methoxy-poly(ethylene oxide) (750 g/mol) using HATU/DIPEA chemistry. C-alkylation then required selective removal of the allyl protecting groups on both ε-amines of the two lysine residues at the C-terminus using 0.2 eq. $Pd(PPh_3)$ catalyst and 24 eq. phenylsilane. Hexadecanoic acid or octadecanoic acid were coupled to the deprotected amine functional group using HBTU/DIPEA chemistry. In total, four variants of C-alkylated amphiphiles were synthesized: hexadecane-acetylated, octadecane-acetylated, hexadecane-PEGylated, and octadecane-PEGylated henceforth referred to as C-16(Ac), C-18(Ac), C-16(P), and C-18(P), respectively.

For N-alkylation, a 20% piperidine solution was used to selectively remove the α- and ε-Fmoc protecting groups on the single lysine residue, allowing two molecules of hexadecenoic or octadecanoic acid to be conjugated to the N-terminus, referred to as N-16 and N-18, respectively.

After alkylation of the peptide, the amphiphiles were cleaved from the resin using a cocktail of TFA/TIS/H_2O (90:8:2). The crude products were precipitated and washed using cold diethyl ether and dried in vacuo to obtain a dry white powder in ~85% yield. Crude amphiphiles were dissolved in phosphate buffer (pH 7.4, 25 mM) at a concentration of ~20-30 mg/mL, depending on hexadecane or octadecane, and 4 eq. of α-maleimide-ω-methoxy-poly(ethylene oxide) (2000 g/mol) added and stirred overnight. Purification of the conjugates was achieved using a linear gradient of water:acetonitrile (A:B) with 0.1% v/v TFA from 30% B to 100% B in 30 mins at a flowrate of 8 mL/min. Purified conjugates eluted around 85% B. Octadecane conjugates were purified using isopropanol plus 0.1% v/v TFA as solvent B and eluted ~90% B.

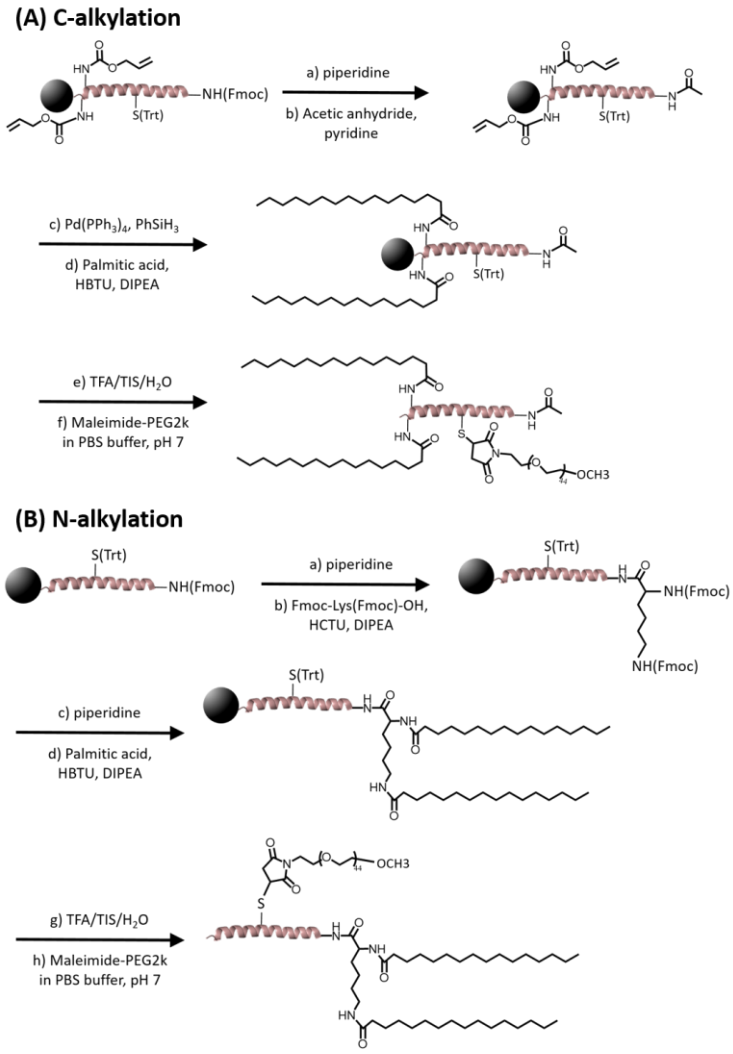

Scheme 7.1. Synthetic scheme of alkylation at the C- and N-terminus of the 1CW peptide. (A) Alkylation of 1CW modified with GGKK residues at the C-terminus through both ε-amines of two adjacent lysine residues. (B) Alkylation of 1CW at the N-terminus through α- and ε-amine of a single lysine residue.

§ 7.3 Results and discussion

7.3.1 Stability of micelles in serum protein

For any intraveneous applications, stability of nanoparticles in serum protein is crucial for minimal drug leakage in circulation. The stability of C-alkylated 3-helix micelles was compared to that of N-alkylated 3-helix micelles using FRET, shown in Figure 7.1. N-16 displayed good micelle stability, FRET ratio decreased ~5% over 24 hrs. Acetylated variants of C-16 and C-18 showed enhanced stability over the same time period, only decreased by ~1% in FRET ratio.

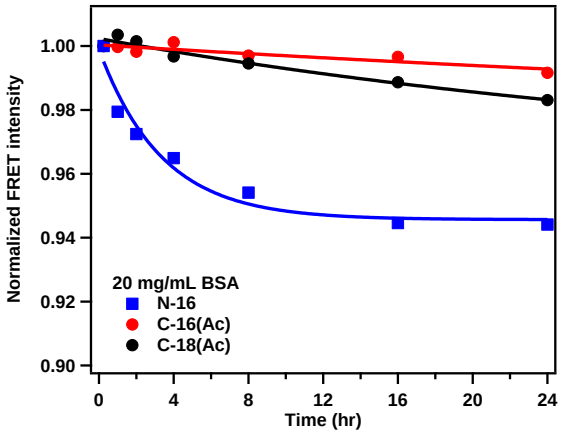

Figure 7.1. FRET stability of N-16 (blue) compared to C-16(Ac) (red) and C-18(Ac) (black).

7.3.2 Packing of C-alkylated chains in 3-helix micelles

To understand the molecular contribution of C-alkylation on the enhanced stability of 3-helix micelles, DSC was used to investigate the alkyl packing behavior of both N-alkylated and C-alkylated 3-helix micelles, shown in Figure 7.2.

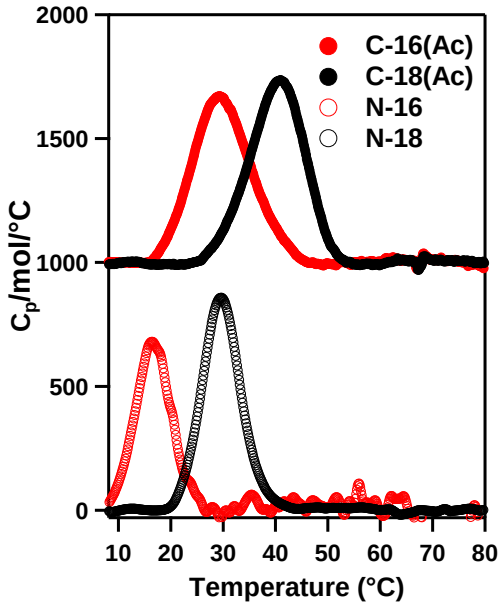

Figure 7.2. DSC measurements showing N-alkylated 3HM in empty circles and C-alkylated 3HM in solid circles. 3HM conjugated with hexadecenoic acid and octadecanoic acid shown in red and black, respectively.

C-alkylated 3-helix micelles exhibited ~10°C higher transition temperature for the same alkyl chain length compared to N-alkylated 3-helix micelles. It is interesting to note that C-18(Ac) micelle has a melting temperature at 40°C which is higher that body temperature (37°C).

7.3.3 Effect of di-alkyl architecture on peptide secondary structure

Our previous studies have shown that the secondary and tertiary structure of the peptide is crucial to maintain high kinetic stability of the 3-helix micelles[18]. We use circular dichroism to probe the effect of C-alkylation on the peptide secondary and tertiary structure. Figure 7.3 shows the spectrum of C-16(Ac) compared to N-16 micelles. C-alkylation resulted in a ~10% decrease in the helical content of the peptide. However, the decrease in helical content did not affect the formation of coiled-coil structure, as shown from the ratio of ellipticity at (222/208 nm) maintained above 1.

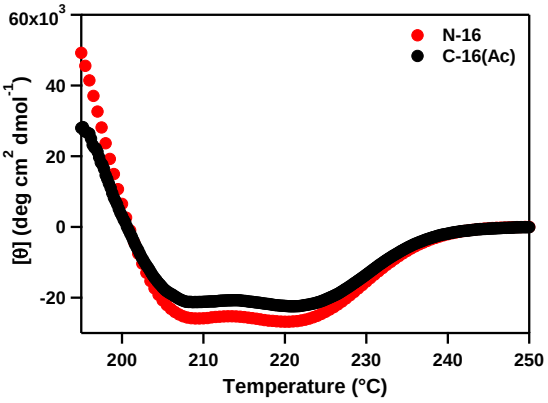

Figure 7.3. Circular dichroism spectra of N-16 and C-16(Ac) in red and black, respectively.

7.3.4 Effect of N-PEGylation on C-alkylated 3-helix micelles

Non-specific absorption of serum proteins on the surface of the micelles can lead to off-target, and often undesired opsonization and sequestration by macrophages thereby cleared from the system rapidly. To overcome this problem, surface PEGylation of particles is a common and effective method to impart the particles with 'stealth' properties, enhancing the circulation lifetime. In this section, we seek to understand the effect of surface PEGylation on the C-alkylated 3-helix micelles, namely stability, secondary structure of the helical peptide, and alkyl packing in the hydrophobic core of 3-helix micelles.

Figure 7.4 shows the FRET stability of N-PEGylated 3-helix micelles with C-alkylation. The FRET ratio remains close to unity and decreased less than 1% over a period of 24 hrs under incubation with 20 mg/mL bovine serum albumin. This indicates that the PEGylated micelles shown in Figure 7.4 are marginally more stable in serum albumin than the acetylated micelles shown in Figure 7.1.

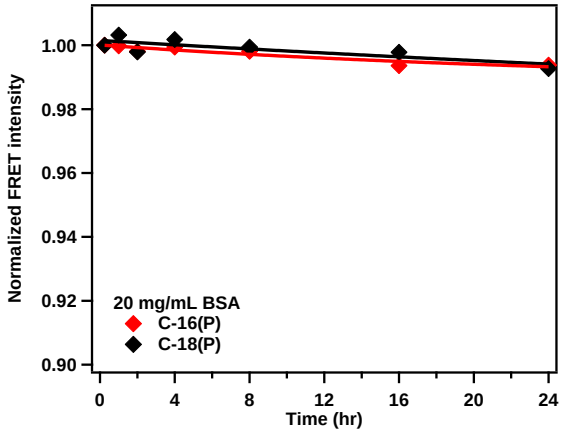

Figure 7.4. Stability of N-PEGylated 3-helix micelles with C-alkylation in 20 mg/mL bovine serum albumin.

For C-alkylated 3-helix micelles, the effect of PEGylation and acetylation at the N-terminus were compared. Figure 7.5 shows that the circular dichroism spectra of acetylated and PEGylated C-alkyl 3-helix micelles overlap for the same alkyl chain length, indicating that PEGylation does not adversely affect the secondary structure of the coiled-coil peptide. However, increasing the alkyl chain length decreases the helicity of the peptide as seen from the less negative minima at 222 nm.

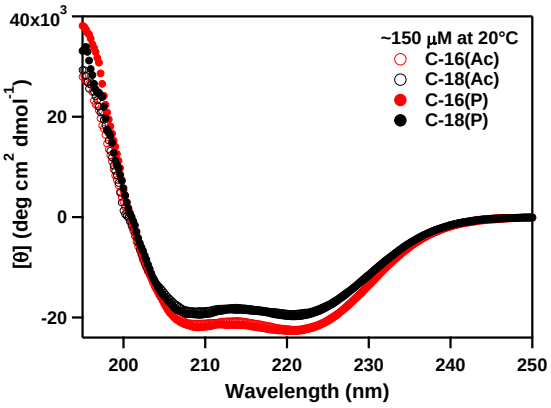

Figure 7.5. Comparison of circular dichroism spectra for N-PEGylated (solid circles) and N-acetylated (empty circles) 3-helix micelles with C-alkylation. Red and black represent micelles conjugated with hexadecenoic acid and octadecanoic acid, respectively.

Figure 7.6 shows the alkyl phase transition for N-PEGylated and N-alkylated 3-helix micelles with C-alkylation. There is no difference in the transition temperature between

PEGylated and acetylated 3-helix micelles, indicating that PEGylation of the N-terminus for C-alkylated micelles does not affect the packing of alkyl chains within the hydrophobic core.

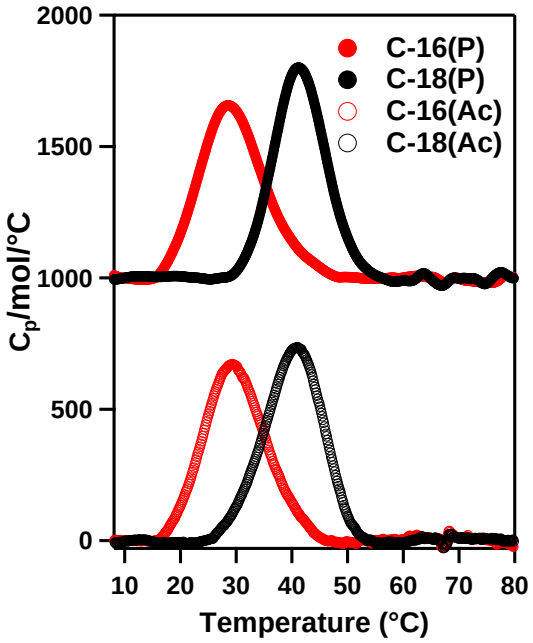

Figure 7.6. DSC thermograms of C-alkylated 3-helix micelles with N-PEGylation (solid circles) and N-acetylation (empty circles).

§ 7.4 Conclusion

This study shows that 3-helix micelles can be alkylated either at the N- or C-terminus of the helical peptide with high retention of the helical and coiled-coil peptide structure. Alkylation at the C-terminus through conjugation to ε-amines of two adjacent lysine residues was shown to enhance the stability of the resulting 3-helix micelles. The hydrophilic–lipophilic balance of the system was not changed – merely the conjugation architecture, directly resulting in a significant stability enhancement. The increased stability was correlated to the increase in alkyl melting temperature within the hydrophobic core of the micelles. Besides increasing the stability of 3-helix micelles, C-alkylation using this new di-alkyl architecture also allows the N-terminus of the peptide to be functionalized with PEG or targeting ligands such as small molecules and peptides which require amine-based conjugation methods. This study opens new avenues to generate 3-helix micelles with tunable stability by modifying the di-alkyl architecture.

§ 7.5 Experimental methods

7.5.1 Forster resonance energy transfer

A FRET pair, 3,3′-dioctadecyloxacarbocyanine perchlorate (DiO, donor) and 1,1′-dioctadecyl-3,3,3′,3′-tetramethylindocarbocyanine perchlorate (DiI, acceptor) and the different variants of 3-helix micelles were co-dissolved in methanol. The methanol was evaporated under vacuum at 60°C for 3 hrs in a glass vial to form a thin film. Phosphate buffer was added to rehydrate the film at a concentration of 1 mg/ml. The solutions were annealed at 70°C for 45 mins then allowed to equilibrate over 16 hrs at room temperature and subjected to spin dialysis using a 3K MWCO filter (Amicon Ultra-4, Millipore) to remove any soluble free dye in solution. The samples were incubated with BSA (20 mg/mL) at 37°C and time-resolved fluorescence emission intensity was monitored every 15 mins on a LS-55 fluorescence spectrometer (Perkin Elmer) from 475–650 nm for 24 hrs using an excitation wavelength of 450 nm.

7.5.2 Differential scanning calorimetry

DSC measurements were conducted using a VP-Microcal calorimeter (GE). ~550 uL of sample and buffer solutions were degassed for 10 mins before being loaded into two hermetically sealed tantalum cells at a pressure of ~28 psi to prevent water evaporation during the heating cycle. The temperature was increased from 5°C to 80°C at a scanrate of 1 °C/min with 15-minute equilibration at 5°C. Baseline correction and concentration normalization were performed using the Origin software provided by Microcal.

7.5.3 Circular dichroism

Circular dichroism measurements for secondary and tertiary structure characterization were conducted on a J-815 spectrometer (Jasco) using a quartz cell with 0.1 cm pathlength. All samples were prepared at a concentration ~150 μM in phosphate buffer (25 mM, pH 7.4). CD spectra were recorded from 250 nm to 190 nm at 0.5 nm intervals with a scanrate of 100 nm/min and a response time of 4 s. The measured ellipticity was normalized by concentration and converted to molar residual ellipticity. The mean residue ellipticity for a 100% helix peptide of infinite length[19-21] was taken to be −37400 deg cm^2 $dmol^{-1}$.

Afterword

3-helix micelle show great potential as nanocarriers for drug delivery. The ability of 3-helix micelle to penetrate various biological barriers such as the blood-brain barrier and achieve deep penetration within dense tumor tissue is inexplicable, for now. The mechanical property of 3-helix micelle holds the key to understanding its exceptional behavior when infiltrating biological barriers typically not accessible to macromolecules or nanoparticles. Fundamental studies to probe the deformability and structure of 3-helix micelle under physiologically-relevant shear stress or pressure would have important biological implications for the development of future nanocarriers.

The discovery of exceptionally high water content in 3-helix micelles suggests that they might be a good candidate for hydrogel applications. To facilitate cross-linking, cross-linkable moieties can be attached to the surface of 3-helix micelles. Varying the number of linkers available on the micelle surface can tune the extent of cross-linking to potentially generate hydrogels with different degrees of stiffness for various biological applications.

3-helix micelle also presents an attractive platform to design nanoparticles for selective targeting to cells as alluded to in Chapter 6. Attachment of specific ligands to the surface of the micelles can achieve active targeting to diseased cells. Biological studies that vary the local ligand density by defining the coiled-coil oligomeric state could elucidate the effect of local ligand cluster size on specific ligand-receptor interaction affinity and the subsequent endocytosis efficiency of the nanocarrier. Furthermore, the possibility of generating 'patchy' or Janus micelles on a sub-20 nm scale could have a huge impact on cellular uptake for targeted delivery applications. Detailed characterization of the structure and spatial distribution of the coiled-coil amphiphiles within mixed micelles is required to establish structure-function relationships. Moreover, a fundamental understanding of the assembly pathway is necessary to control their self-assembly into well-defined nanostructures, if the mixed coiled-coil micelle platform is to fulfil its full potential for biological applications. Further studies to elucidate the origin of nano-phase separation within the mixed coiled-coil micelles could open new avenues to generate well-defined 'patchy' particles in the unique size range of tens of nanometers.

References

Chapter 1

1. Zhang, L.; Gu, F. X.; Chan, J. M.; Wang, A. Z.; Langer, R. S.; Farokhzad, O. C., Nanoparticles in medicine: therapeutic applications and developments. *Clin. Pharmacol. Ther.* **2008,** 83, (5), 761-9.
2. Gabizon, A.; Catane, R.; Uziely, B.; Kaufman, B.; Safra, T.; Cohen, R.; Martin, F.; Huang, A.; Barenholz, Y., Prolonged circulation time and enhanced accumulation in malignant exudates of doxorubicin encapsulated in polyethylene-glycol coated liposomes. *Cancer Res.* **1994,** 54, (4), 987-92.
3. Kim, D. W.; Kim, S. Y.; Kim, H. K.; Kim, S. W.; Shin, S. W.; Kim, J. S.; Park, K.; Lee, M. Y.; Heo, D. S., Multicenter phase II trial of Genexol-PM, a novel Cremophor-free, polymeric micelle formulation of paclitaxel, with cisplatin in patients with advanced non-small-cell lung cancer. *Ann. Oncol.* **2007,** 18, (12), 2009-14.
4. Lee, K. S.; Chung, H. C.; Im, S. A.; Park, Y. H.; Kim, C. S.; Kim, S. B.; Rha, S. Y.; Lee, M. Y.; Ro, J., Multicenter phase II trial of Genexol-PM, a Cremophor-free, polymeric micelle formulation of paclitaxel, in patients with metastatic breast cancer. *Breast Cancer Res. Treat.* **2008,** 108, (2), 241-50.
5. https://clinicaltrials.gov/.
6. Kim, S. C.; Kim, D. W.; Shim, Y. H.; Bang, J. S.; Oh, H. S.; Wan Kim, S.; Seo, M. H., In vivo evaluation of polymeric micellar paclitaxel formulation: toxicity and efficacy. *J. Control. Release* **2001,** 72, (1-3), 191-202.
7. O'Brien, M. E. R.; Wigler, N.; Inbar, M.; Rosso, R.; Grischke, E.; Santoro, A.; Catane, R.; Kieback, D. G.; Tomczak, P.; Ackland, S. P.; Orlandi, F.; Mellars, L.; Alland, L.; Tendler, C.; Grp, C. B. C. S., Reduced cardiotoxicity and comparable efficacy in a phase III trial of pegylated liposomal doxorubicin HCl (CAELYX (TM)/Doxil (R)) versus conventional doxorubicin for first-line treatment of metastatic breast cancer. *Ann. Oncol.* **2004,** 15, (3), 440-449.
8. Gradishar, W. J.; Tjulandin, S.; Davidson, N.; Shaw, H.; Desai, N.; Bhar, P.; Hawkins, M.; O'Shaughnessy, J., Phase III trial of nanoparticle albumin-bound paclitaxel compared with polyethylated castor oil-based paclitaxel in women with breast cancer. *J. Clin. Oncol.* **2005,** 23, (31), 7794-7803.
9. Mitragotri, S., Devices for overcoming biological barriers: The use of physical forces to disrupt the barriers. *Adv. Drug Deliver. Rev.* **2013,** 65, (1), 100-103.
10. Barua, S.; Mitragotri, S., Challenges associated with penetration of nanoparticles across cell and tissue barriers: A review of current status and future prospects. *Nano Today* **2014,** 9, (2), 223-243.
11. Sriraman, S. K.; Aryasomayajula, B.; Torchilin, V. P., Barriers to drug delivery in solid tumors. *Tissue Barriers* **2014,** 2, (3), e29528.
12. Blanco, E.; Shen, H.; Ferrari, M., Principles of nanoparticle design for overcoming biological barriers to drug delivery. *Nat. Biotechnol.* **2015,** 33, (9), 941-951.

13. Venturoli, D.; Rippe, B., Ficoll and dextran vs. globular proteins as probes for testing glomerular permselectivity: effects of molecular size, shape, charge, and deformability. *Am. J. Physiol. Renal Physiol.* **2005,** 288, (4), F605-13.
14. Choi, H. S.; Liu, W.; Misra, P.; Tanaka, E.; Zimmer, J. P.; Ipe, B. I.; Bawendi, M. G.; Frangioni, J. V., Renal Clearance of Nanoparticles. *Nat. Biotechnol.* **2007,** 25, (10), 1165-1170.
15. Longmire, M.; Choyke, P. L.; Kobayashi, H., Clearance Properties of Nano-sized Particles and Molecules as Imaging Agents: Considerations and Caveats. *Nanomedicine (London, England)* **2008,** 3, (5), 703-717.
16. Cabral, H.; Matsumoto, Y.; Mizuno, K.; Chen, Q.; Murakami, M.; Kimura, M.; Terada, Y.; Kano, M. R.; Miyazono, K.; Uesaka, M.; Nishiyama, N.; Kataoka, K., Accumulation of sub-100 nm polymeric micelles in poorly permeable tumours depends on size. *Nat. Nanotechnol.* **2011,** 6, (12), 815-823.
17. Popović, Z.; Liu, W.; Chauhan, V. P.; Lee, J.; Wong, C.; Greytak, A. B.; Insin, N.; Nocera, D. G.; Fukumura, D.; Jain, R. K.; Bawendi, M. G., A nanoparticle size series for in vivo fluorescence imaging. *Angew. Chem. Int. Ed. Engl.* **2010,** 49, (46), 8649-8652.
18. Vakoc, B. J.; Lanning, R. M.; Tyrrell, J. A.; Padera, T. P.; Bartlett, L. A.; Stylianopoulos, T.; Munn, L. L.; Tearney, G. J.; Fukumura, D.; Jain, R. K.; Bouma, B. E., Three-dimensional microscopy of the tumor microenvironment in vivo using optical frequency domain imaging. *Nat. Med.* **2009,** 15, (10), 1219-1223.
19. Hobbs, S. K.; Monsky, W. L.; Yuan, F.; Roberts, W. G.; Griffith, L.; Torchilin, V. P.; Jain, R. K., Regulation of transport pathways in tumor vessels: role of tumor type and microenvironment. *Proc. Natl. Acad. Sci. USA* **1998,** 95, (8), 4607-12.
20. Hashizume, H.; Baluk, P.; Morikawa, S.; McLean, J. W.; Thurston, G.; Roberge, S.; Jain, R. K.; McDonald, D. M., Openings between defective endothelial cells explain tumor vessel leakiness. *Am. J. Pathol.* **2000,** 156, (4), 1363-80.
21. Matsumura, Y.; Maeda, H., A new concept for macromolecular therapeutics in cancer chemotherapy: mechanism of tumoritropic accumulation of proteins and the antitumor agent smancs. *Cancer Res.* **1986,** 46, (12 Pt 1), 6387-92.
22. Maeda, H.; Wu, J.; Sawa, T.; Matsumura, Y.; Hori, K., Tumor vascular permeability and the EPR effect in macromolecular therapeutics: a review. *J. Control. Release* **2000,** 65, (1-2), 271-84.
23. Prabhakar, U.; Maeda, H.; Jain, R. K.; Sevick-Muraca, E. M.; Zamboni, W.; Farokhzad, O. C.; Barry, S. T.; Gabizon, A.; Grodzinski, P.; Blakey, D. C., Challenges and Key Considerations of the Enhanced Permeability and Retention Effect for Nanomedicine Drug Delivery in Oncology. *Cancer Res.* **2013,** 73, (8), 2412-2417.
24. Nichols, J. W.; Bae, Y. H., EPR: Evidence and fallacy. *J. Control. Release* **2014,** 190, 451-64.
25. Clark, A. J.; Wiley, D. T.; Zuckerman, J. E.; Webster, P.; Chao, J.; Lin, J.; Yen, Y.; Davis, M. E., CRLX101 nanoparticles localize in human tumors and not in adjacent, nonneoplastic tissue after intravenous dosing. *Proc. Natl. Acad. Sci. USA* **2016,** 113, (14), 3850-3854.
26. Gilkes, D. M.; Semenza, G. L.; Wirtz, D., Hypoxia and the extracellular matrix: drivers of tumour metastasis. *Nat. Rev. Cancer* **2014,** 14, (6), 430-439.

27. Alexandrakis, G.; Brown, E. B.; Tong, R. T.; McKee, T. D.; Campbell, R. B.; Boucher, Y.; Jain, R. K., Two-photon fluorescence correlation microscopy reveals the two-phase nature of transport in tumors. *Nat. Med.* **2004,** 10, (2), 203-7.
28. Yuan, F.; Leunig, M.; Huang, S. K.; Berk, D. A.; Papahadjopoulos, D.; Jain, R. K., Microvascular permeability and interstitial penetration of sterically stabilized (stealth) liposomes in a human tumor xenograft. *Cancer Res.* **1994,** 54, (13), 3352-6.
29. McKee, T. D.; Grandi, P.; Mok, W.; Alexandrakis, G.; Insin, N.; Zimmer, J. P.; Bawendi, M. G.; Boucher, Y.; Breakefield, X. O.; Jain, R. K., Degradation of fibrillar collagen in a human melanoma xenograft improves the efficacy of an oncolytic herpes simplex virus vector. *Cancer Res.* **2006,** 66, (5), 2509-13.
30. Perrault, S. D.; Walkey, C.; Jennings, T.; Fischer, H. C.; Chan, W. C. W., Mediating Tumor Targeting Efficiency of Nanoparticles Through Design. *Nano Lett.* **2009,** 9, (5), 1909-1915.
31. Albanese, A.; Lam, A. K.; Sykes, E. A.; Rocheleau, J. V.; Chan, W. C. W., Tumour-on-a-chip provides an optical window into nanoparticle tissue transport. *Nat. Commun.* **2013,** 4.
32. Diop-Frimpong, B.; Chauhan, V. P.; Krane, S.; Boucher, Y.; Jain, R. K., Losartan inhibits collagen I synthesis and improves the distribution and efficacy of nanotherapeutics in tumors. *Proc. Natl. Acad. Sci. USA* **2011,** 108, (7), 2909-2914.
33. Li, H.-J.; Du, J.-Z.; Liu, J.; Du, X.-J.; Shen, S.; Zhu, Y.-H.; Wang, X.; Ye, X.; Nie, S.; Wang, J., Smart Superstructures with Ultrahigh pH-Sensitivity for Targeting Acidic Tumor Microenvironment: Instantaneous Size Switching and Improved Tumor Penetration. *ACS Nano* **2016,** 10, (7), 6753-6761.
34. Wong, C.; Stylianopoulos, T.; Cui, J.; Martin, J.; Chauhan, V. P.; Jiang, W.; Popović, Z.; Jain, R. K.; Bawendi, M. G.; Fukumura, D., Multistage nanoparticle delivery system for deep penetration into tumor tissue. *Proc. Natl. Acad. Sci. USA* **2011,** 108, (6), 2426-2431.
35. Monsky, W. L.; Fukumura, D.; Gohongi, T.; Ancukiewcz, M.; Weich, H. A.; Torchilin, V. P.; Yuan, F.; Jain, R. K., Augmentation of transvascular transport of macromolecules and nanoparticles in tumors using vascular endothelial growth factor. *Cancer Res.* **1999,** 59, (16), 4129-35.
36. Maeda, H.; Fang, J.; Inutsuka, T.; Kitamoto, Y., Vascular permeability enhancement in solid tumor: Various factors, mechanisms involved and its implications. *Int. Immunopharmacol.* **2003,** 3, (3), 319-328.
37. Maeda, H.; Noguchi, Y.; Sato, K.; Akaike, T., Enhanced vascular permeability in solid tumor is mediated by nitric oxide and inhibited by both new nitric oxide scavenger and nitric oxide synthase inhibitor. *Jpn. J. Cancer Res.* **1994,** 85, (4), 331-334.
38. Yasuda, H.; Yanagihara, K.; Nakayama, K.; Mio, T.; Sasaki, T.; Asada, M.; Yamaya, M.; Fukushima, M., Therapeutic Applications of Nitric Oxide for Malignant Tumor in Animal Models and Human Studies. In *Nitric Oxide (NO) and Cancer: Prognosis, Prevention, and Therapy*, Bonavida, B., Ed. Springer New York: New York, NY, 2010; pp 419-441.
39. Maeda, H., Macromolecular therapeutics in cancer treatment: the EPR effect and beyond. *J. Control. Release* **2012,** 164, (2), 138-44.

40. Maeda, H.; Nakamura, H.; Fang, J., The EPR effect for macromolecular drug delivery to solid tumors: Improvement of tumor uptake, lowering of systemic toxicity, and distinct tumor imaging in vivo. *Adv. Drug Deliver. Rev.* **2013,** 65, (1), 71-9.
41. Nagamitsu, A.; Greish, K.; Maeda, H., Elevating blood pressure as a strategy to increase tumor-targeted delivery of macromolecular drug SMANCS: Cases of advanced solid tumors. *Jpn. J. Clin. Oncol.* **2009,** 39, (11), 756-766.
42. Ruoslahti, E., Specialization of tumour vasculature. *Nat. Rev. Cancer* **2002,** 2, (2), 83-90.
43. Jain, R. K., Transport of Molecules, Particles, and Cells in Solid Tumors. *Annu. Rev. Biomed. Eng.* **1999,** 1, (1), 241-263.
44. Jain, R. K.; Stylianopoulos, T., Delivering nanomedicine to solid tumors. *Nat. Rev. Clin. Oncol.* **2010,** 7, (11), 653-64.
45. Jain, R. K., Normalizing tumor microenvironment to treat cancer: bench to bedside to biomarkers. *J. Clin. Oncol.* **2013,** 31, (17), 2205-18.
46. Chauhan, V. P.; Stylianopoulos, T.; Martin, J. D.; Popovic, Z.; Chen, O.; Kamoun, W. S.; Bawendi, M. G.; Fukumura, D.; Jain, R. K., Normalization of tumour blood vessels improves the delivery of nanomedicines in a size-dependent manner. *Nat. Nanotechnol.* **2012,** 7, (6), 383-388.
47. Cedervall, T.; Lynch, I.; Lindman, S.; Berggard, T.; Thulin, E.; Nilsson, H.; Dawson, K. A.; Linse, S., Understanding the nanoparticle-protein corona using methods to quantify exchange rates and affinities of proteins for nanoparticles. *Proc. Natl. Acad. Sci. USA* **2007,** 104, (7), 2050-5.
48. Monopoli, M. P.; Aberg, C.; Salvati, A.; Dawson, K. A., Biomolecular coronas provide the biological identity of nanosized materials. *Nat. Nanotechnol.* **2012,** 7, (12), 779-86.
49. Milani, S.; Bombelli, F. B.; Pitek, A. S.; Dawson, K. A.; Radler, J., Reversible versus Irreversible Binding of Transferrin to Polystyrene Nanoparticles: Soft and Hard Corona. *ACS Nano* **2012,** 6, (3), 2532-2541.
50. Lundqvist, M.; Stigler, J.; Elia, G.; Lynch, I.; Cedervall, T.; Dawson, K. A., Nanoparticle size and surface properties determine the protein corona with possible implications for biological impacts. *Proc. Natl. Acad. Sci. USA* **2008,** 105, (38), 14265-14270.
51. Moghimi, S. M.; Hunter, A. C.; Murray, J. C., Long-Circulating and Target-Specific Nanoparticles: Theory to Practice. *Pharmacol. Rev.* **2001,** 53, (2), 283-318.
52. Bae, Y. H.; Park, K., Targeted drug delivery to tumors: Myths, reality and possibility. *J. Control. Release* **2011,** 153, (3), 198-205.
53. Harris, J. M.; Chess, R. B., Effect of pegylation on pharmaceuticals. *Nat. Rev. Drug Discovery* **2003,** 2, (3), 214-221.
54. Veronese, F. M.; Pasut, G., PEGylation, successful approach to drug delivery. *Drug Discov. Today* **2005,** 10, (21), 1451-1458.
55. Armstrong, J. K.; Hempel, G.; Koling, S.; Chan, L. S.; Fisher, T.; Meiselman, H. J.; Garratty, G., Antibody against poly(ethylene glycol) adversely affects PEG-asparaginase therapy in acute lymphoblastic leukemia patients. *Cancer* **2007,** 110, (1), 103-111.

56. Garay, R. P.; El-Gewely, R.; Armstrong, J. K.; Garratty, G.; Richette, P., Antibodies against polyethylene glycol in healthy subjects and in patients treated with PEG-conjugated agents. *Expert Opin. Drug Deliv.* **2012,** 9, (11), 1319-23.
57. Zhang, P.; Sun, F.; Liu, S.; Jiang, S., Anti-PEG antibodies in the clinic: Current issues and beyond PEGylation. *J. Control. Release* **2016**.
58. Ishida, T.; Ichihara, M.; Wang, X.; Yamamoto, K.; Kimura, J.; Majima, E.; Kiwada, H., Injection of PEGylated liposomes in rats elicits PEG-specific IgM, which is responsible for rapid elimination of a second dose of PEGylated liposomes. *J. Control. Release* **2006,** 112, (1), 15-25.
59. Ishida, T.; Kiwada, H., Anti-polyethyleneglycol antibody response to PEGylated substances. *Biol. Pharm. Bull.* **2013,** 36, (6), 889-91.
60. Elsabahy, M.; Zhang, S.; Zhang, F.; Deng, Z. J.; Lim, Y. H.; Wang, H.; Parsamian, P.; Hammond, P. T.; Wooley, K. L., Surface charges and shell crosslinks each play significant roles in mediating degradation, biofouling, cytotoxicity and immunotoxicity for polyphosphoester-based nanoparticles. *Scientific Reports* **2013,** 3, 3313.
61. Schottler, S.; Becker, G.; Winzen, S.; Steinbach, T.; Mohr, K.; Landfester, K.; Mailander, V.; Wurm, F. R., Protein adsorption is required for stealth effect of poly(ethylene glycol)- and poly(phosphoester)-coated nanocarriers. *Nat. Nanotechnol.* **2016,** 11, (4), 372-7.
62. Cao, Z.; Jiang, S., Super-hydrophilic zwitterionic poly(carboxybetaine) and amphiphilic non-ionic poly(ethylene glycol) for stealth nanoparticles. *Nano Today* **2012,** 7, (5), 404-413.
63. Elsabahy, M.; Li, A.; Zhang, F.; Sultan, D.; Liu, Y.; Wooley, K. L., Differential immunotoxicities of poly(ethylene glycol)- vs. poly(carboxybetaine)-coated nanoparticles. *J. Control. Release* **2013,** 172, (3), 641-652.
64. Yang, W.; Liu, S.; Bai, T.; Keefe, A. J.; Zhang, L.; Ella-Menye, J.-R.; Li, Y.; Jiang, S., Poly(carboxybetaine) nanomaterials enable long circulation and prevent polymer-specific antibody production. *Nano Today* **2014,** 9, (1), 10-16.
65. Zhang, P.; Sun, F.; Tsao, C.; Liu, S.; Jain, P.; Sinclair, A.; Hung, H.-C.; Bai, T.; Wu, K.; Jiang, S., Zwitterionic gel encapsulation promotes protein stability, enhances pharmacokinetics, and reduces immunogenicity. *Proc. Natl. Acad. Sci. USA* **2015,** 112, (39), 12046-12051.
66. Liu, S.; Jiang, S., Zwitterionic polymer-protein conjugates reduce polymer-specific antibody response. *Nano Today* **2016,** 11, (3), 285-291.
67. Schellenberger, V.; Wang, C. W.; Geething, N. C.; Spink, B. J.; Campbell, A.; To, W.; Scholle, M. D.; Yin, Y.; Yao, Y.; Bogin, O.; Cleland, J. L.; Silverman, J.; Stemmer, W. P., A recombinant polypeptide extends the in vivo half-life of peptides and proteins in a tunable manner. *Nat. Biotechnol.* **2009,** 27, (12), 1186-90.
68. Podust, V. N.; Balan, S.; Sim, B.-C.; Coyle, M. P.; Ernst, U.; Peters, R. T.; Schellenberger, V., Extension of in vivo half-life of biologically active molecules by XTEN protein polymers. *J. Control. Release* **2016,** 240, 52-66.
69. Ishihara, T.; Maeda, T.; Sakamoto, H.; Takasaki, N.; Shigyo, M.; Ishida, T.; Kiwada, H.; Mizushima, Y.; Mizushima, T., Evasion of the Accelerated Blood Clearance Phenomenon by Coating of Nanoparticles with Various Hydrophilic Polymers. *Biomacromolecules* **2010,** 11, (10), 2700-2706.

70. Amoozgar, Z.; Yeo, Y., Recent advances in stealth coating of nanoparticle drug delivery systems. *Wiley Interdisciplinary Reviews: Nanomedicine and Nanobiotechnology* **2012,** 4, (2), 219-33.
71. Niitsu, Y.; Kohgo, Y.; Nishisato, T.; Kondo, H.; Kato, J.; Urushizaki, Y.; Urushizaki, I., Transferrin receptors in human cancerous tissues. *Tohoku J. Exp. Med.* **1987,** 153, (3), 239-43.
72. Qian, Z. M.; Li, H.; Sun, H.; Ho, K., Targeted Drug Delivery via the Transferrin Receptor-Mediated Endocytosis Pathway. *Pharmacol. Rev.* **2002,** 54, (4), 561-587.
73. Garin-Chesa, P.; Campbell, I.; Saigo, P. E.; Lewis, J. L.; Old, L. J.; Rettig, W. J., Trophoblast and ovarian cancer antigen LK26. Sensitivity and specificity in immunopathology and molecular identification as a folate-binding protein. *The American Journal of Pathology* **1993,** 142, (2), 557-567.
74. Parker, N.; Turk, M. J.; Westrick, E.; Lewis, J. D.; Low, P. S.; Leamon, C. P., Folate receptor expression in carcinomas and normal tissues determined by a quantitative radioligand binding assay. *Anal. Biochem.* **2005,** 338, (2), 284-293.
75. Desgrosellier, J. S.; Cheresh, D. A., Integrins in cancer: biological implications and therapeutic opportunities. *Nat. Rev. Cancer* **2010,** 10, (1), 9-22.
76. Pasqualini, R.; Koivunen, E.; Ruoslahti, E., alpha v Integrins as receptors for tumor targeting by circulating ligands. *Nat. Biotechnol.* **1997,** 15, (6), 542-546.
77. Scaltriti, M.; Baselga, J., The epidermal growth factor receptor pathway: A model for targeted therapy. *Clin. Cancer Res.* **2006,** 12, (18), 5268-5272.
78. Slamon, D. J.; Clark, G. M.; Wong, S. G.; Levin, W. J.; Ullrich, A.; McGuire, W. L., Human breast cancer - correlation of relapse and survival with amplification of the Her-2 Neu oncogene. *Science* **1987,** 235, (4785), 177-182.
79. Slamon, D. J.; Godolphin, W.; Jones, L. A.; Holt, J. A.; Wong, S. G.; Keith, D. E.; Levin, W. J.; Stuart, S. G.; Udove, J.; Ullrich, A.; Press, M. F., Studies of the HER-2/NEU proto-oncogene in human breast and ovarian cancer. *Science* **1989,** 244, (4905), 707-712.
80. Lurje, G.; Lenz, H.-J., EGFR Signaling and Drug Discovery. *Oncology* **2009,** 77, (6), 400-410.
81. Kirpotin, D. B.; Drummond, D. C.; Shao, Y.; Shalaby, M. R.; Hong, K. L.; Nielsen, U. B.; Marks, J. D.; Benz, C. C.; Park, J. W., Antibody targeting of long-circulating lipidic nanoparticles does not increase tumor localization but does increase internalization in animal models. *Cancer Res.* **2006,** 66, (13), 6732-6740.
82. Pirollo, K. F.; Chang, E. H., Does a targeting ligand influence nanoparticle tumor localization or uptake? *Trends Biotechnol.* **2008,** 26, (10), 552-558.
83. Bae, Y.; Nishiyama, N.; Kataoka, K., In vivo antitumor activity of the folate-conjugated pH-Sensitive polymeric micelle selectively releasing adriamycin in the intracellular acidic compartments. *Bioconjugate Chem.* **2007,** 18, (4), 1131-1139.
84. Mamot, C.; Drummond, D. C.; Noble, C. O.; Kallab, V.; Guo, Z.; Hong, K.; Kirpotin, D. B.; Park, J. W., Epidermal growth factor receptor-targeted immunoliposomes significantly enhance the efficacy of multiple anticancer drugs in vivo. *Cancer Res.* **2005,** 65, (24), 11631-11638.

85. van der Meel, R.; Vehmeijer, L. J. C.; Kok, R. J.; Storm, G.; van Gaal, E. V. B., Ligand-targeted particulate nanomedicines undergoing clinical evaluation: Current status. *Adv. Drug Deliver. Rev.* **2013,** 65, (10), 1284-1298.
86. Goodall, S.; Jones, M. L.; Mahler, S., Monoclonal antibody-targeted polymeric nanoparticles for cancer therapy – future prospects. *J. Chem. Technol. Biotechnol.* **2015,** 90, (7), 1169-1176.
87. Xu, L.; Tang, W. H.; Huang, C. C.; Alexander, W.; Xiang, L. M.; Pirollo, K. F.; Rait, A.; Chang, E. H., Systemic p53 gene therapy of cancer with immunolipoplexes targeted by anti-transferrin receptor scFv. *Mol. Med.* **2001,** 7, (10), 723-734.
88. Xu, L.; Huang, C.-C.; Huang, W.; Tang, W.-H.; Rait, A.; Yin, Y. Z.; Cruz, I.; Xiang, L.-M.; Pirollo, K. F.; Chang, E. H., Systemic Tumor-targeted Gene Delivery by Anti-Transferrin Receptor scFv-Immunoliposomes. *Mol. Cancer Ther.* **2002,** 1, (5), 337-346.
89. Senzer, N.; Nemunaitis, J.; Nemunaitis, D.; Bedell, C.; Edelman, G.; Barve, M.; Nunan, R.; Pirollo, K. F.; Rait, A.; Chang, E. H., Phase I Study of a Systemically Delivered p53 Nanoparticle in Advanced Solid Tumors. *Mol. Ther.* **2013,** 21, (5), 1096-1103.
90. Salvati, A.; Pitek, A. S.; Monopoli, M. P.; Prapainop, K.; Bombelli, F. B.; Hristov, D. R.; Kelly, P. M.; Aberg, C.; Mahon, E.; Dawson, K. A., Transferrin-functionalized nanoparticles lose their targeting capabilities when a biomolecule corona adsorbs on the surface. *Nat. Nanotechnol.* **2013,** 8, (2), 137-43.
91. Kozlovskaya, V.; Xue, B.; Kharlampieva, E., Shape-Adaptable Polymeric Particles for Controlled Delivery. *Macromolecules* **2016,** 49, (22), 8373-8386.
92. Zhang, L.; Cao, Z.; Li, Y.; Ella-Menye, J.-R.; Bai, T.; Jiang, S., Softer Zwitterionic Nanogels for Longer Circulation and Lower Splenic Accumulation. *ACS Nano* **2012,** 6, (8), 6681-6686.
93. Merkel, T. J.; Jones, S. W.; Herlihy, K. P.; Kersey, F. R.; Shields, A. R.; Napier, M.; Luft, J. C.; Wu, H.; Zamboni, W. C.; Wang, A. Z.; Bear, J. E.; DeSimone, J. M., Using mechanobiological mimicry of red blood cells to extend circulation times of hydrogel microparticles. *Proc. Natl. Acad. Sci. USA* **2011,** 108, (2), 586-91.
94. Merkel, T. J.; Chen, K.; Jones, S. W.; Pandya, A. A.; Tian, S.; Napier, M. E.; Zamboni, W. E.; DeSimone, J. M., The effect of particle size on the biodistribution of low-modulus hydrogel PRINT particles. *J. Control. Release* **2012,** 162, (1), 37-44.
95. Cui, J.; Bjornmalm, M.; Liang, K.; Xu, C.; Best, J. P.; Zhang, X.; Caruso, F., Super-soft hydrogel particles with tunable elasticity in a microfluidic blood capillary model. *Adv. Mater.* **2014,** 26, (43), 7295-9.
96. Nugent, L. J.; Jain, R. K., Extravascular diffusion in normal and neoplastic tissues. *Cancer Res.* **1984,** 44, (1), 238-44.
97. Pluen, A.; Netti, P. A.; Jain, R. K.; Berk, D. A., Diffusion of macromolecules in agarose gels: comparison of linear and globular configurations. *Biophys. J.* **1999,** 77, (1), 542-552.
98. Mikhail, A. S.; Allen, C., Block copolymer micelles for delivery of cancer therapy: Transport at the whole body, tissue and cellular levels. *J. Control. Release* **2009,** 138, (3), 214-223.
99. Oerlemans, C.; Bult, W.; Bos, M.; Storm, G.; Nijsen, J. F. W.; Hennink, W. E., Polymeric Micelles in Anticancer Therapy: Targeting, Imaging and Triggered Release. *Pharm. Res.* **2010,** 27, (12), 2569-2589.

100. Torchilin, V. P., Structure and design of polymeric surfactant-based drug delivery systems. *J. Control. Release* **2001,** 73, (2–3), 137-172.
101. Kwon, G. S.; Okano, T., Polymeric micelles as new drug carriers. *Adv. Drug Deliver. Rev.* **1996,** 21, (2), 107-116.
102. Glavas, L.; Olsén, P.; Odelius, K.; Albertsson, A.-C., Achieving Micelle Control through Core Crystallinity. *Biomacromolecules* **2013,** 14, (11), 4150-4156.
103. Glavas, L.; Odelius, K.; Albertsson, A. C., Tuning loading and release by modification of micelle core crystallinity and preparation. *Polym. Adv. Technol.* **2015,** 26, (7), 880-888.
104. Vasey, P. A.; Kaye, S. B.; Morrison, R.; Twelves, C.; Wilson, P.; Duncan, R.; Thomson, A. H.; Murray, L. S.; Hilditch, T. E.; Murray, T.; Burtles, S.; Fraier, D.; Frigerio, E.; Cassidy, J., Phase I clinical and pharmacokinetic study of PK1 [N-(2-hydroxypropyl)methacrylamide copolymer doxorubicin]: First member of a new class of chemotherapeutic agents - Drug-polymer conjugates. *Clin. Cancer Res.* **1999,** 5, (1), 83-94.
105. Greish, K.; Sawa, T.; Fang, J.; Akaike, T.; Maeda, H., SMA-doxorubicin, a new polymeric micellar drug for effective targeting to solid tumours. *J. Control. Release* **2004,** 97, (2), 219-230.
106. Iyer, A. K.; Khaled, G.; Fang, J.; Maeda, H., Exploiting the enhanced permeability and retention effect for tumor targeting. *Drug Discov. Today* **2006,** 11, (17–18), 812-818.
107. Kwon, G.; Suwa, S.; Yokoyama, M.; Okano, T.; Sakurai, Y.; Kataoka, K., Enhanced tumor accumulation and prolonged circulation times of micelle-forming poly (ethylene oxide-aspartate) block copolymer-adriamycin conjugates. *J. Control. Release* **1994,** 29, (1), 17-23.
108. Attia, A. B.; Yang, C.; Tan, J. P.; Gao, S.; Williams, D. F.; Hedrick, J. L.; Yang, Y. Y., The effect of kinetic stability on biodistribution and anti-tumor efficacy of drug-loaded biodegradable polymeric micelles. *Biomaterials* **2013,** 34, (12), 3132-40.
109. Wang, J.; Mao, W.; Lock, L. L.; Tang, J.; Sui, M.; Sun, W.; Cui, H.; Xu, D.; Shen, Y., The Role of Micelle Size in Tumor Accumulation, Penetration, and Treatment. *ACS Nano* **2015,** 9, (7), 7195-7206.
110. Dong, H.; Dube, N.; Shu, J. Y.; Seo, J. W.; Mahakian, L. M.; Ferrara, K. W.; Xu, T., Long-Circulating 15 nm Micelles Based on Amphiphilic 3-Helix Peptide–PEG Conjugates. *ACS Nano* **2012,** 6, (6), 5320-5329.
111. Wohlfart, S.; Gelperina, S.; Kreuter, J., Transport of drugs across the blood-brain barrier by nanoparticles. *J. Control. Release* **2012,** 161, (2), 264-73.
112. Seo, J. W.; Ang, J.; Mahakian, L. M.; Tam, S.; Fite, B.; Ingham, E. S.; Beyer, J.; Forsayeth, J.; Bankiewicz, K. S.; Xu, T.; Ferrara, K. W., Self-assembled 20-nm 64Cu-micelles enhance accumulation in rat glioblastoma. *J. Control. Release* **2015,** 220, Part A, 51-60.
113. Salegio, E.; Streeter, H.; Dube, N.; Hadaczek, P.; Samaranch, L.; Kells, A.; San Sebastián, W.; Zhai, Y.; Bringas, J.; Xu, T.; Forsayeth, J.; Bankiewicz, K., Distribution of nanoparticles throughout the cerebral cortex of rodents and non-human primates: Implications for gene and drug therapy. *Frontiers in Neuroanatomy* **2014,** 8, (9).
114. Dube, N.; Shu, J. Y.; Dong, H.; Seo, J. W.; Ingham, E.; Kheirolomoom, A.; Chen, P.-Y.; Forsayeth, J.; Bankiewicz, K.; Ferrara, K. W.; Xu, T., Evaluation of Doxorubicin-

Loaded 3-Helix Micelles as Nanocarriers. *Biomacromolecules* **2013,** 14, (10), 3697-3705.

115. Hansen, A. E.; Petersen, A. L.; Henriksen, J. R.; Boerresen, B.; Rasmussen, P.; Elema, D. R.; Rosenschöld, P. M. a.; Kristensen, A. T.; Kjær, A.; Andresen, T. L., Positron Emission Tomography Based Elucidation of the Enhanced Permeability and Retention Effect in Dogs with Cancer Using Copper-64 Liposomes. *ACS Nano* **2015,** 9, (7), 6985-6995.

Chapter 2

1. D. N. Louis, H. Ohgaki, O. D. Wiestler and W. K. Cavanee, *IARC Press*, 2007.
2. M. Preusser, S. de Ribaupierre, A. Wohrer, S. C. Erridge, M. Hegi, M. Weller and R. Stupp, *Ann Neurol*, 2011, **70**, 9-21.
3. P. Y. Wen and S. Kesari, *New Engl J Med*, 2008, **359**, 492-507.
4. F. Zustovich, G. Lombardi, A. Della Puppa, A. Rotilio, R. Scienza and D. Pastorelli, *Anticancer Res*, 2009, **29**, 4275-4279.
5. A. A. Brandes, U. Basso, M. Reni, F. Vastola, A. Tosoni, G. Cavallo, L. Scopece, A. J. Ferreri, M. G. Panucci, S. Monfardini and M. Ermani, *J Clin Oncol*, 2004, **22**, 1598-1604.
6. G. B. Zhang, S. Y. Huang and Z. C. Wang, *J Clin Neurosci*, 2012, **19**, 1636-1640.
7. J. J. Vredenburgh, A. Desjardins, D. A. Reardon and H. S. Friedman, *Neuro-Oncology*, 2009, **11**, 80-91.
8. H. S. Friedman, M. D. Prados, P. Y. Wen, T. Mikkelsen, D. Schiff, L. E. Abrey, W. K. A. Yung, N. Paleologos, M. K. Nicholas, R. Jensen, J. Vredenburgh, J. Huang, M. X. Zheng and T. Cloughesy, *J Clin Oncol*, 2009, **27**, 4733-4740.
9. G. M. Marx, N. Pavlakis, S. McCowatt, F. M. Boyle, J. A. Levi, D. R. Bell, R. Cook, M. Biggs, N. Little and H. R. Wheeler, *J Neuro-Oncol*, 2001, **54**, 31-38.
10. V. K. Puduvalli, P. Giglio, M. D. Groves, K. R. Hess, M. R. Gilbert, S. Mahankali, E. F. Jackson, V. A. Levin, C. A. Conrad, S. H. Hsu, H. Colman, J. F. de Groot, M. G. Ritterhouse, S. E. Ictech and W. K. A. Yung, *Neuro-Oncology*, 2008, **10**, 216-222.
11. M. R. Gilbert, J. J. Dignam, T. S. Armstrong, J. S. Wefel, D. T. Blumenthal, M. A. Vogelbaum, H. Colman, A. Chakravarti, S. Pugh, M. Won, R. Jeraj, P. D. Brown, K. A. Jaeckle, D. Schiff, V. W. Stieber, D. G. Brachman, M. Werner-Wasik, I. W. Tremont-Lukats, E. P. Sulman, K. D. Aldape, W. J. Curran and M. P. Mehta, *New Engl J Med*, 2014, **370**, 699-708.
12. O. L. Chinot, W. Wick, W. Mason, R. Henriksson, F. Saran, R. Nishikawa, A. F. Carpentier, K. Hoang-Xuan, P. Kavan, D. Cernea, A. A. Brandes, M. Hilton, L. Abrey and T. Cloughesy, *New Engl J Med*, 2014, **370**, 709-722.
13. R. Stupp, M. E. Hegi, W. P. Mason, M. J. van den Bent, M. J. B. Taphoorn, R. C. Janzer, S. K. Ludwin, A. Allgeier, B. Fisher, K. Belanger, P. Hau, A. A. Brandes, J. Gijtenbeek, C. Marosi, C. J. Vecht, K. Mokhtari, P. Wesseling, S. Villa, E. Eisenhauer, T. Gorlia, M. Weller, D. Lacombe, J. G. Cairncross, R. O. Mirimanoff, E. O. R. Treatment, C. B. T. Grp, R. O. Grp and N. C. I. C. C. Trials, *Lancet Oncol*, 2009, **10**, 459-466.
14. R. Stupp, W. P. Mason, M. J. van den Bent, M. Weller, B. Fisher, M. J. B. Taphoorn, K. Belanger, A. A. Brandes, C. Marosi, U. Bogdahn, J. Curschmann, R. C. Janzer, S. K. Ludwin, T. Gorlia, A. Allgeier, D. Lacombe, J. G. Cairncross, E. Eisenhauer, R. O. Mirimanoff, D. Van Den Weyngaert, S. Kaendler, P. Krauseneck, N. Vinolas, S. Villa, R. E. Wurm, M. H. B. Maillot, F. Spagnolli, G. Kantor, J. P. Malhaire, L. Renard, O. De Witte, L. Scandolaro, C. J. Vecht, P. Maingon, J. Lutterbach, A. Kobierska, M. Bolla, R. Souchon, C. Mitine, T. Tzuk-Shina, A. Kuten, G. Haferkamp, J. de Greve, F. Priou, J. Menten, I. Rutten, P. Clavere, A. Malmstrom, B. Jancar, E. Newlands, K. Pigott, A. Twijnstra, O. Chinot, M. Reni, A. Boiardi, M. Fabbro, M. Campone, J. Bozzino, M. Frenay, J. Gijtenbeek, A. A. Brandes, J. Y. Delattre, U. Bogdahn, U. De

Paula, M. J. van den Bent, C. Hanzen, G. Pavanato, S. Schraub, R. Pfeffer, R. Soffietti, M. Weller, R. D. Kortmann, M. Taphoorn, J. L. Torrecilla, C. Marosi, W. Grisold, P. Huget, P. Forsyth, D. Fulton, S. Kirby, R. Wong, D. Fenton, B. Fisher, G. Cairncross, P. Whitlock, K. Belanger, S. Burdette-Radoux, S. Gertler, S. Saunders, K. Laing, J. Siddiqui, L. A. Martin, S. Gulavita, J. Perry, W. Mason, B. Thiessen, H. Pai, Z. Y. Alam, D. Eisenstat, W. Mingrone, S. Hofer, G. Pesce, J. Curschmann, P. Y. Dietrich, R. Stupp, R. O. Mirimanoff, P. Thum, B. Baumert, G. Ryan and E. O. R. T. C. Br, *New Engl J Med*, 2005, **352**, 987-996.

15. N. J. Abbott, L. Ronnback and E. Hansson, *Nat Rev Neurosci*, 2006, **7**, 41-53.
16. R. K. Oberoi, K. E. Parrish, T. T. Sio, R. K. Mittapalli, W. F. Elmquist and J. N. Sarkaria, *Neuro-Oncology*, 2015, DOI: 10.1093/neuonc/nov164.
17. S. Bhaskar, F. Tian, T. Stoeger, W. Kreyling, J. M. de la Fuente, V. Grazu, P. Borm, G. Estrada, V. Ntziachristos and D. Razansky, *Particle and Fibre Toxicology*, 2010, **7**.
18. I. Wilhelm, C. Fazakas and I. A. Krizbai, *Acta Neurobiologiae Experimentalis*, 2011, **71**, 113-128.
19. H. Yang, *Pharmaceutical Research*, 2010, **27**, 1759-1771.
20. X. Y. Xu, X. F. Zhang, X. H. Wang, Y. X. Li and X. B. Jing, *Polym Advan Technol*, 2009, **20**, 843-848.
21. A. Zensi, D. Begley, C. Pontikis, C. Legros, L. Mihoreanu, C. Buechel and J. Kreuter, *Journal of Drug Targeting*, 2010, **18**, 842-848.
22. A. Zensi, D. Begley, C. Pontikis, C. Legros, L. Mihoreanu, S. Wagner, C. Buechel, H. von Briesen and J. Kreuter, *Journal of Controlled Release*, 2009, **137**, 78-86.
23. I. Miladi, G. Le Duc, D. Kryza, A. Berniard, P. Mowat, S. Roux, J. Taleb, P. Bonazza, P. Perriat, F. Lux, O. Tillement, C. Billotey and M. Janier, *J Biomater Appl*, 2013, **28**, 385-394.
24. N. T. Huynh, M. Morille, J. Bejaud, P. Legras, A. Vessieres, G. Jaouen, J. P. Benoit and C. Passirani, *Pharmaceutical Research*, 2011, **28**, 3189-3198.
25. S. C. J. Steiniger, J. Kreuter, A. S. Khalansky, I. N. Skidan, A. I. Bobruskin, Z. S. Smirnova, S. E. Severin, R. Uhl, M. Kock, K. D. Geiger and S. E. Gelperina, *Int J Cancer*, 2004, **109**, 759-767.
26. Y. Yamashita, R. Saito, M. T. Krauze, T. Kawaguchi, C. Noble, D. C. Drummond, D. B. Kirpotin, J. W. Park, M. S. Berger and K. S. Bankiewicz, *Target Oncol*, 2006, **1**, 79-85.
27. I. Brigger, J. Morizet, G. Aubert, H. Chacun, M. J. Terrier-Lacombe, P. Couvreur and G. Vassal, *J Pharmacol Exp Ther*, 2002, **303**, 928-936.
28. H. Cabral, Y. Matsumoto, K. Mizuno, Q. Chen, M. Murakami, M. Kimura, Y. Terada, M. R. Kano, K. Miyazono, M. Uesaka, N. Nishiyama and K. Kataoka, *Nature Nanotechnology*, 2011, **6**, 815-823.
29. M. Longmire, P. L. Choyke and H. Kobayashi, *Nanomedicine-Uk*, 2008, **3**, 703-717.
30. M. Horowitz, R. Blasberg, P. Molnar, J. Strong, P. Kornblith, R. Pleasants and J. Fenstermacher, *Cancer Res*, 1983, **43**, 3800-3807.
31. V. A. Levin, M. Freemandove and H. D. Landahl, *Arch Neurol-Chicago*, 1975, **32**, 785-791.
32. R. K. Oberoi, R. K. Mittapalli and W. F. Elmquist, *J Pharmacol Exp Ther*, 2013, **347**, 755-764.

33. S. K. Hobbs, W. L. Monsky, F. Yuan, W. G. Roberts, L. Griffith, V. P. Torchilin and R. K. Jain, *Proceedings of the National Academy of Sciences of the United States of America*, 1998, **95**, 4607-4612.
34. A. I. Minchinton and I. F. Tannock, *Nat Rev Cancer*, 2006, **6**, 583-592.
35. Z. Popovic, W. H. Liu, V. P. Chauhan, J. Lee, C. Wong, A. B. Greytak, N. Insin, D. G. Nocera, D. Fukumura, R. K. Jain and M. G. Bawendi, *Angew Chem Int Edit*, 2010, **49**, 8649-8652.
36. M. E. Fox, F. C. Szoka and J. M. J. Frechet, *Accounts Chem Res*, 2009, **42**, 1141-1151.
37. N. Nasongkla, B. Chen, N. Macaraeg, M. E. Fox, J. M. J. Frechet and F. C. Szoka, *J Am Chem Soc*, 2009, **131**, 3842-+.
38. H. L. Kim, S. B. Lee, H. J. Jeong and D. W. Kim, *Rsc Advances*, 2014, **4**, 31318-31322.
39. J. W. Seo, H. Zhang, D. L. Kukis, C. F. Meares and K. W. Ferrara, *Bioconjugate Chem.*, 2008, **19**, 2577-2584.
40. H. Dong, N. Dube, J. Y. Shu, J. W. Seo, L. M. Mahakian, K. W. Ferrara and T. Xu, *Acs Nano*, 2012, **6**, 5320-5329.
41. H. Dong, J. Y. Shu, N. Dube, Y. Ma, M. V. Tirrell, K. H. Downing and T. Xu, *J Am Chem Soc*, 2012, **134**, 11807-11814.
42. N. Dube, J. Y. Shu, H. Dong, J. W. Seo, E. Ingham, A. Kheirolomoom, P.-Y. Chen, J. Forsayeth, K. Bankiewicz, K. W. Ferrara and T. Xu, *Biomacromolecules*, 2013, **14**, 3697-3705.
43. N. Dube, J. W. Seo, H. Dong, J. Y. Shu, R. Lund, L. M. Mahakian, K. W. Ferrara and T. Xu, *Biomacromolecules*, 2014, **15**, 2963-2970.
44. H. Dong, R. Lund and T. Xu, *Biomacromolecules*, 2015, **16**, 743-747.
45. M. I. Koukourakis, S. Koukouraki, I. Fezoulidis, N. Kelekis, G. Kyrias, S. Archimandritis and N. Karkavitsas, *Brit J Cancer*, 2000, **83**, 1281-1286.
46. D. R. Senger, L. F. Brown, K. P. Claffey and H. F. Dvorak, *Invas Metast*, 1994, **14**, 385-394.
47. J. W. Seo, L. M. Mahakian, A. Kheirolomoom, H. Zhang, C. F. Meares, R. Ferdani, C. J. Anderson and K. W. Ferrara, *Bioconjugate Chem.*, 2010, **21**, 1206-1215.
48. E. T. M. Dams, P. Laverman, W. J. G. Oyen, G. Storm, G. L. Scherphof, J. W. M. Van der Meer, F. H. M. Corstens and O. C. Boerman, *J Pharmacol Exp Ther*, 2000, **292**, 1071-1079.
49. C. Engvall, E. Ryding, R. Wirestam, S. Holtas, K. Ljunggren, T. Ohlsson and P. Reinstrup, *J Neurosurg Anesth*, 2008, **20**, 41-44.
50. J. Dennie, J. B. Mandeville, J. L. Boxerman, S. D. Packard, B. R. Rosen and R. M. Weisskoff, *Magnet Reson Med*, 1998, **40**, 793-799.
51. C. Ricard, F. Stanchi, T. Rodriguez, M. C. Amoureux, G. Rougon and F. Debarbieux, *Plos One*, 2013, **8**, 15.
52. N. Nghi, J. Montagnese, L. R. Rogers, A. Sher and L. Wolansky, *Seminars in Roentgenology*, 2014, **49**, 275-289.
53. B. Ertl-Wagner, M. Ingrisch, M. Niyazi, O. Schnell, N. Jansen, S. Forster and C. la Fougere, *Radiologe*, 2013, **53**, 682-690.
54. H. B. Lee and M. D. Blaufox, *J Nucl Med*, 1985, **26**, 72-76.

Chapter 3

1. J. Andrew MacKay, M. Chen, J. R. McDaniel, W. Liu, A. J. Simnick and A. Chilkoti, *Nat. Mater.*, 2009, **8**, 993-999.
2. J. A. Hubbell, S. N. Thomas and M. A. Swartz, *Nature*, 2009, **462**, 449-460.
3. S. Kaida, H. Cabral, M. Kumagai, A. Kishimura, Y. Terada, M. Sekino, I. Aoki, N. Nishiyama, T. Tani and K. Kataoka, *Cancer Res.*, 2010, **70**, 7031-7041.
4. Z. Popović, W. Liu, V. P. Chauhan, J. Lee, C. Wong, A. B. Greytak, N. Insin, D. G. Nocera, D. Fukumura, R. K. Jain and M. G. Bawendi, *Angew. Chem., Int. Ed.*, 2010, **49**, 8649-8652.
5. N. Dube, J. W. Seo, H. Dong, J. Y. Shu, R. Lund, L. M. Mahakian, K. W. Ferrara and T. Xu, *Biomacromolecules*, 2014, **15**, 2963-2970.
6. H. Dong, J. Y. Shu, N. Dube, Y. Ma, M. V. Tirrell, K. H. Downing and T. Xu, *J. Am. Chem. Soc.*, 2012, **134**, 11807-11814.
7. H. Dong, R. Lund and T. Xu, *Biomacromolecules*, 2015, **16**, 743-747.
8. H. Dong, N. Dube, J. Y. Shu, J. W. Seo, L. M. Mahakian, K. W. Ferrara and T. Xu, *ACS Nano*, 2012, **6**, 5320-5329.
9. N. Dube, J. Y. Shu, H. Dong, J. W. Seo, E. Ingham, A. Kheirolomoom, P.-Y. Chen, J. Forsayeth, K. Bankiewicz, K. W. Ferrara and T. Xu, *Biomacromolecules*, 2013, **14**, 3697-3705.
10. J. W. Seo, J. Ang, L. M. Mahakian, S. Tam, B. Fite, E. S. Ingham, J. Beyer, J. Forsayeth, K. S. Bankiewicz, T. Xu and K. W. Ferrara, *J. Controlled Release*, 2015, **220, Part A**, 51-60.
11. *97th Edition*, 2016-2017, http://hbcponline.com/.
12. J. Y. Shu, R. Lund and T. Xu, *Biomacromolecules*, 2012, **13**, 1945-1955.
13. in *The MAK-Collection for Occupational Health and Safety*, Wiley-VCH Verlag GmbH & Co. KGaA, 2002, DOI: 10.1002/3527600418.mb2532268kske0010.
14. J. N. Israelachvili, D. J. Mitchell and B. W. Ninham, *J. Chem. Soc., Faraday Trans. 2*, 1976, **72**, 1525-1568.
15. C. Tanford, *The hydrophobic effect*, New York: John Wiley & Sons, 1980.
16. M. Kastantin, B. Ananthanarayanan, P. Karmali, E. Ruoslahti and M. Tirrell, *Langmuir*, 2009, **25**, 7279-7286.
17. N. L. Ogihara, M. S. Weiss, W. F. Degrado and D. Eisenberg, *Protein Sci.*, 1997, **6**, 80-88.
18. R. Lund, J. Shu and T. Xu, *Macromolecules*, 2013, **46**, 1625-1632.
19. J. M. Harris and R. B. Chess, *Nat. Rev. Drug Discovery*, 2003, **2**, 214-221.
20. F. M. Veronese and G. Pasut, *Drug Discovery Today*, 2005, **10**, 1451-1458.
21. O. Tirosh, Y. Barenholz, J. Katzhendler and A. Priev, *Biophys. J.*, 1998, **74**, 1371-1379.
22. Y. C. Liu, S. H. Chen and J. S. Huang, *Phys. Rev. E*, 1996, **54**, 1698-1708.
23. L. Derici, S. Ledger, S. M. Mai, C. Booth, I. W. Hamley and J. S. Pedersen, *Phys. Chem. Chem. Phys.*, 1999, **1**, 2773-2785.
24. Y. Liu, S.-H. Chen and J. S. Huang, *Macromolecules*, 1998, **31**, 2236-2244.
25. T. Li, K. Hong, L. Porcar, R. Verduzco, P. D. Butler, G. S. Smith, Y. Liu and W.-R. Chen, *Macromolecules*, 2008, **41**, 8916-8920.
26. T. Gillich, E. M. Benetti, E. Rakhmatullina, R. Konradi, W. Li, A. Zhang, A. D. Schlüter and M. Textor, *J. Am. Chem. Soc.*, 2011, **133**, 10940-10950.

27. X. Li, K. Hong, Y. Liu, C.-Y. Shew, E. Liu, K. W. Herwig, G. S. Smith, J. Zhao, G. Zhang, S. Pispas and W.-R. Chen, *J. Chem. Phys.*, 2010, **133**, 144912.
28. E. Hamed, T. Xu and S. Keten, *Biomacromolecules*, 2013, **14**, 4053-4060.
29. A. Jain and H. S. Ashbaugh, *Biomacromolecules*, 2011, **12**, 2729-2734.
30. K. Devanand and J. C. Selser, *Macromolecules*, 1991, **24**, 5943-5947.
31. C. J. Glinka, J. G. Barker, B. Hammouda, S. Krueger, J. J. Moyer and W. J. Orts, *J. Appl. Crystallogr.*, 1998, **31**, 430-445.
32. S. R. Kline, *J. Appl. Crystallogr.*, 2006, **39**, 895-900.
33. J. S. Pedersen, C. Svaneborg, K. Almdal, I. W. Hamley and R. N. Young, *Macromolecules*, 2003, **36**, 416-433.
34. G. Beaucage, *Journal of Applied Crystallography*, 1996, **29**, 134-146.
35. R. D. Groot and P. B. Warren, *J. Chem. Phys.*, 1997, **107**, 4423-4435.
36. R. D. Groot, *J. Chem. Phys.*, 2003, **118**, 11265-11277.
37. S. Plimpton, *J. Comput. Phys.*, 1995, **117**, 1-19.
38. M. Kranenburg and B. Smit, *J. Phys. Chem. B*, 2005, **109**, 6553-6563.
39. M. Venturoli, B. Smit and M. M. Sperotto, *Biophys. J.*, 2005, **88**, 1778-1798.
40. J.-H. Huang, Z.-X. Fan and Z.-X. Ma, *J. Chem. Phys.*, 2013, **139**, 064905.
41. Y. Li, M. Kroeger and W. K. Liu, *Biomaterials*, 2014, **35**, 8467-8478.
42. J. Y. Shu, C. Tan, W. F. DeGrado and T. Xu, *Biomacromolecules*, 2008, **9**, 2111-2117.
43. M. Pechar, P. Kopeckova, L. Joss and J. Kopecek, *Macromol. Biosci.*, 2002, **2**, 199-206.
44. E. Hamed, D. Ma and S. Keten, *BioNanoSci.*, 2015, **5**, 140-149.
45. D. R. Fattal and A. Benshaul, *Biophys. J.*, 1993, **65**, 1795-1809.
46. R. A. Friesner, R. B. Murphy, M. P. Repasky, L. L. Frye, J. R. Greenwood, T. A. Halgren, P. C. Sanschagrin and D. T. Mainz, *J. Med. Chem.*, 2006, **49**, 6177-6196.
47. H. Lee, A. H. de Vries, S.-J. Marrink and R. W. Pastor, *J. Phys. Chem. B*, 2009, **113**, 13186-13194.

Chapter 4

1. M. Mammen, S. K. Choi and G. M. Whitesides, *Angewandte Chemie-International Edition*, 1998, **37**, 2755-2794.
2. Y. C. Lee and R. T. Lee, *Acc. Chem. Res.*, 1995, **28**, 321-327.
3. G. Maheshwari, G. Brown, D. A. Lauffenburger, A. Wells and L. G. Griffith, *J. Cell Sci.*, 2000, **113**, 1677-1686.
4. J. J. Lundquist and E. J. Toone, *Chem. Rev.*, 2002, **102**, 555-578.
5. J. E. Gestwicki, C. W. Cairo, L. E. Strong, K. A. Oetjen and L. L. Kiessling, *J. Am. Chem. Soc.*, 2002, **124**, 14922-14933.
6. M. Arnold, E. A. Cavalcanti-Adam, R. Glass, J. Blummel, W. Eck, M. Kantlehner, H. Kessler and J. P. Spatz, *Chemphyschem*, 2004, **5**, 383-388.
7. C. Margadant, H. N. Monsuur, J. C. Norman and A. Sonnenberg, *Curr. Opin. Cell Biol.*, 2011, **23**, 607-614.
8. S. H. M. Sontjens, D. L. Nettles, M. A. Carnahan, L. A. Setton and M. W. Grinstaff, *Biomacromolecules*, 2006, **7**, 310-316.
9. M. S. Hahn, J. S. Miller and J. L. West, *Adv. Mater.*, 2006, **18**, 2679-2684.
10. N. J. Walters and E. Gentleman, *Acta Biomater.*, 2015, **11**, 3-16.
11. T. A. Petrie, J. E. Raynor, D. W. Dumbauld, T. T. Lee, S. Jagtap, K. L. Templeman, D. M. Collard and A. J. Garcia, *Sci. Transl. Med.*, 2010, **2**.
12. R. J. Seelbach, P. Fransen, M. Peroglio, D. Pulido, P. Lopez-Chicon, F. Duttenhoefer, S. Sauerbier, T. Freiman, P. Niemeyer, C. Semino, F. Albericio, M. Alini, M. Royo, A. Mata and D. Eglin, *Acta Biomater.*, 2014, **10**, 4340-4350.
13. Z. Poon, S. Chen, A. C. Engler, H.-i. Lee, E. Atas, G. von Maltzahn, S. N. Bhatia and P. T. Hammond, *Angew. Chem. Int. Ed.*, 2010, **49**, 7266-7270.
14. D. R. Elias, A. Poloukhtine, V. Popik and A. Tsourkas, *Nanomed. Nanotechnol. Biol. Med.*, 2013, **9**, 194-201.
15. B. P. Gray, S. Li and K. C. Brown, *Bioconjugate Chem.*, 2013, **24**, 85-96.
16. J. Y. Shu, C. Tan, W. F. DeGrado and T. Xu, *Biomacromolecules*, 2008, **9**, 2111-2117.
17. T. Xu and J. Shu, *Soft Matter*, 2010, **6**, 212-217.
18. J. Y. Shu, R. Lund and T. Xu, *Biomacromolecules*, 2012, **13**, 1945-1955.
19. H. Dong, N. Dube, J. Y. Shu, J. W. Seo, L. M. Mahakian, K. W. Ferrara and T. Xu, *ACS Nano*, 2012, **6**, 5320-5329.
20. H. Dong, J. Y. Shu, N. Dube, Y. Ma, M. V. Tirrell, K. H. Downing and T. Xu, *J. Am. Chem. Soc.*, 2012, **134**, 11807-11814.
21. R. Lund, J. Shu and T. Xu, *Macromolecules*, 2013, **46**, 1625-1632.
22. N. Dube, J. Y. Shu, H. Dong, J. W. Seo, E. Ingham, A. Kheirolomoom, P.-Y. Chen, J. Forsayeth, K. Bankiewicz, K. W. Ferrara and T. Xu, *Biomacromolecules*, 2013, **14**, 3697-3705.
23. N. Dube, J. W. Seo, H. Dong, J. Y. Shu, R. Lund, L. M. Mahakian, K. W. Ferrara and T. Xu, *Biomacromolecules*, 2014, **15**, 2963-2970.
24. H. Dong, R. Lund and T. Xu, *Biomacromolecules*, 2015, **16**, 743-747.
25. J. W. Seo, J. Ang, L. M. Mahakian, S. Tam, B. Fite, E. S. Ingham, J. Beyer, J. Forsayeth, K. S. Bankiewicz, T. Xu and K. W. Ferrara, *J. Controlled Release*, 2015, **220, Part A**, 51-60.
26. J. Ang, D. Ma, R. Lund, S. Keten and T. Xu, *Biomacromolecules*, 2016, **17**, 3262-3267.

27. T. J. Graddis, D. G. Myszka and I. M. Chaiken, *Biochemistry*, 1993, **32**, 12664-12671.
28. H. Sakamoto, M. S. Lewis, H. Kodama, E. Appella and K. Sakaguchi, *Proc. Natl. Acad. Sci. U.S.A.*, 1994, **91**, 8974-8978.
29. G. W. M. Vandermeulen, C. Tziatzios and H. A. Klok, *Macromolecules*, 2003, **36**, 4107-4114.
30. G. W. M. Vandermeulen, C. Tziatzios, R. Duncan and H.-A. Klok, *Macromolecules*, 2005, **38**, 761-769.
31. L. Malik, J. Nygaard, N. J. Christensen, W. W. Streicher, P. W. Thulstrup, L. Arleth and K. J. Jensen, *J. Pept. Sci.*, 2013, **19**, 283-292.
32. D. A. D. Parry, R. D. B. Fraser and J. M. Squire, *J. Struct. Biol.*, 2008, **163**, 258-269.
33. P. Dutta, J. B. Peng, B. Lin, J. B. Ketterson, M. Prakash, P. Georgopoulos and S. Ehrlich, *Phys. Rev. Lett.*, 1987, **58**, 2228-2231.
34. K. Kjaer, J. Als-Nielsen, C. A. Helm, L. A. Laxhuber and H. Mohwald, *Phys. Rev. Lett.*, 1987, **58**, 2224-2227.
35. I. Langmuir, *J. Am. Chem. Soc.*, 1917, **39**, 1848-1906.
36. L. Bosio, J. J. Benattar and F. Rieutord, *Revue De Physique Appliquee*, 1987, **22**, 775-778.
37. M. J. Grundy, R. M. Richardson, S. J. Roser, J. Penfold and R. C. Ward, *Thin Solid Films*, 1988, **159**, 43-52.
38. B. Lin, M. C. Shih, T. M. Bohanon, G. E. Ice and P. Dutta, *Phys. Rev. Lett.*, 1990, **65**, 191-194.
39. D. Jacquemain, S. G. Wolf, F. Leveiller, M. Deutsch, K. Kjaer, J. Alsnielsen, M. Lahav and L. Leiserowitz, *Angewandte Chemie-International Edition in English*, 1992, **31**, 130-152.
40. M. K. Durbin, A. Malik, R. Ghaskadvi, M. C. Shih, P. Zschack and P. Dutta, *The Journal of Physical Chemistry*, 1994, **98**, 1753-1755.
41. W. J. Foster, M. C. Shih and P. S. Pershan, *The Journal of Chemical Physics*, 1996, **105**, 3307-3315.
42. S. Ye, B. M. Discher, J. Strzalka, T. Xu, S. P. Wu, D. Noy, I. Kuzmenko, T. Gog, M. J. Therien, P. L. Dutton and J. K. Blasie, *Nano Lett.*, 2005, **5**, 1658-1667.
43. J. Strzalka, T. Xu, A. Tronin, S. P. Wu, I. Miloradovic, I. Kuzmenko, T. Gog, M. J. Therien and J. K. Blasie, *Nano Lett.*, 2006, **6**, 2395-2405.
44. V. Krishnan, A. Tronin, J. Strzalka, H. C. Fry, M. J. Therien and J. K. Blasie, *J. Am. Chem. Soc.*, 2010, **132**, 11083-11092.
45. J. Strzalka, X. Chen, C. C. Moser, P. L. Dutton, B. M. Ocko and J. K. Blasie, *Langmuir*, 2000, **16**, 10404-10418.
46. D. H. Atha and K. C. Ingham, *J. Biol. Chem.*, 1981, **256**, 2108-2117.
47. G. Maisano, D. Majolino, P. Migliardo, S. Venuto, F. Aliotta and S. Magazu, *Mol. Phys.*, 1993, **78**, 421-435.
48. N. Chaudhary and R. Nagaraj, *J. Colloid Interface Sci.*, 2011, **360**, 139-147.
49. A. Trovato, T. X. Hoang, J. R. Banavar and A. Maritan, *Proceedings of the National Academy of Sciences*, 2007, **104**, 19187-19192.
50. Z. Li, M. W. Zhao, J. Quinn, M. H. Rafailovich, J. Sokolov, R. B. Lennox, A. Eisenberg, X. Z. Wu, M. W. Kim, S. K. Sinha and M. Tolan, *Langmuir*, 1995, **11**, 4785-4792.

51. R. K. Thomas and J. Penfold, *Current Opinion in Colloid & Interface Science*, 1996, **1**, 23-33.
52. S. W. An, R. K. Thomas, F. L. Baines, N. C. Billingham, S. P. Armes and J. Penfold, *Macromolecules*, 1998, **31**, 7877-7885.
53. M. C. Faure, P. Bassereau, L. T. Lee, A. Menelle and C. Lheveder, *Macromolecules*, 1999, **32**, 8538-8550.
54. A. Top, C. J. Roberts and K. L. Kiick, *Biomacromolecules*, 2011, **12**, 2184-2192.
55. N. Tzokova, C. M. Fernyhough, P. D. Topham, N. Sandon, D. J. Adams, M. F. Butler, S. P. Armes and A. J. Ryan, *Langmuir*, 2009, **25**, 2479-2485.
56. N. Tzokova, C. M. Fernyhough, M. F. Butler, S. P. Armes, A. J. Ryan, P. D. Topham and D. J. Adams, *Langmuir*, 2009, **25**, 11082-11089.
57. B. Lin, M. Meron, J. Gebhardt, T. Graber, M. L. Schlossman and P. J. Viccaro, *Physica B: Condensed Matter*, 2003, **336**, 75-80.
58. S. M. Danauskas, D. Li, M. Meron, B. Lin and K. Y. C. Lee, *J. Appl. Crystallogr.*, 2008, **41**, 1187-1193.

Chapter 5

1. Whitesides, G. M.; Boncheva, M., Beyond molecules: Self-assembly of mesoscopic and macroscopic components. *Proceedings of the National Academy of Sciences of the United States of America* **2002,** 99, (8), 4769-4774.
2. Zhang, S. G., Fabrication of novel biomaterials through molecular self-assembly. *Nature Biotechnology* **2003,** 21, (10), 1171-1178.
3. Palmer, L. C.; Stupp, S. I., Molecular Self-Assembly into One-Dimensional Nanostructures. *Accounts of Chemical Research* **2008,** 41, (12), 1674-1684.
4. Paramonov, S. E.; Jun, H. W.; Hartgerink, J. D., Self-assembly of peptide-amphiphile nanofibers: The roles of hydrogen bonding and amphiphilic packing. *Journal of the American Chemical Society* **2006,** 128, (22), 7291-7298.
5. Dong, H.; Paramonov, S. E.; Aulisa, L.; Bakota, E. L.; Hartgerink, J. D., Self-Assembly of Multidomain Peptides: Balancing Molecular Frustration Controls Conformation and Nanostructure. *Journal of the American Chemical Society* **2007,** 129, (41), 12468-12472.
6. Cui, H. G.; Chen, Z. Y.; Zhong, S.; Wooley, K. L.; Pochan, D. J., Block copolymer assembly via kinetic control. *Science* **2007,** 317, (5838), 647-650.
7. Versluis, F.; Marsden, H. R.; Kros, A., Power struggles in peptide-amphiphile nanostructures. *Chemical Society Reviews* **2010,** 39, (9), 3434-3444.
8. Hayward, R. C.; Pochan, D. J., Tailored Assemblies of Block Copolymers in Solution: It Is All about the Process. *Macromolecules* **2010,** 43, (8), 3577-3584.
9. O'Leary, L. E. R.; Fallas, J. A.; Bakota, E. L.; Kang, M. K.; Hartgerink, J. D., Multi-hierarchical self-assembly of a collagen mimetic peptide from triple helix to nanofibre and hydrogel. *Nature Chemistry* **2011,** 3, (10), 821-828.
10. Hamley, I. W.; Castelletto, V., Self-Assembly of Peptide Bioconjugates: Selected Recent Research Highlights. *Bioconjugate Chemistry* **2016**.
11. Whitesides, G. M.; Grzybowski, B., Self-assembly at all scales. *Science* **2002,** 295, (5564), 2418-2421.
12. Checot, F.; Lecommandoux, S.; Gnanou, Y.; Klok, H. A., Water-soluble stimuli-responsive vesicles from peptide-based diblock copolymers. *Angewandte Chemie-International Edition* **2002,** 41, (8), 1339-1343.
13. Colfen, H.; Mann, S., Higher-order organization by mesoscale self-assembly and transformation of hybrid nanostructures. *Angewandte Chemie-International Edition* **2003,** 42, (21), 2350-2365.
14. Haines-Butterick, L.; Rajagopal, K.; Branco, M.; Salick, D.; Rughani, R.; Pilarz, M.; Lamm, M. S.; Pochan, D. J.; Schneider, J. P., Controlling hydrogelation kinetics by peptide design for three-dimensional encapsulation and injectable delivery of cells. *Proceedings of the National Academy of Sciences of the United States of America* **2007,** 104, (19), 7791-7796.
15. Carlsen, A.; Lecommandoux, S., Self-assembly of polypeptide-based block copolymer amphiphiles. *Current Opinion in Colloid & Interface Science* **2009,** 14, (5), 329-339.
16. Zhu, J. H.; Zhang, S. Y.; Zhang, F. W.; Wooley, K. L.; Pochan, D. J., Hierarchical Assembly of Complex Block Copolymer Nanoparticles into Multicompartment Superstructures through Tunable Interparticle Associations. *Advanced Functional Materials* **2013,** 23, (14), 1767-1773.

17. Tantakitti, F.; Boekhoven, J.; Wang, X.; Kazantsev, R. V.; Yu, T.; Li, J. H.; Zhuang, E.; Zandi, R.; Ortony, J. H.; Newcomb, C. J.; Palmer, L. C.; Shekhawat, G. S.; de la Cruz, M. O.; Schatz, G. C.; Stupp, S. I., Energy landscapes and functions of supramolecular systems. *Nature Materials* **2016,** 15, (4), 469-+.
18. Whitesides, G. M., The 'right' size in nanobiotechnology. *Nat Biotech* **2003,** 21, (10), 1161-1165.
19. Salata, O. V., Applications of nanoparticles in biology and medicine. *Journal of Nanobiotechnology* **2004,** 2, 3-3.
20. Cabral, H.; Matsumoto, Y.; Mizuno, K.; Chen, Q.; Murakami, M.; Kimura, M.; Terada, Y.; Kano, M. R.; Miyazono, K.; Uesaka, M.; Nishiyama, N.; Kataoka, K., Accumulation of sub-100 nm polymeric micelles in poorly permeable tumours depends on size. *Nature Nanotechnology* **2011,** 6, (12), 815-823.
21. Albanese, A.; Tang, P. S.; Chan, W. C. W., The Effect of Nanoparticle Size, Shape, and Surface Chemistry on Biological Systems. In *Annual Review of Biomedical Engineering, Vol 14*, Yarmush, M. L., Ed. 2012; Vol. 14, pp 1-16.
22. Moghimi, S. M.; Hunter, A. C.; Andresen, T. L., Factors Controlling Nanoparticle Pharmacokinetics: An Integrated Analysis and Perspective. In *Annual Review of Pharmacology and Toxicology, Vol 52*, Insel, P. A.; Amara, S. G.; Blaschke, T. F., Eds. 2012; Vol. 52, pp 481-503.
23. Barua, S.; Mitragotri, S., Challenges associated with penetration of nanoparticles across cell and tissue barriers: A review of current status and future prospects. *Nano Today* **2014,** 9, (2), 223-243.
24. Dong, H.; Dube, N.; Shu, J. Y.; Seo, J. W.; Mahakian, L. M.; Ferrara, K. W.; Xu, T., Long-Circulating 15 nm Micelles Based on Amphiphilic 3-Helix Peptide–PEG Conjugates. *ACS Nano* **2012,** 6, (6), 5320-5329.
25. Dong, H.; Shu, J. Y.; Dube, N.; Ma, Y.; Tirrell, M. V.; Downing, K. H.; Xu, T., 3-Helix Micelles Stabilized by Polymer Springs. *Journal of the American Chemical Society* **2012,** 134, (28), 11807-11814.
26. Dube, N.; Shu, J. Y.; Dong, H.; Seo, J. W.; Ingham, E.; Kheirolomoom, A.; Chen, P.-Y.; Forsayeth, J.; Bankiewicz, K.; Ferrara, K. W.; Xu, T., Evaluation of Doxorubicin-Loaded 3-Helix Micelles as Nanocarriers. *Biomacromolecules* **2013,** 14, (10), 3697-3705.
27. Dube, N.; Seo, J. W.; Dong, H.; Shu, J. Y.; Lund, R.; Mahakian, L. M.; Ferrara, K. W.; Xu, T., Effect of Alkyl Length of Peptide–Polymer Amphiphile on Cargo Encapsulation Stability and Pharmacokinetics of 3-Helix Micelles. *Biomacromolecules* **2014,** 15, (8), 2963-2970.
28. Dong, H.; Lund, R.; Xu, T., Micelle Stabilization via Entropic Repulsion: Balance of Force Directionality and Geometric Packing of Subunit. *Biomacromolecules* **2015,** 16, (3), 743-747.
29. Ang, J.; Ma, D.; Lund, R.; Keten, S.; Xu, T., Internal Structure of 15 nm 3-Helix Micelle Revealed by Small-Angle Neutron Scattering and Coarse-Grained MD Simulation. *Biomacromolecules* **2016,** 17, (10), 3262-3267.
30. Wohlfart, S.; Gelperina, S.; Kreuter, J., Transport of drugs across the blood-brain barrier by nanoparticles. *Journal of controlled release : official journal of the Controlled Release Society* **2012,** 161, (2), 264-73.

31. Seo, J. W.; Ang, J.; Mahakian, L. M.; Tam, S.; Fite, B.; Ingham, E. S.; Beyer, J.; Forsayeth, J.; Bankiewicz, K. S.; Xu, T.; Ferrara, K. W., Self-assembled 20-nm 64Cu-micelles enhance accumulation in rat glioblastoma. *Journal of Controlled Release* **2015,** 220, Part A, 51-60.
32. Salegio, E.; Streeter, H.; Dube, N.; Hadaczek, P.; Samaranch, L.; Kells, A.; San Sebastián, W.; Zhai, Y.; Bringas, J.; Xu, T.; Forsayeth, J.; Bankiewicz, K., Distribution of nanoparticles throughout the cerebral cortex of rodents and non-human primates: Implications for gene and drug therapy. *Frontiers in Neuroanatomy* **2014,** 8, (9).
33. Hamed, E.; Xu, T.; Keten, S., Poly(ethylene glycol) Conjugation Stabilizes the Secondary Structure of alpha-Helices by Reducing Peptide Solvent Accessible Surface Area. *Biomacromolecules* **2013,** 14, (11), 4053-4060.
34. Hamley, I. W., PEG–Peptide Conjugates. *Biomacromolecules* **2014,** 15, (5), 1543-1559.
35. Kastantin, M.; Ananthanarayanan, B.; Karmali, P.; Ruoslahti, E.; Tirrell, M., Effect of the Lipid Chain Melting Transition on the Stability of DSPE-PEG(2000) Micelles. *Langmuir* **2009,** 25, (13), 7279-7286.
36. Glavas, L.; Olsén, P.; Odelius, K.; Albertsson, A.-C., Achieving Micelle Control through Core Crystallinity. *Biomacromolecules* **2013,** 14, (11), 4150-4156.
37. Zinn, T.; Willner, L.; Lund, R., Nanoscopic Confinement through Self-Assembly: Crystallization within Micellar Cores Exhibits Simple Gibbs-Thomson Behavior. *Physical Review Letters* **2014,** 113, (23).
38. Wu, P. G.; Brand, L., Resonance Energy Transfer: Methods and Applications. *Analytical Biochemistry* **1994,** 218, (1), 1-13.
39. Shu, J. Y.; Lund, R.; Xu, T., Solution Structural Characterization of Coiled-Coil Peptide–Polymer Side-Conjugates. *Biomacromolecules* **2012,** 13, (6), 1945-1955.
40. Lund, R.; Ang, J.; Shu, J. Y.; Xu, T., Understanding Peptide Oligomeric State in Langmuir Monolayers of Amphiphilic 3-Helix Bundle-forming Peptide-PEG Conjugates. *Biomacromolecules* **2016**.
41. Thomas, F.; Boyle, A. L.; Burton, A. J.; Woolfson, D. N., A Set of de Novo Designed Parallel Heterodimeric Coiled Coils with Quantified Dissociation Constants in the Micromolar to Sub-nanomolar Regime. *Journal of the American Chemical Society* **2013,** 135, (13), 5161-5166.
42. Boice, J. A.; Dieckmann, G. R.; DeGrado, W. F.; Fairman, R., Thermodynamic analysis of a designed three-stranded coiled coil. *Biochemistry* **1996,** 35, (46), 14480-14485.
43. Won, Y.-Y.; Davis, H. T.; Bates, F. S., Molecular Exchange in PEO−PB Micelles in Water. *Macromolecules* **2003,** 36, (3), 953-955.
44. Lund, R.; Willner, L.; Richter, D.; Dormidontova, E. E., Equilibrium Chain Exchange Kinetics of Diblock Copolymer Micelles: Tuning and Logarithmic Relaxation. *Macromolecules* **2006,** 39, (13), 4566-4575.
45. Rosu, F.; Gabelica, V.; Poncelet, H.; De Pauw, E., Tetramolecular G-quadruplex formation pathways studied by electrospray mass spectrometry. *Nucleic Acids Research* **2010,** 38, (15), 5217-5225.
46. Rikken, R. S. M.; Engelkamp, H.; Nolte, R. J. M.; Maan, J. C.; van Hest, J. C. M.; Wilson, D. A.; Christianen, P. C. M., Shaping polymersomes into predictable morphologies via out-of-equilibrium self-assembly. *Nature Communications* **2016,** 7.

47. Laflèche, F.; Nicolai, T.; Durand, D.; Gnanou, Y.; Taton, D., Association of Adhesive Spheres Formed by Hydrophobically End-Capped PEO. 2. Influence of the Alkyl End-Group Length and the Chain Backbone Architecture. *Macromolecules* **2003,** 36, (4), 1341-1348.
48. Zinn, T.; Willner, L.; Pipich, V.; Richter, D.; Lund, R., Effect of Core Crystallization and Conformational Entropy on the Molecular Exchange Kinetics of Polymeric Micelles. *ACS Macro Letters* **2015,** 4, (6), 651-655.
49. Zinn, T.; Willner, L.; Pipich, V.; Richter, D.; Lund, R., Molecular Exchange Kinetics of Micelles: Corona Chain Length Dependence. *ACS Macro Letters* **2016,** 5, (7), 884-888.
50. Chen, Y.-H.; Yang, J. T.; Chau, K. H., Determination of the helix and β form of proteins in aqueous solution by circular dichroism. *Biochemistry* **1974,** 13, (16), 3350-3359.
51. Forood, B.; Feliciano, E. J.; Nambiar, K. P., Stabilization of alpha-helical structures in short peptides via end capping. *Proceedings of the National Academy of Sciences of the United States of America* **1993,** 90, (3), 838-42.
52. Su, J. Y.; Hodges, R. S.; Kay, C. M., Effect of Chain Length on the Formation and Stability of Synthetic .alpha.-Helical Coiled Coils. *Biochemistry* **1994,** 33, (51), 15501-15510.

Chapter 6

1. Y. Matsumura and H. Maeda, *Cancer Research*, 1986, **46**, 6387-6392.
2. U. Prabhakar, H. Maeda, R. K. Jain, E. M. Sevick-Muraca, W. Zamboni, O. C. Farokhzad, S. T. Barry, A. Gabizon, P. Grodzinski and D. C. Blakey, *Cancer Research*, 2013, **73**, 2412-2417.
3. N. Kottari, Y. M. Chabre, R. Sharma and R. Roy, in *Multifaceted Development and Application of Biopolymers for Biology, Biomedicine and Nanotechnology*, eds. P. K. Dutta and J. Dutta, Springer Berlin Heidelberg, Berlin, Heidelberg, 2013, DOI: 10.1007/12_2012_208, pp. 297-341.
4. C. Mamot, D. C. Drummond, U. Greiser, K. Hong, D. B. Kirpotin, J. D. Marks and J. W. Park, *Cancer Res*, 2003, **63**, 3154-3161.
5. H. S. Yoo and T. G. Park, *Journal of Controlled Release*, 2004, **100**, 247-256.
6. P. J. Stevens, M. Sekido and R. J. Lee, *Pharmaceutical research*, 2004, **21**, 2153-2157.
7. P. Kocbek, N. Obermajer, M. Cegnar, J. Kos and J. Kristl, *Journal of controlled release : official journal of the Controlled Release Society*, 2007, **120**, 18-26.
8. N. Nasongkla, X. Shuai, H. Ai, B. D. Weinberg, J. Pink, D. A. Boothman and J. Gao, *Angewandte Chemie International Edition*, 2004, **43**, 6323-6327.
9. P. Hölig, M. Bach, T. Völkel, T. Nahde, S. Hoffmann, R. Müller and R. E. Kontermann, *Protein Engineering Design and Selection*, 2004, **17**, 433-441.
10. Y. H. Bae, *Journal of Controlled Release*, 2009, **133**, 2-3.
11. T. M. Allen, C. Hansen, F. Martin, C. Redemann and A. Yau-Young, *Biochimica et biophysica acta*, 1991, **1066**, 29-36.
12. D. Papahadjopoulos, T. M. Allen, A. Gabizon, E. Mayhew, K. Matthay, S. K. Huang, K. D. Lee, M. C. Woodle, D. D. Lasic and C. Redemann, *Proceedings of the National Academy of Sciences*, 1991, **88**, 11460-11464.
13. F. Yuan, M. Leunig, S. K. Huang, D. A. Berk, D. Papahadjopoulos and R. K. Jain, *Cancer Research*, 1994, **54**, 3352-3356.
14. J. A. MacKay, M. N. Chen, J. R. McDaniel, W. G. Liu, A. J. Simnick and A. Chilkoti, *Nature Materials*, 2009, **8**, 993-999.
15. V. Percec, D. A. Wilson, P. Leowanawat, C. J. Wilson, A. D. Hughes, M. S. Kaucher, D. A. Hammer, D. H. Levine, A. J. Kim, F. S. Bates, K. P. Davis, T. P. Lodge, M. L. Klein, R. H. DeVane, E. Aqad, B. M. Rosen, A. O. Argintaru, M. J. Sienkowska, K. Rissanen, S. Nummelin and J. Ropponen, *Science*, 2010, **328**, 1009-1014.
16. J. N. Israelachvili, D. J. Mitchell and B. W. Ninham, *Journal of the Chemical Society, Faraday Transactions 2: Molecular and Chemical Physics*, 1976, **72**, 1525-1568.
17. Y. C. Yu, P. Berndt, M. Tirrell and G. B. Fields, *Journal of the American Chemical Society*, 1996, **118**, 12515-12520.
18. L. A. Koutsky , K. A. Ault , C. M. Wheeler , D. R. Brown , E. Barr , F. B. Alvarez , L. M. Chiacchierini and K. U. Jansen *New England Journal of Medicine*, 2002, **347**, 1645-1651.
19. T. L. Schlick, Z. Ding, E. W. Kovacs and M. B. Francis, *Journal of the American Chemical Society*, 2005, **127**, 3718-3723.
20. R. K. Iha, K. L. Wooley, A. M. Nystrom, D. J. Burke, M. J. Kade and C. J. Hawker, *Chemical reviews*, 2009, **109**, 5620-5686.

21. M. Mammen, S.-K. Choi and G. M. Whitesides, *Angewandte Chemie International Edition*, 1998, **37**, 2754-2794.
22. J. H. Rao, J. Lahiri, L. Isaacs, R. M. Weis and G. M. Whitesides, *Science*, 1998, **280**, 708-711.
23. T. Christensen, D. M. Gooden, J. E. Kung and E. J. Toone, *Journal of the American Chemical Society*, 2003, **125**, 7357-7366.
24. P. I. Kitov and D. R. Bundle, *Journal of the American Chemical Society*, 2003, **125**, 16271-16284.
25. X. Montet, M. Funovics, K. Montet-Abou, R. Weissleder and L. Josephson, *Journal of Medicinal Chemistry*, 2006, **49**, 6087-6093.
26. S. Hong, P. R. Leroueil, I. J. Majoros, B. G. Orr, J. R. Baker Jr and M. M. Banaszak Holl, *Chemistry & Biology*, 2007, **14**, 107-115.
27. H. Dong, J. Y. Shu, N. Dube, Y. Ma, M. V. Tirrell, K. H. Downing and T. Xu, *Journal of the American Chemical Society*, 2012, **134**, 11807-11814.
28. H. Dong, N. Dube, J. Y. Shu, J. W. Seo, L. M. Mahakian, K. W. Ferrara and T. Xu, *ACS Nano*, 2012, **6**, 5320-5329.
29. N. Dube, J. Y. Shu, H. Dong, J. W. Seo, E. Ingham, A. Kheirolomoom, P.-Y. Chen, J. Forsayeth, K. Bankiewicz, K. W. Ferrara and T. Xu, *Biomacromolecules*, 2013, **14**, 3697-3705.
30. N. Dube, J. W. Seo, H. Dong, J. Y. Shu, R. Lund, L. M. Mahakian, K. W. Ferrara and T. Xu, *Biomacromolecules*, 2014, **15**, 2963-2970.
31. H. Dong, R. Lund and T. Xu, *Biomacromolecules*, 2015, **16**, 743-747.
32. J. W. Seo, J. Ang, L. M. Mahakian, S. Tam, B. Fite, E. S. Ingham, J. Beyer, J. Forsayeth, K. S. Bankiewicz, T. Xu and K. W. Ferrara, *Journal of Controlled Release*, 2015, **220, Part A**, 51-60.
33. J. Ang, D. Ma, R. Lund, S. Keten and T. Xu, *Biomacromolecules*, 2016, **17**, 3262-3267.
34. T. Kinashi, *Nature Reviews Immunology*, 2005, **5**, 546-559.
35. S. J. Shattil, C. Kim and M. H. Ginsberg, *Nature Reviews Molecular Cell Biology*, 2010, **11**, 288-300.
36. C. Margadant, H. N. Monsuur, J. C. Norman and A. Sonnenberg, *Current Opinion in Cell Biology*, 2011, **23**, 607-614.
37. A. W. Reinke, R. A. Grant and A. E. Keating, *Journal of the American Chemical Society*, 2010, **132**, 6025-6031.
38. L. Jiang, D. Xu, K. E. Namitz, M. S. Cosgrove, R. Lund and H. Dong, *Small (Weinheim an der Bergstrasse, Germany)*, 2016, **12**, 5126-5131.
39. J. M. Fletcher, R. L. Harniman, F. R. Barnes, A. L. Boyle, A. Collins, J. Mantell, T. H. Sharp, M. Antognozzi, P. J. Booth, N. Linden, M. J. Miles, R. B. Sessions, P. Verkade and D. N. Woolfson, *Science*, 2013, **340**, 595-599.
40. H. Gradišar, S. Božič, T. Doles, D. Vengust, I. Hafner-Bratkovič, A. Mertelj, B. Webb, A. Šali, S. Klavžar and R. Jerala, *Nat Chem Biol*, 2013, **9**, 362-366.
41. A. B. E. Attia, Z. Y. Ong, J. L. Hedrick, P. P. Lee, P. L. R. Ee, P. T. Hammond and Y.-Y. Yang, *Current Opinion in Colloid & Interface Science*, 2011, **16**, 182-194.
42. D. J. Lunn, J. R. Finnegan and I. Manners, *Chemical Science*, 2015, **6**, 3663-3673.
43. Z. Poon, S. Chen, A. C. Engler, H. I. Lee, E. Atas, G. von Maltzahn, S. N. Bhatia and P. T. Hammond, *Angewandte Chemie-International Edition*, 2010, **49**, 7266-7270.

44. Z. Poon, J. A. Lee, S. W. Huang, R. J. Prevost and P. T. Hammond, *Nanomedicine-Nanotechnology Biology and Medicine*, 2011, **7**, 201-209.
45. H. B. Qiu, Y. Gao, C. E. Boott, O. E. C. Gould, R. L. Harniman, M. J. Miles, S. E. D. Webb, M. A. Winnik and I. Manners, *Science*, 2016, **352**, 697-701.
46. A. H. Groschel, A. Walther, T. I. Lobling, F. H. Schacher, H. Schmalz and A. H. E. Muller, *Nature*, 2013, **503**, 247-+.
47. A. H. Groschel, F. H. Schacher, H. Schmalz, O. V. Borisov, E. B. Zhulina, A. Walther and A. H. E. Muller, *Nature Communications*, 2012, **3**.
48. Z. Li, E. Kesselman, Y. Talmon, M. A. Hillmyer and T. P. Lodge, *Science*, 2004, **306**, 98-101.
49. H. Cui, Z. Chen, S. Zhong, K. L. Wooley and D. J. Pochan, *Science*, 2007, **317**, 647-650.
50. G. Srinivas and J. W. Pitera, *Nano Letters*, 2008, **8**, 611-618.
51. X. G. Ye, Z. W. Li, Z. Y. Sun and B. Khomami, *Acs Nano*, 2016, **10**, 5199-5203.
52. C. LoPresti, M. Massignani, C. Fernyhough, A. Blanazs, A. J. Ryan, J. Madsen, N. J. Warren, S. P. Armes, A. L. Lewis, S. Chirasatitsin, A. J. Engler and G. Battaglia, *Acs Nano*, 2011, **5**, 1775-1784.
53. D. J. Kraft, R. Ni, F. Smallenburg, M. Hermes, K. Yoon, D. A. Weitz, A. van Blaaderen, J. Groenewold, M. Dijkstra and W. K. Kegel, *Proceedings of the National Academy of Sciences of the United States of America*, 2012, **109**, 10787-10792.
54. Y. Kashcooli, K. Park, A. Bose, M. Greenfield and G. D. Bothun, *Biomacromolecules*, 2016, DOI: 10.1021/acs.biomac.6b01467.
55. A. M. Jackson, J. W. Myerson and F. Stellacci, *Nature Materials*, 2004, **3**, 330-336.
56. I. C. Pons-Siepermann and S. C. Glotzer, *Acs Nano*, 2012, **6**, 3919-3924.
57. A. Santos, J. A. Millan and S. C. Glotzer, *Nanoscale*, 2012, **4**, 2640-2650.
58. T. M. Hermans, M. A. C. Broeren, N. Gomopoulos, P. van der Schoot, M. H. P. van Genderen, N. Sommerdijk, G. Fytas and E. W. Meijer, *Nature Nanotechnology*, 2009, **4**, 721-726.
59. Y. F. Wang, A. D. Hollingsworth, S. K. Yang, S. Patel, D. J. Pine and M. Weck, *Journal of the American Chemical Society*, 2013, **135**, 14064-14067.
60. R. M. Choueiri, E. Galati, H. Thérien-Aubin, A. Klinkova, E. M. Larin, A. Querejeta-Fernández, L. Han, H. L. Xin, O. Gang, E. B. Zhulina, M. Rubinstein and E. Kumacheva, *Nature*, 2016, **538**, 79-83.
61. D. E. Robertson, R. S. Farid, C. C. Moser, J. L. Urbauer, S. E. Mulholland, R. Pidikiti, J. D. Lear, A. J. Wand, W. F. Degrado and P. L. Dutton, *Nature*, 1994, **368**, 425-431.
62. B. R. Gibney and P. L. Dutton, *Protein Science*, 1999, **8**, 1888-1898.
63. A. D. Presley, J. J. Chang and T. Xu, *Soft Matter*, 2011, **7**, 172-179.
64. R. Lund, J. Ang, J. Y. Shu and T. Xu, *Biomacromolecules*, 2016, DOI: 10.1021/acs.biomac.6b01356.
65. J. Y. Shu, C. Tan, W. F. DeGrado and T. Xu, *Biomacromolecules*, 2008, **9**, 2111-2117.
66. J. Y. Shu, Y.-J. Huang, C. Tan, A. D. Presley, J. Chang and T. Xu, *Biomacromolecules*, 2010, **11**, 1443-1452.
67. H. Chen, S. Kim, W. He, H. Wang, P. S. Low, K. Park and J.-X. Cheng, *Langmuir*, 2008, **24**, 5213-5217.

68. H. Chen, S. Kim, L. Li, S. Wang, K. Park and J.-X. Cheng, *Proceedings of the National Academy of Sciences*, 2008, **105**, 6596-6601.
69. J. Lu, S. C. Owen and M. S. Shoichet, *Macromolecules*, 2011, **44**, 6002-6008.
70. J. Y. Shu, R. Lund and T. Xu, *Biomacromolecules*, 2012, **13**, 1945-1955.
71. F. A. Heberle, R. S. Petruzielo, J. Pan, P. Drazba, N. Kučerka, R. F. Standaert, G. W. Feigenson and J. Katsaras, *Journal of the American Chemical Society*, 2013, **135**, 6853-6859.
72. A. J. Garcia-Saez, S. Chiantia and P. Schwille, *Journal of Biological Chemistry*, 2007, **282**.
73. N. L. Ogihara, M. S. Weiss, W. F. Degrado and D. Eisenberg, *Protein science : a publication of the Protein Society*, 1997, **6**, 80-88.
74. S. S. Huang, B. R. Gibney, S. E. Stayrook, P. Leslie Dutton and M. Lewis, *Journal of molecular biology*, 2003, **326**, 1219-1225.

Chapter 7

1. Y. Kimiho, I. Hirotaka, I. Toshio, F. Takanori and H. Chuichi, *Chemistry Letters*, 1984, **13**, 1713-1716.
2. T. Kunitake, *Angewandte Chemie International Edition in English*, 1992, **31**, 709-726.
3. A. Kakinuma, H. Sugino, M. Isono, G. Tamura and K. Arima, *Agricultural and Biological Chemistry*, 1969, **33**, 973-&.
4. J. S. Martinez, G. P. Zhang, P. D. Holt, H. T. Jung, C. J. Carrano, M. G. Haygood and A. Butler, *Science*, 2000, **287**, 1245-1247.
5. J. D. Hartgerink, E. Beniash and S. I. Stupp, *Science*, 2001, **294**, 1684-1688.
6. J. D. Hartgerink, E. Beniash and S. I. Stupp, *Proceedings of the National Academy of Sciences of the United States of America*, 2002, **99**, 5133-5138.
7. M. O. Guler, S. Soukasene, J. F. Hulvat and S. I. Stupp, *Nano Letters*, 2005, **5**, 249-252.
8. H. Z. Jiang, M. O. Guler and S. I. Stupp, *Soft Matter*, 2007, **3**, 454-462.
9. H. Storrie, M. O. Guler, S. N. Abu-Amara, T. Volberg, M. Rao, B. Geiger and S. I. Stupp, *Biomaterials*, 2007, **28**, 4608-4618.
10. H. G. Cui, M. J. Webber and S. I. Stupp, *Biopolymers*, 2010, **94**, 1-18.
11. P. Berndt, G. B. Fields and M. Tirrell, *Journal of the American Chemical Society*, 1995, **117**, 9515-9522.
12. Y.-C. Yu, P. Berndt, M. Tirrell and G. B. Fields, *Journal of the American Chemical Society*, 1996, **118**, 12515-12520.
13. Y.-C. Yu, T. Pakalns, Y. Dori, J. B. McCarthy, M. Tirrell and G. B. Fields, in *Methods in Enzymology*, Academic Press, 1997, vol. Volume 289, pp. 571-587.
14. Y.-C. Yu, V. Roontga, V. A. Daragan, K. H. Mayo, M. Tirrell and G. B. Fields, *Biochemistry*, 1999, **38**, 1659-1668.
15. T. Pakalns, K. L. Haverstick, G. B. Fields, J. B. McCarthy, D. L. Mooradian and M. Tirrell, *Biomaterials*, 1999, **20**, 2265-2279.
16. T. Gore, Y. Dori, Y. Talmon, M. Tirrell and H. Bianco-Peled, *Langmuir*, 2001, **17**, 5352-5360.
17. N. Dube, J. W. Seo, H. Dong, J. Y. Shu, R. Lund, L. M. Mahakian, K. W. Ferrara and T. Xu, *Biomacromolecules*, 2014, **15**, 2963-2970.
18. H. Dong, J. Y. Shu, N. Dube, Y. Ma, M. V. Tirrell, K. H. Downing and T. Xu, *Journal of the American Chemical Society*, 2012, **134**, 11807-11814.
19. Y.-H. Chen, J. T. Yang and K. H. Chau, *Biochemistry*, 1974, **13**, 3350-3359.
20. B. Forood, E. J. Feliciano and K. P. Nambiar, *Proceedings of the National Academy of Sciences of the United States of America*, 1993, **90**, 838-842.
21. J. Y. Su, R. S. Hodges and C. M. Kay, *Biochemistry*, 1994, **33**, 15501-15510.

Appendix

A.1 Supporting information for Chapter 2

A.1.1

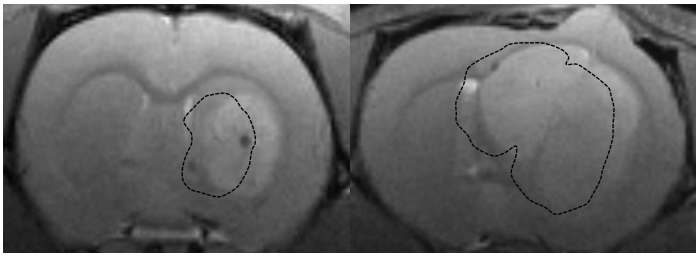

A.1.1 MR images of rat brain bearing tumors. Left and right images are obtained at 9 and 16 days (tumor volume: 48 and 201 mm^3) post-intracranial transplantation of U87 cells, respectively. (Black dots represent the GBM border)

A.1.2

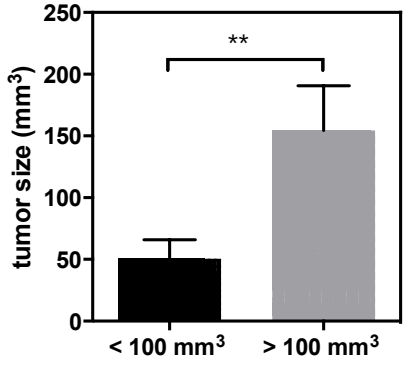

A.1.2 Average tumor size from 9 and 16 days post-intracranial transplantation of U87 cells (data represents mean and SD, unpaired *t-test* with Welch's correction, $p = 0.0016$)

A.2 Supporting information for Chapter 3

A.2.1

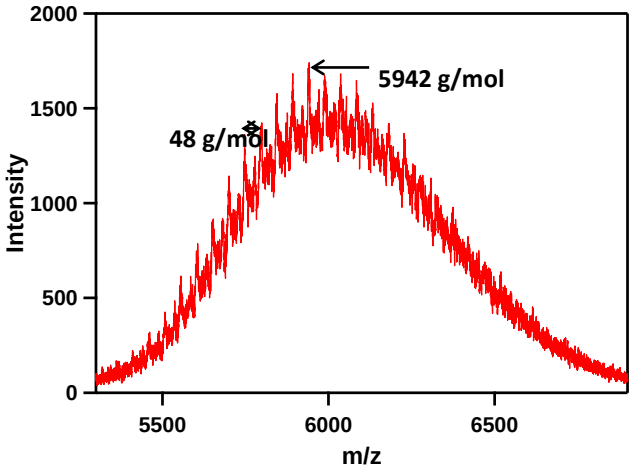

A.2.1 MALDI of dC16-1CW(dPEG), Δm/z of 48 g/mol indicates the presence of deuterated ethylene oxide repeat units.

A.2.2

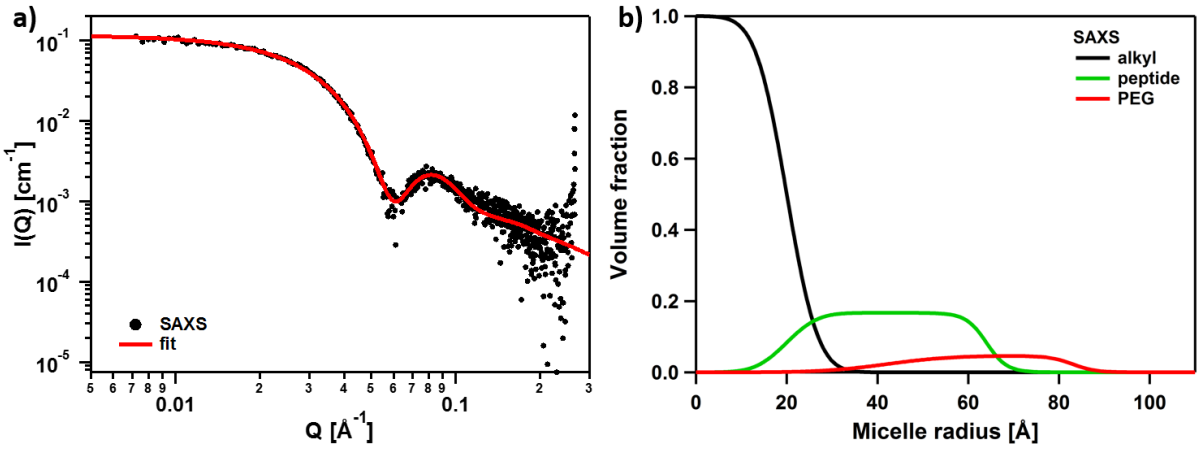

A.2.2 a) SAXS profile of 3HM with PEG at the 14 position. b) Radial density profiles of the different components of 3HM.

A.2.3

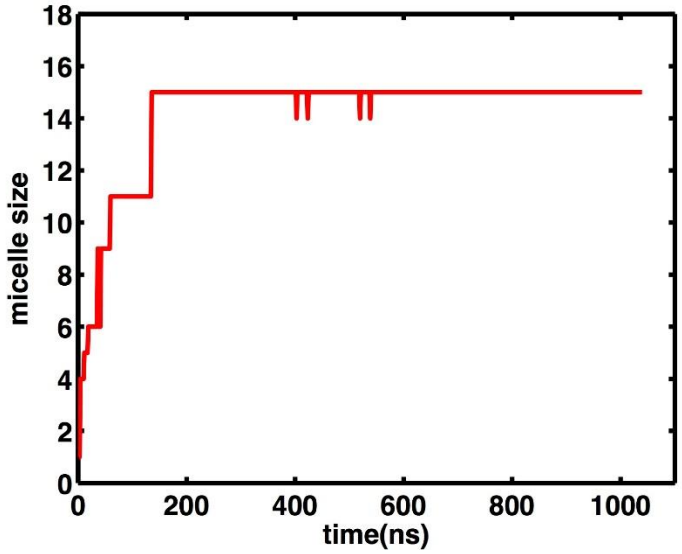

A.2.3 The aggregation number for the micelle selected for all the analyses in CGMD as a function of simulation time.

A.2.4

a_{ij}	water	PEG	alkyl	peptides
water	25	26.3	100	33.7
PEG	26.3	25	100	100
alkyl	100	100	25	100
peptides	33.7	100	100	100

A.2.4 Repulsion parameter a_{ij} used for the interactions between the different bead-types in MD DPD model.

A.2.5

	FWHM		95%	
Thickness of component	SANS (Å)	CGMD (Å)	SANS (Å)	CGMD (Å)
alkyl	25	23	35	27
peptide	38	23	53	51
PEG	61	37	92	68

A.2.5 Thicknesses of peptide, PEG, and alkyl layers within 3HM from SANS and CGMD, reported in two different ways: (1) full-width at half maximum (FWHM) and (2) range of the distribution representing 95% of each component.

A.3 Supporting information for Chapter 4

A.3.1

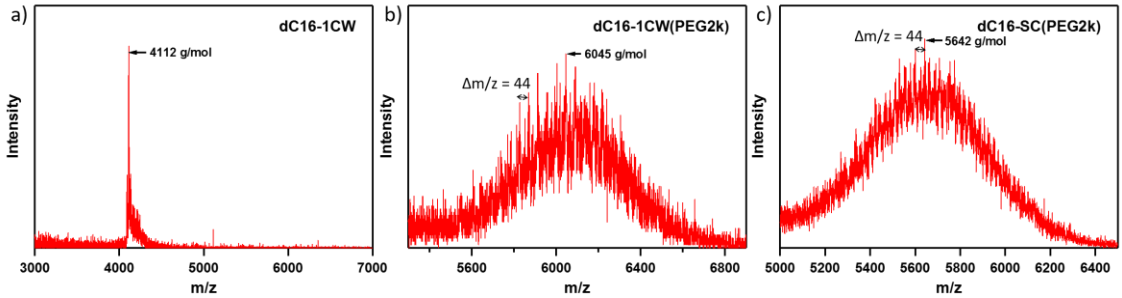

A.3.1 MALDI of (a) dC16-1CW, (b) dC16-1CW(PEG2k), and (c) dC16-SC(PEG2k). The expected m/z for dC16-1CW is 4079 and the observed m/z of 4112 corresponds to the $[M+K]^+$ ion. Δm/z of 44 g/mol indicates the presence of ethylene oxide repeat units. The m/z ratios for the PEGylated peptides indicate 44 repeat ethylene oxide units.

A.3.2

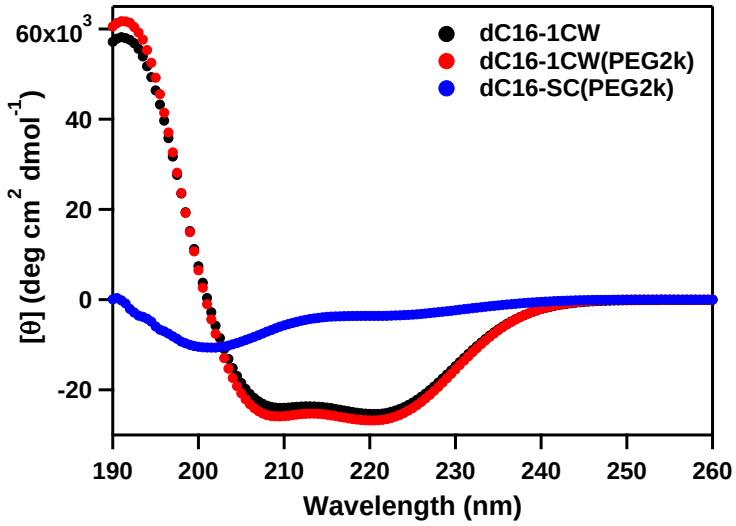

A.3.2 CD spectra of ~100 μM dC16-1CW (black), dC16-1CW(PEG2k) (red), and dC16-SC(PEG2k) (blue). $\theta_{222}/\theta_{208} \geq 1$ for 1CW-based amphiphiles indicate the presence of coiled-coils.

A.3.3

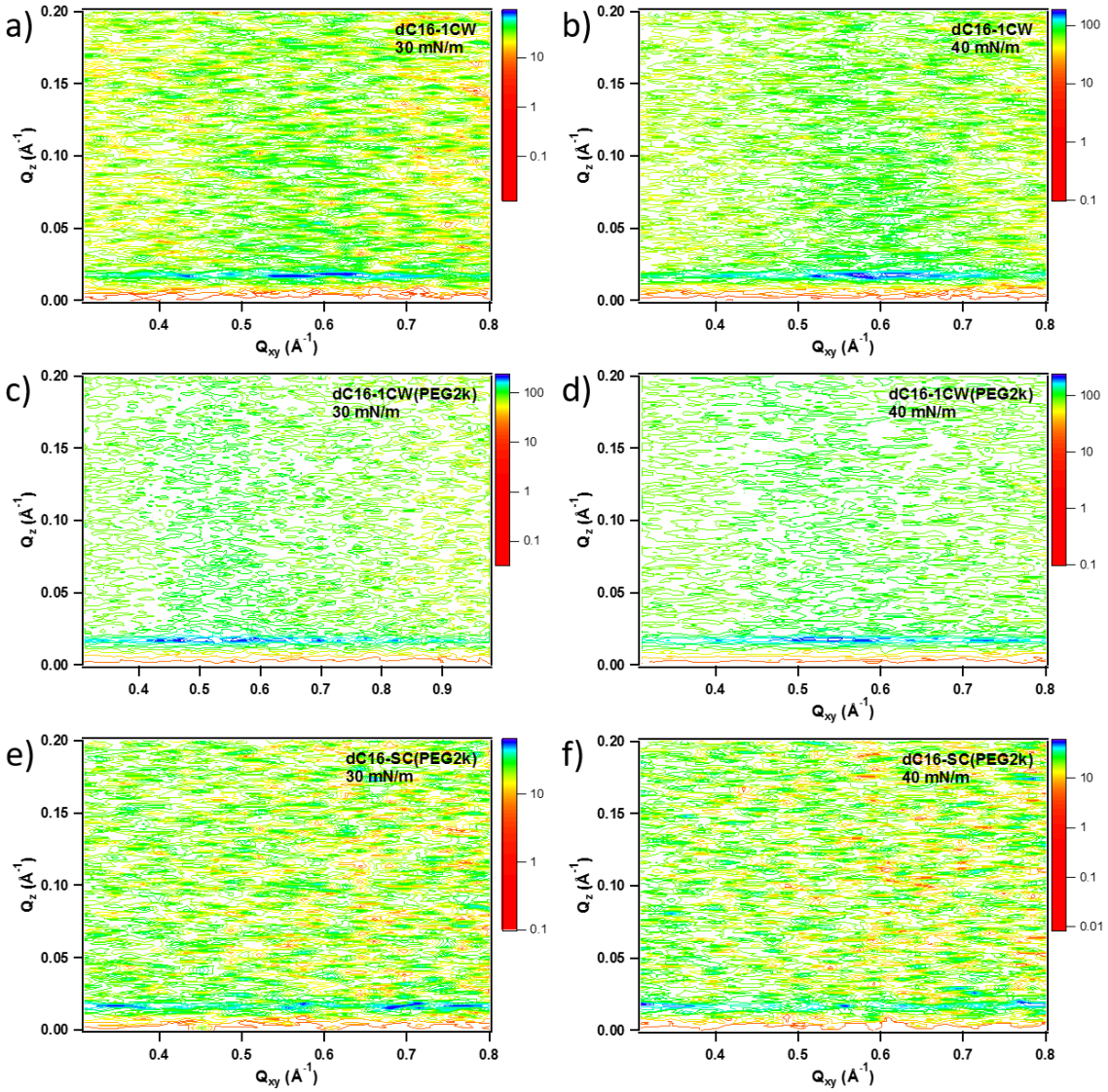

A.3.3 2D contour plots of GIXD patterns for dC16-1CW at (a) 30 mN/m and (b) 40 mN/m; dC16-1CW(PEG2k) at (c) 30 mN/m and (d) 40 mN/m; and dC16-SC(PEG2k) at (e) 30 mN/m and (f) 40 mN/m.

A.4 Supporting information for Chapter 5

A.4.1

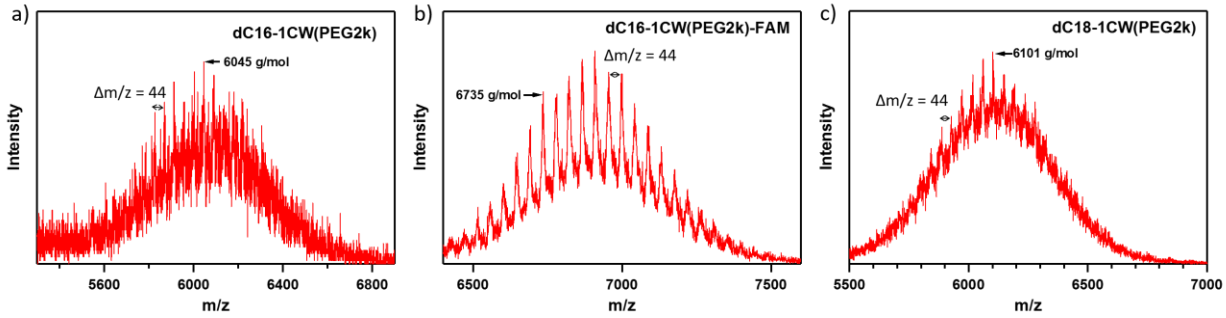

A.4.1 MALDI of (a) dC16-1CW(PEG2k), (b) dC16-1CW(PEG2k)-FAM, and (c) dC18-1CW(PEG2k). Δm/z of 44 g/mol indicates the presence of ethylene oxide repeat units.

A.4.2

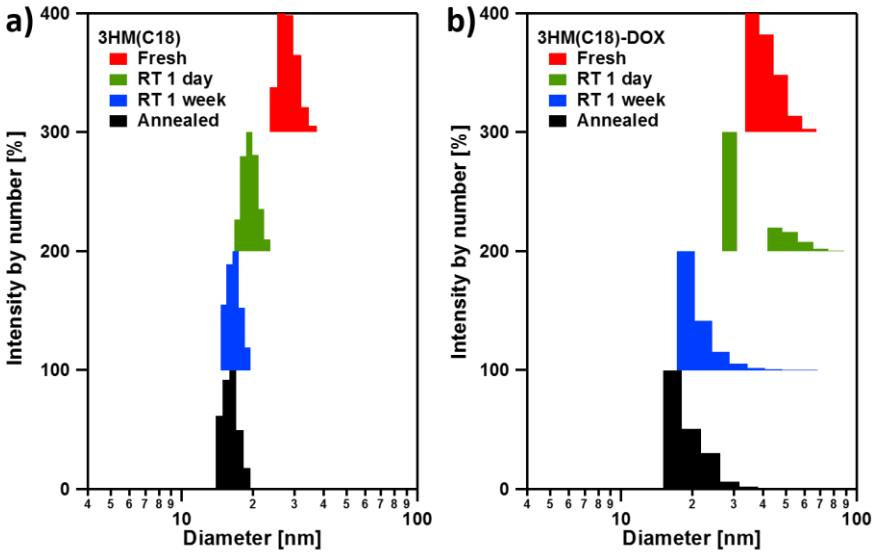

A.4.2 Time-dependent changes in size distributions of (a) 3HM(C18) and (b) 3HM(C18)-DOX.

A.4.3

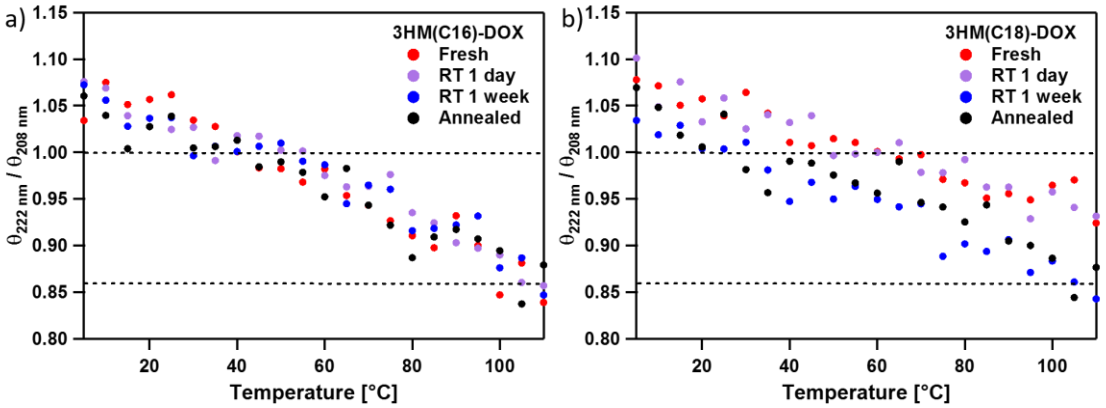

A.4.3 Temperature-dependent circular dichroism spectra showing $\theta_{222}/\theta_{208}$ of (a) 3HM(C16)-DOX and (b) 3HM(C18)-DOX.

A.5 Supporting information for Chapter 6

A.5.1

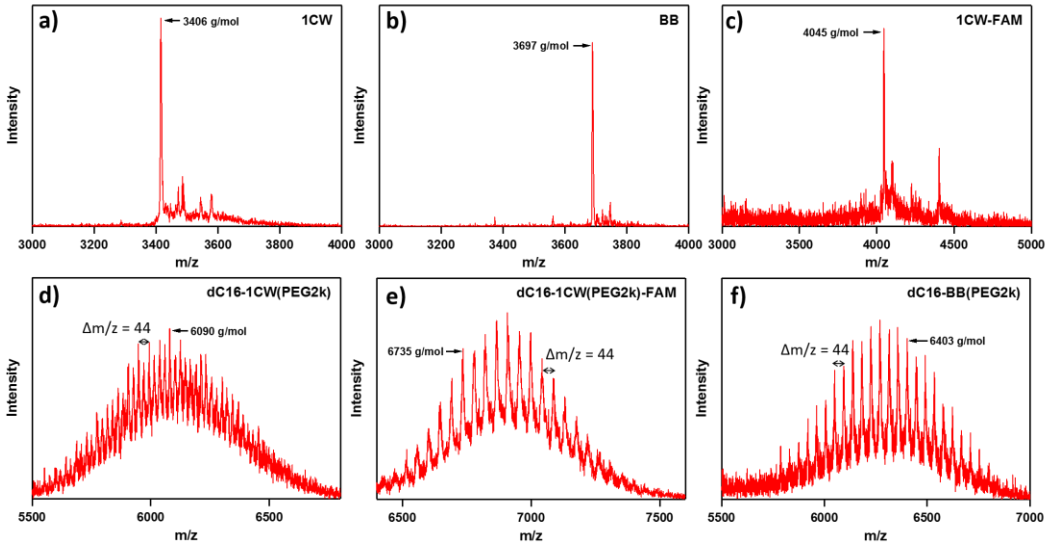

A.5.1 MALDI of purified peptides and conjugates. (a) 1CW, (b) BB, (c) 1CW-FAM, (d) dC16-1CW(PEG2k), (e) dC16-1CW(PEG2k)-FAM, and (f) dC16-BB(PEG2k).

A.5.2

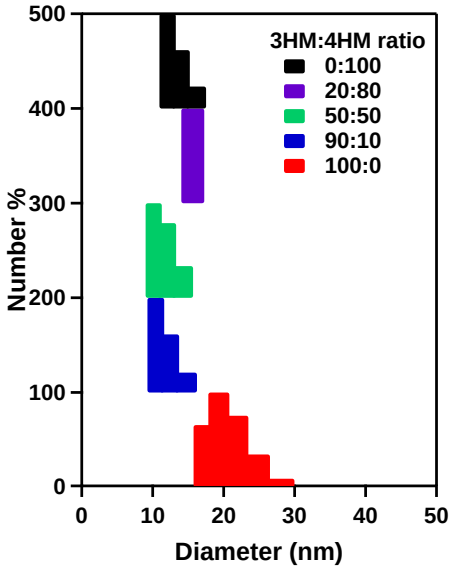

A.5.2 Size distributions of mixed micelles from different 3HM:4HM ratios measured by DLS.

A.5.3

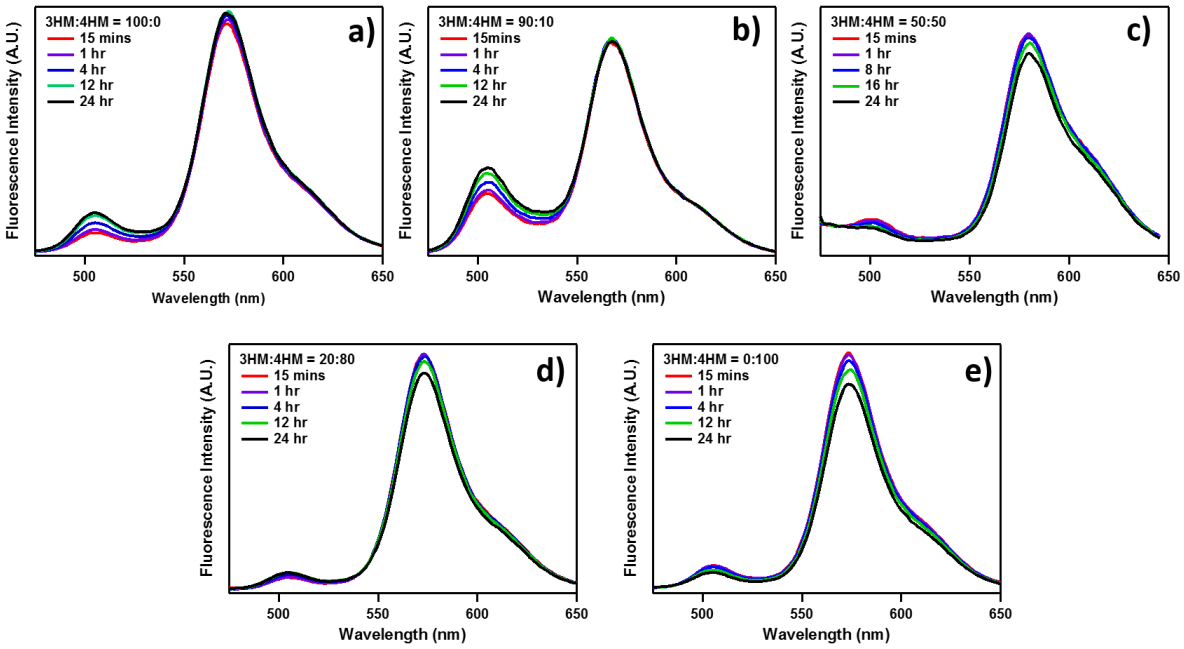

A.5.3 Time-resolved fluorescence spectra of mixed micelles at various 3HM:4HM ratios (a) 100:0, (b) 90:10, (c) 50:50, (d) 20:80, and (e) 0:100 encapsulated with a FRET pair.